



HAL
open science

Design, Modeling, Fabrication, Characterization and Applications of very Wideband Semiconductor Optical Amplifiers

Agnes Verdier

► **To cite this version:**

Agnes Verdier. Design, Modeling, Fabrication, Characterization and Applications of very Wideband Semiconductor Optical Amplifiers. Optics [physics.optics]. INSA de Toulouse, 2018. English. NNT : 2018ISAT0051 . tel-03578670

HAL Id: tel-03578670

<https://theses.hal.science/tel-03578670>

Submitted on 17 Feb 2022

HAL is a multi-disciplinary open access archive for the deposit and dissemination of scientific research documents, whether they are published or not. The documents may come from teaching and research institutions in France or abroad, or from public or private research centers.

L'archive ouverte pluridisciplinaire **HAL**, est destinée au dépôt et à la diffusion de documents scientifiques de niveau recherche, publiés ou non, émanant des établissements d'enseignement et de recherche français ou étrangers, des laboratoires publics ou privés.



THÈSE

En vue de l'obtention du

DOCTORAT DE L'UNIVERSITÉ DE TOULOUSE

Délivré par :

l'Institut National des Sciences Appliquées de Toulouse (INSA de Toulouse)

Présentée et soutenue le *04/09/2018* par :

AGNÈS VERDIER

Modélisation, conception, fabrication, caractérisation et valorisation d'amplificateurs optiques à semiconducteur de très large bande spectrale.

JURY

JOËL JACQUET	Rapporteur
MICHAEL CONNELLY	Rapporteur
DELPHINE MORINI	Membre du Jury
CHANTAL FONTAINE	Membre du Jury
JEREMIE RENAUDIER	Membre du Jury invité
HÉLÈNE CARRERE	Directrice de thèse
HÉLÈNE DEBREGEAS	Encadrante industrielle

École doctorale et spécialité :

GEET : Photonique et Systèmes Optoélectroniques

Unité de Recherche :

*Laboratoire de Physique Chimie des Nano-objets (LPCNO) & III-V
Lab*

Directeur de Thèse :

Hélène CARRERE

Rapporteurs :

Joël Jacquet et Michael Connelly

Summary (English)

Optical networks are constantly evolving toward higher transmission rates in optical fiber. However in the past few years optical fiber spectral efficiency seems to be reaching its upper limit. Best solution to keep increasing data rates consists then in increasing spectral bandwidth used in optical fibers, currently limited to 35 nm due to restricted bandwidth of erbium-doped fiber amplifiers (EDFAs) used for in-line amplification. Previous studies have been conducted to evaluate whether semiconductor optical amplifiers (SOAs) could replace EDFAs and offer an extended bandwidth. Promising results have been obtained but blocking points have also been identified regarding SOAs saturation output power and noise figure. During the thesis we have developed solutions to these issues to make use of SOAs a realistic option.

Beginning of the thesis was dedicated to design of wideband SOAs consisting of material simulations at LPCNO to understand and optimize active structure of the amplifiers. This study was completed by optical simulations at III-V Lab in order to integrate an asymmetric cladding to the SOA for increased saturation output power and lower noise. Different chip geometries were also proposed for improved performances. These designs were fabricated and characterized at III-V Lab.

Resulting SOAs have demonstrated a spectral bandwidth of 120 nm in S+C+L band with optical gain within 3 dB of 18.5 dB maximal value. Chip optical far-field is quasi-circular with full-width at half maximum divergence angle as low as 17° which greatly participated in reducing coupling losses. In module, we obtained saturation output power of 23 dBm at 25°C . Improvement of noise figure is also visible as it reaches 4 dB in L-band.

Several applications using our SOAs have already been tested notably as repeater in long-haul optical communications with great results. They have also been integrated to tunable external cavity lasers where their wide gain bandwidth has permitted record tuning range. These lasers also showed record narrow linewidth in the kHz range and output power of 10 dBm.

At III-V Lab the thesis was supervised by Romain Brenot and H el ene Debr egeas for design, characterization and valorization of the SOAs. At LPCNO (Laboratoire de Physique et Chimie des Nano-Objets) H el ene Carr ere supervised wideband material modeling and simulations

Summary (French)

Les réseaux de transport optique connaissent une constante évolution et requièrent des débits de plus en plus importants par fibre optique. Depuis quelques années, l'efficacité spectrale des fibres atteint un plafond, et semble proche de sa limite ultime. La meilleure manière d'augmenter les débits consisterait à étendre la largeur spectrale utilisée dans les fibres optiques. Actuellement, cette largeur est limitée à 35 nm, à cause de la bande optique restreinte des amplificateurs utilisés, les EDFA (Erbium-Doped Fiber Amplifiers). Dans le cadre de projets précédents la capacité des SOAs (Semiconductor Optical Amplifiers) à pouvoir un jour remplacer les EDFA en offrant une plage spectrale nettement plus étendue a été évaluée. Les résultats en ont été très prometteurs, mais nous avons identifié un certain nombre de points bloquants concernant notamment la puissance de saturation et le bruit des SOAs. Durant la thèse nous avons développé des solutions à ces blocages pour tirer le meilleur profit de l'approche SOA large-bande de puissance.

La thèse a débuté par la conception des SOAs large-bande de puissance. Cette phase a consisté en campagnes de simulation matériaux au LPCNO pour comprendre et valider la structure active des amplificateurs. Des simulations optiques au III-V Lab ont également été réalisées afin d'optimiser la puissance de saturation des SOAs à travers l'utilisation d'une couche de matériau à fort indice de réfraction sous le guide. De plus différentes géométries ont été proposées pour optimiser les performances des composants. Une fois la conception terminée les composants ont été fabriqués et caractérisés au sein du III-V Lab.

Les SOAs réalisées ont démontré une bande passante optique record de 120 nm en bande S+C+L avec un gain de 18.5 dB. Le champ lointain des puces est relativement circulaire avec une divergence très faible à mi-hauteur autour de 17° qui

nous a permis d'améliorer les pertes de couplage et tendre vers une mise en module optimisée. Nous avons obtenu une puissance de saturation des SOAs de 23 dBm à 25 ° C en module. Enfin grâce aux améliorations apportées, le facteur de bruit de nos SOA atteint 4 dB en bande L.

Plusieurs applications ont d'ores et déjà été testées avec ces composants à commencer par leur utilisation en télécommunication optique pour des transmissions longue distance avec d'excellents résultats. Ils ont également été intégrés dans des lasers en cavité externe avec des performances remarquables en termes d'accordabilité et de largeur de raie des lasers.

Au sein du laboratoire III-V Lab, la thèse a été étroitement encadrée par Romain Brenot et Hélène Debrégeas pour les parties conception, expérimentation et valorisation. Au sein du Laboratoire de Physique et Chimie des Nano-Objets (UMR INSA-CNRS-UPS) de Toulouse, Hélène Carrère a encadré les travaux sur la partie modélisation des matériaux large bande optique.

Résumé de la thèse en français

0.1 Introduction

Cette section introduit le concept d'amplificateur optique à semiconducteur avec une brève explication de l'origine de l'amplification ainsi qu'une description du composant. Les caractéristiques de l'amplificateur que nous utilisons dans la suite du manuscrit sont également présentées. Puis nous nous intéressons à son utilisation dans les télécommunications optiques. Nous décrivons le besoin actuel de amplificateurs large-bande et les limites technologiques rencontrées par les amplificateurs traditionnels. Nous montrons les arguments en faveur de l'utilisation des amplificateurs optiques à semiconducteur dans les futurs réseaux optiques multiplexés en longueur d'onde. Nous passons enfin en revue les travaux existant sur le sujet des amplificateurs optiques à semiconducteur large-bande pour aboutir à la solution proposée dans cette thèse.

0.1.1 Amplificateur optique à semiconducteur

Les amplificateurs optiques à semiconducteur (SOA) utilisés dans les télécommunications optiques sont composés de matériaux semiconducteurs à bande-interdite directe issus des systèmes GaAs et InP. Cela signifie que les extremums de leurs bande de conduction et de valence ont le même vecteur d'onde et sont séparés par une bande d'énergie interdite appelée E_g . Cela permet aux porteurs électriques présents dans la bande de conduction de recombiner dans la bande de valence en émettant un photon dont l'énergie est proche de E_g .

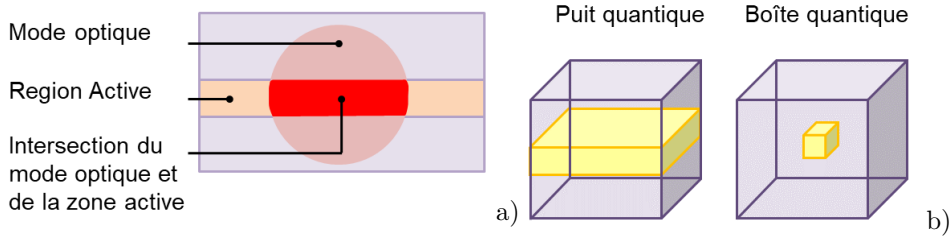


Figure 1 – a) Confinement optique Γ défini comme le rapport entre la zone rouge vif et les zones rouge clair. b) Confinement spatial des porteurs électriques imposés par les puits quantiques et les boîtes quantiques.

Cette recombinaison radiative peut prendre deux formes. D'un côté l'émission stimulée lors de laquelle un photon incident d'énergie proche de E_g provoque la recombinaison de deux porteurs électriques (électron et trou) ce qui génère un deuxième photon identique au premier. Ces deux photons sont cohérents, ils partagent la même énergie, phase et direction de propagation. À l'inverse l'émission spontanée est un phénomène aléatoire qui résulte en la création d'un photon dont l'énergie est certes proche de E_g mais dont la phase et la direction sont aléatoires. Elle est à l'origine de l'émission spontanée amplifiée (ASE) lorsque ces photons génèrent à leur tour de nouveaux photons par émission stimulée. Ces phénomènes sont expliqués plus en détail dans [1].

Pour que la recombinaison puisse avoir lieu il faut que la densité de porteurs électriques soit suffisante dans le matériau. La zone active d'un SOA est pour cette raison placée entre deux couches de matériaux dopées p et n pour former une diode PiN dans laquelle on injecte du courant. Cette zone active est généralement composée d'un alliage quaternaire InGaAsP qui possède un indice de réfraction élevé. Cela crée un effet de guidage optique pour les photons présents dans le composant et les concentre dans la zone active ce qui favorise l'émission stimulée. La concentration des photons dans la zone active est quantifiée par le confinement optique Γ donné en pourcentage. La Figure 1 a) illustre sa définition.

Différents types de structures peuvent être utilisés dans la zone active. Une couche de matériau uniforme aussi appelée couche massive, des puits quantiques, voire des boîtes quantiques. Chacune de ces structures correspond à un degré de confinement supplémentaire des porteurs électriques dans l'espace et présente des caractéristiques qui lui sont propres. Figure 1 b) montre le confinement 1D dû aux puits quantiques et le confinement 3D dans les boîtes quantiques.

Un SOA est un guide d'onde comprenant un milieu à gain et délimité par deux facettes traitées anti-reflet. Sa structure est donc proche de celle d'un laser Fabry-Pérot tout en évitant l'effet laser en diminuant la réflectivité des facettes. Dans un

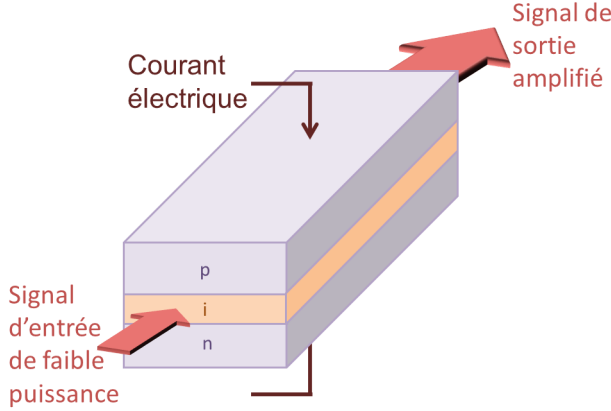


Figure 2 – Schéma d'un SOA.

SOA l'amplification peut avoir lieu lorsque qu'un signal lumineux dont les photons ont une énergie proche de E_g du matériau composant la zone active est envoyé à travers le SOA. Un courant électrique doit être appliqué à l'SOA pour augmenter la densité de porteurs. On obtient du gain lorsque l'émission stimulée compense l'absorption et les pertes du guide d'onde. Une représentation schématique du composant est présentée en Figure 1.5. Les SOA utilisés dans les télécommunications optiques fonctionnent à des longueurs d'ondes autour de 1.3 et 1.55 μm fenêtres de faible absorption et dispersion des fibres optiques. Leurs gains sont généralement compris entre 20 et 30 dB avec une bande-passante optique allant de 30 à 80 nm [2, 3].

Trois grandeurs sont principalement utilisées pour caractériser un SOA : son gain G , son facteur de bruit NF et sa puissance de saturation P_{sat} . Ces grandeurs sont définies par les équations suivantes :

$$G(n) = C_1 C_2 \exp[(\Gamma g_m(n) - \alpha(n))L] \quad (1)$$

$$NF = \frac{2P_{ASE}}{G_{puce} h\nu B_0} + \frac{1}{G_{puce}} = \frac{2n_{sp}}{C_1} \quad (2)$$

$$P_{sat} = \ln(2) \frac{A}{\Gamma} \frac{h\nu}{a_1 \tau} \frac{G_0}{G_0 - 2} \quad (3)$$

Avec n la densité de porteurs électriques, C_1 et C_2 le taux de couplage en entrée et en sortie de l'SOA (compris entre 0 et 1), $g_m(n)$ le gain matériau, $\alpha(n)$ les pertes, L la longueur du guide d'onde, P_{ASE}/B_0 la densité spectrale d'ASE, G_{puce} le gain puce ne prenant pas en compte les pertes de couplage, n_{sp} le facteur d'inversion qui quantifie le remplissage des niveaux d'énergie, $h\nu$ l'énergie d'un photon, A la section de la zone active (*largeur* \times *épaisseur*), $a_1 = \frac{dg_m}{dn}$ le gain différentiel, τ le temps de vie des porteurs et G_0 le gain nominal à la densité de porteurs considérée.

Il est à retenir de ces équations que les performances d'un SOA sont d'autant meilleures que les pertes de couplage et les pertes du guide d'onde sont faibles. Il est également important d'avoir un bon rapport signal à bruit pour minimiser le NF dont la valeur minimale théorique est de 2 (soit 3 dB). Un faible confinement optique permet d'augmenter P_{sat} et de diminuer le NF mais au détriment du gain, ce qui peut être compensé en allongeant le composant. Un bon OAS aura un gain et une P_{sat} élevés ainsi qu'un faible NF.

0.1.2 Applications pour les télécommunications

Les réseaux de transport optique connaissent une constante évolution et requièrent des débits de plus en plus importants par fibre optique. Cette augmentation constante est accompagnée par l'amélioration continue des réseaux optiques. Le multiplexage en longueur d'onde a tout d'abord permis de paralléliser les canaux de transmission. Cette technique a ensuite progressé par l'amélioration de la densité spectrale dans la fibre optique. Des composants plus rapide et la complexification des formats de modulation ont également contribué à l'accélération des débits de données.

Ces différentes méthodes trouvent leurs applications dans les trois types de réseaux existants dont les caractéristiques nécessitent des solutions spécifiques. On distingue les réseaux longue distance (≈ 1000 km), les réseaux métropolitains (≈ 100 km) et les réseaux d'accès (≈ 10 km). Depuis quelques années, l'efficacité spectrale des fibres atteint un plafond, et semble proche de sa limite ultime. La meilleure manière d'augmenter les débits consisterait à étendre la largeur spectrale utilisée dans les fibres optiques. Actuellement, cette largeur est limitée à 35 nm, à cause de la bande optique restreinte des amplificateurs utilisés, les EDFA (Erbium-Doped Fiber Amplifiers). Pour cette raison nous nous intéressons aux SOA qui présentent une bande-passante optique plus large. Les EDFA leur ont jusqu'à présent été préférés car ils ont plus de gain, une figure de bruit plus faible et peuvent être utilisés en régime saturé ce qui n'est pas le cas des SOA. Si nous parvenons à développer un SOA de bande-passante large (≈ 120 nm) et dont les performances s'approchent de celles des EDFA ce composant présentera un intérêt majeur pour les télécommunications optiques.

0.1.3 Etat de l'art des amplificateurs optiques à semiconducteur large-bande

L'élargissement de la bande-passante est donc le moteur de notre recherche sur les SOA. De nombreuses solutions ont d'ores et déjà été essayées. A un courant donné, la bande-passante des SOA est définie comme l'étendue des longueurs d'onde pour

0.2. STRUCTURE MATÉRIAU DE L'AMPLIFICATEUR OPTIQUE À SEMICONDUCTEURix

lesquelles le gain est compris entre sa valeur maximale G_{max} et la moitié de celle-ci $G_{max}/2$. Le spectre de gain ayant habituellement une forme parabolique, tronquer les valeurs maximales de gain permet par exemple d'abaisser le G_{max} considéré et ainsi d'étendre la bande-passante à -3 dB. L'utilisation de filtres pour égaliser la bande-passante des SOA a été envisagée parmi d'autres solutions. Les difficultés pour réaliser ce type de composant et contrôler efficacement le filtrage ont conduit à l'abandon de cette solution.

La solution donnant les meilleurs résultats jusqu'à présent a été proposée par une équipe japonaise. Leur structure à puits quantiques leur permet d'étendre la bande-passante de leur SOA jusqu'à 120 nm avec d'excellentes performances par ailleurs [4, 5]. Cependant malgré ces remarquables résultats la méthode choisie n'est pas applicable aux longueurs d'ondes que nous visons et nécessite de très fortes densités de courant. Nous sommes donc partis vers une autre solution présentée dans la section suivante.

0.2 Structure matériau de l'amplificateur optique à semiconducteur

Les travaux présentés dans cette thèse ont été guidés par les résultats obtenus lors de projets précédents. Les projets ANR Arome et Ultrawide ont en effet déjà proposé l'idée originale d'utiliser une structure à puits quantiques pour la zone active de l'SOA avec non pas une mais deux transitions afin d'élargir la bande-passante optique. En nous basant sur les travaux déjà réalisés nous avons travaillé sur l'amélioration des performances de l'SOA ainsi que sur son adaptation aux forte puissances. Les travaux présentés ont été largement portés par le projet FUI Calipso.

0.2.1 Conception d'un amplificateur optique à semiconducteur large-bande

La structure choisie pour obtenir un SOA large-bande est un empilement de plusieurs puits quantiques. Les propriétés d'une telle structure peuvent être modifiées en jouant sur la composition, l'épaisseur et la contrainte des puits. Comme nous utilisons un alliage quaternaire InGaAsP la zone active peut en effet présenter un désaccord de maille avec le substrat InP sur lequel a lieu la croissance matériau. Ce désaccord crée une contrainte sur la couche qui peut être en compression ou en tension selon que la maille de l'alliage quaternaire est plus grande ou plus petite que la maille de l'InP. Jouer sur la contrainte pour améliorer les propriétés

d'un composant est une technique largement utilisée dans les télécommunications optiques [6].

La contrainte a notamment un effet important sur la dépendance à la polarisation du composant car la compression favorise l'amplification en polarisation transverse électrique (TE) alors que la tension permet d'être indépendant à la polarisation voire de favoriser l'amplification en polarisation transverse magnétique (TM). Dans les réseaux optiques la fibre ne permet pas de maintenir l'état de polarisation de la lumière et celle-ci peut se trouver dans n'importe quelle combinaison de TE et TM à l'entrée d'un SOA. Il est donc important que l'amplificateur puisse amplifier les deux polarisations de façon équivalente. Nous avons choisi pour notre SOA d'amplifier principalement en polarisation TE mais de développer un module à diversité de polarisation qui permet d'amplifier les deux polarisation à partir de deux de nos SOA. Ce module est présenté dans la dernière partie de la thèse. A partir de simulations matériaux comprenant le calcul des niveaux d'énergie et de la structure de bande des puits quantiques, nous avons développé une structure de SOA large-bande fonctionnant en bande télécom S, C et L qui correspondent respectivement aux plages de longueurs d'onde 1460-1530 nm, 1530-1565 nm et 1565-1625 nm.

La présence de deux transitions résulte en deux régimes de fonctionnement pour la structure simulée. Pour des courants d'injection faibles, seuls les premiers niveaux d'énergie ont une densité de porteurs suffisante pour avoir du gain. Le spectre de gain ressemble alors à celui d'un SOA classique. Alors que le courant augmente, les niveaux de plus haute énergie se remplissent et on commence à obtenir du gain aux énergies plus élevées. Arrive un point où le gain est équivalent sur les deux transitions. Le spectre de gain est alors le plus large et relativement plat. Le courant de gain plat est noté I_m . Aux courants plus élevés la deuxième transition présente plus de gain que la première et le spectre de gain est incliné avec un maximum aux hautes énergies. La Figure 3 illustre ce mécanisme à travers le spectre d'ASE qui suit les mêmes variations que le spectre de gain.

Étant donnée la précision requise lors de la croissance des couches composant les puits quantiques nous avons souhaité réaliser plusieurs structures voisines pour d'une part réduire le risque lié à l'incertitude expérimentale et de l'autre étudier les effets de légères variations sur notre structure. Nous avons donc développé cinq variations autour de la même structure appelées A, A bis, B, C et D. La structure A est notre structure de référence à laquelle se compareront les autres. La structure A bis est ainsi nommée de par sa proximité avec la structure A. En effet la seule différence entre elles provient de la différence d'épaisseurs des couches de confinement. Ces couches entourent la zone active et servent à confiner le mode optique dans celle-ci. En augmentant leur épaisseur on augmente Γ dans les puits quantiques. Ceci a pour effet d'augmenter le gain mais aussi de réduire la puissance de saturation. Les structures A et A bis partagent néanmoins la même zone active.

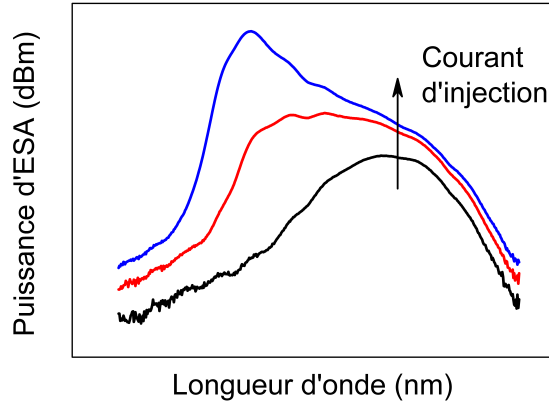


Figure 3 – Evolution du spectre d'ASE avec le courant d'injection de l'SOA. En rouge, le courant de spectre plat pour lequel la largeur spectrale est maximale

Structure	caractéristiques
A	Structure de référence
A bis	Confinement optique plus fort
B	Décalage spectral de +20 nm
C	Barrières de plus grande bande d'énergie interdite
D	Puits plus fins

Table 1 – Caractéristiques des cinq structures

La structure B ne diffère de la structure A que par la composition de ses puits quantiques afin de déplacer de 20 nm la position de la première transition des puits. On souhaite ainsi déplacer la bande-passante optique vers la bande L. Les structures C et D visent quant à elles à affaiblir la deuxième transition par rapport à la première pour obtenir un gain suffisant aux hautes longueurs d'onde. En effet lorsque l'on commence à avoir du gain aux basses longueurs d'onde, celui des plus hautes longueurs d'onde cesse quasiment d'augmenter. On cherche donc à retarder l'apparition du gain à basses longueurs d'onde. Concrètement cela passe par un changement de composition des barrières entourant les puits quantiques de la structure C afin de moins confiner les niveaux électroniques correspondant à la deuxième transition. Dans la structure D on réduit l'épaisseur des puits afin d'espacer les niveaux électroniques.

0.2.2 Conception d'un amplificateur optique à semiconducteur de puissance

Le deuxième aspect mis à l'étude lors de la thèse est celui de la puissance de saturation. Les transmissions avec multiplexage en longueur d'onde envisagées comme application prévoient la transmission d'environ cent canaux simultanés ce qui nécessite une forte puissance totale pour que chaque canal bénéficie d'une puissance suffisante. Nous prévoyons une puissance de saturation d'au moins 20 dBm ce qui permettra de répartir au moins 0 dBm par canal. Pour cela nous devons trouver des leviers afin d'augmenter la puissance de saturation de nos composants.

Le processus de fabrication est tout d'abord optimisé afin d'améliorer l'efficacité de l'injection électrique et de l'évacuation de la chaleur. Le processus technologique choisi est appelé SIBH pour semi-insulated buried heterostructure et consiste à enterrer le guide d'onde dans de l'InP isolant. La forte résistivité du matériau isolant permet une bonne injection du courant dans le guide en évitant les courants de fuite latéraux. L'InP qui entoure le guide permet de plus de diffuser la chaleur émise par le composant et favorise la régulation en température.

L'équation 1.9 montre la relation entre P_{sat} et différents facteurs. Pour augmenter la valeur de P_{sat} les deux leviers les plus accessibles sont l'augmentation de la section de la zone active A et la diminution de Γ . A cette fin nous avons décidé d'implémenter un "cladding asymétrique" dans notre structure matériau. Cette méthode est utilisée avec succès par plusieurs équipes pour augmenter la puissance de saturation d'AOS [7–9]. Elle permet de diminuer Γ mais également d'augmenter la largeur du ruban jusqu'à 5 μm tout en restant monomode. Un ruban plus large est bénéfique à P_{sat} à travers l'augmentation de la section A mais il favorise aussi une bonne résistance thermique.

Des composants ont été fabriqués à partir de chaque structure développée. Ces composants ont ensuite été testés pour déterminer leurs performances et les comparer aux prévisions établies.

0.3 Résultats

Avant de pouvoir mesurer les composants il faut les cliver, traiter leurs facettes pour abaisser la réflectivité à 10^4 et enfin les monter sur embase pour pouvoir les manipuler et injecter du courant plus facilement. Les composants étant initialement tiltés à 7° l'embase permet aussi de corriger cet angle pour que le faisceau lumineux sorte perpendiculairement à l'arête de l'embase. Sur celle-ci se trouve également

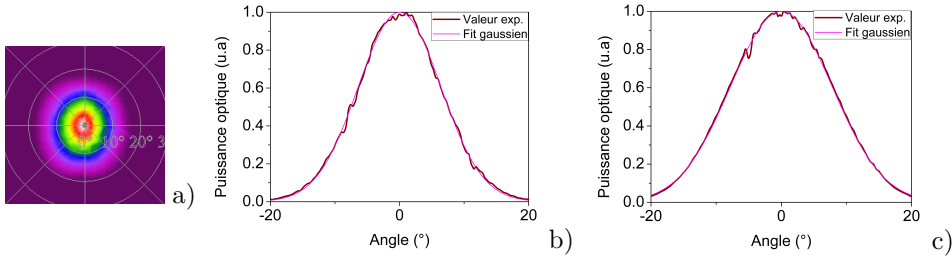


Figure 4 – a) Reconstruction du champ lointain du SOA A. b) Mesure de la divergence horizontale. c) Mesure de la divergence verticale.

une résistance thermique utilisée pour la régulation en température du composant à travers un module Peltier. Durant les mesures la température est réglée à 25 °C.

Les résultats présentés proviennent de mesures réalisées sur des SOA de 4 mm de long et de ruban de 5 μm de large de chacun des cinq design à l'exception des mesures de champ lointain réalisées sur des puces de 2 mm. Les composants sont respectivement nommés SOA A, SOA A bis, SOA B, SOA C et SOA D.

0.3.1 Mode optique

Une des premières caractérisations effectuées consiste à observer la géométrie du mode optique par une mesure de son champ lointain à la sortie du SOA à l'aide d'une caméra. Une fente placée devant la caméra permet une mesure à différents angles dans le plan perpendiculaire à la direction de propagation de la lumière. Les données obtenues permettent de déterminer l'angle de divergence du faisceau lumineux mesuré sur les axes verticaux et horizontaux. Elles permettent également de reconstruire la forme du faisceau en répétant la mesure sur 360 °.

La Figure 4 présente les mesures réalisées pour l'SOA A. On observe un mode très légèrement elliptique pour lequel on obtient un excellent fit gaussien avec un angle à mi-hauteur de 15.1 ° horizontalement et 18.4 ° verticalement. Il en va de même pour tous les SOA dont les angles de divergences sont tous compris entre 14 ° et 19 °. Ces valeurs sont bien adaptées au couplage avec une fibre optique. Nous obtenons ainsi des pertes de couplage de seulement 1.7 dB lors de cette campagne de mesure.

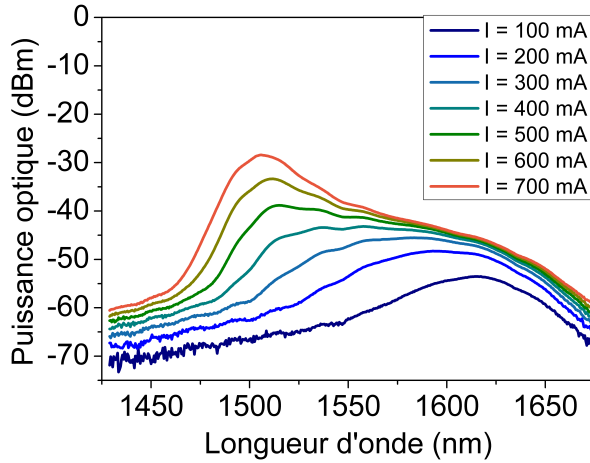


Figure 5 – Spectre d’ASE de l’SOA A pour différents courants d’injection.

0.3.2 Bande-passante optique et gain

Dans cette section nous évaluons le caractère large-bande des SOA à travers notamment la mesure des spectres de gain. Toutefois une première estimation de la bande-passante optique peut être réalisée en mesurant le spectre d’ASE des SOA. L’émission spontanée résulte en effet elle aussi des transitions à l’intérieur des puits quantiques et les deux transitions présentes dans nos structures doivent logiquement en élargir le spectre. Le spectre d’ASE est donc proche du spectre de gain d’autant plus que nos amplificateurs ne présentent pas de SHB (spacial hole burning).

Pour mesurer le spectre d’ASE, le SOA est injecté électriquement. On couple ensuite une fibre optique à l’une de ses facettes, que l’on connecte ensuite à un analyseur de spectre optique (OSA) qui mesure et affiche la puissance optique résolue en longueur d’onde. La figure 5 présente l’évolution du spectre d’ASE du SOA A en fonction du courant d’injection. Pour les courants les plus faibles un seul pic correspondant à la première transition est visible autour de 1620 nm et sa puissance augmente avec le courant. Assez rapidement le spectre s’élargit au fur et à mesure que les niveaux électroniques se remplissent et la seconde transition commence à avoir du gain. Autour de 400 mA le spectre est large et plat. Lorsque le courant dépasse cette valeur la deuxième transition a plus de gain que la première et un second pic apparaît autour de 1510 nm. Alors que ce second pic acquiert plus de puissance avec le courant, le premier pic à 1620 nm n’augmente plus. Ce spectre présente les caractéristiques prévues par simulation et les deux transitions résultent bel et bien en un large spectre.

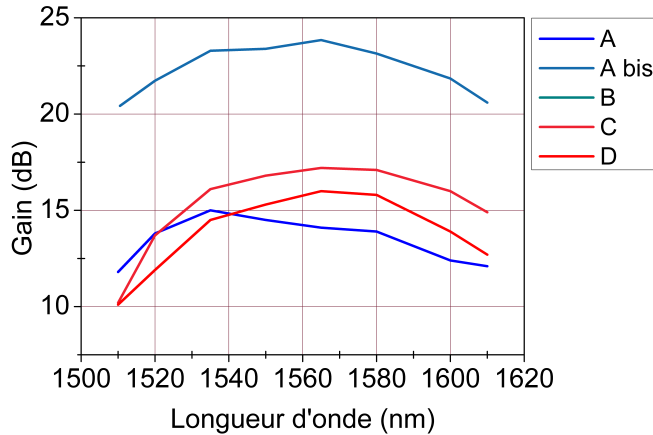


Figure 6 – Spectre de gain des cinq SOA à 500 mA.

La mesure de gain est un peu plus complexe car il faut injecter un signal optique d'entrée dans le composant. Ce signal est donné par une source laser accordable dont la puissance transmise est contrôlée par un atténuateur. On lit sur l'OSA la puissance de sortie du composant à laquelle on soustrait la puissance d'ASE, également lue sur l'OSA. Connaissant la puissance à l'entrée du SOA on peut alors établir le rapport P_{out}/P_{in} qui donne le gain.

Pour une meilleure comparaison on trace Figure 3.14 le spectre de gain des cinq SOAs à 500 mA, au courant de gain plat du design A. Les autres designs présentent un courant de gain plat plus élevé. Il apparaît d'ailleurs sur le graphe que les spectres des SOA A bis, B, C et D ne sont pas encore tout à fait plats. Comme prévu l'SOA A bis présente le plus de gain. Il est très positifs que tous les SOA aient un spectre de gain large, la structure paraît ainsi tolérante vis-à-vis des variations imposées.

0.3.3 Facteur de bruit et puissance de saturation

La mesure de NF a lieu en même temps que la mesure de gain car elle fait intervenir les mêmes grandeurs. Elle correspond à la mesure du rapport signal à bruit du composant prenant en compte la largeur du filtre optique de l'ASO (sa résolution) et l'énergie des photons. Comme précédemment nous traçons les cinq courbes de NF sur le même graphe en Figure 7 a). Pour toutes ces courbes le NF est meilleur aux grandes longueurs d'onde ce qui provient de la diminution du facteur d'inversion. Il atteint une valeur minimale record de 4 dB à 1610 nm ce qui est un excellent résultat.

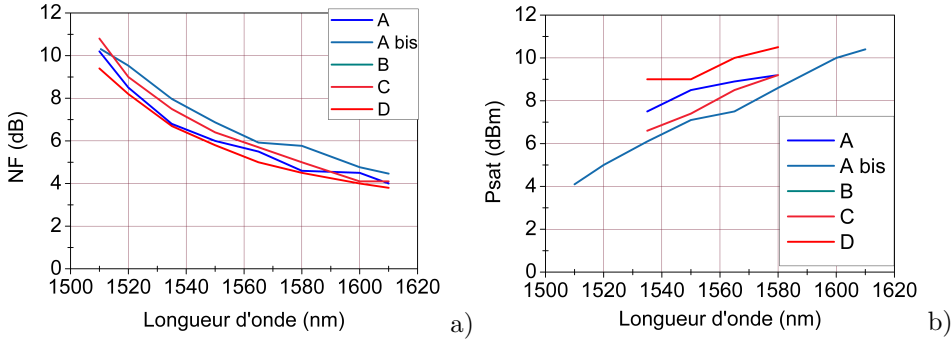


Figure 7 – a) NF des cinq SOA à 500 mA. b) P_{sat} des cinq SOA à 500 mA.

La puissance de saturation est obtenue à partir d'une courbe de gain tracée en fonction de la puissance de sortie pour un courant d'injection fixé (500 mA ici). Pour tracer cette courbe nous augmentons progressivement la puissance optique à l'entrée de l'SOA jusqu'à observer une chute du gain de 3 dB. A ce point on relève la puissance de saturation en sortie. Les valeurs mesurées pour les cinq SOA sont présentées Figure 7 b). On observe que P_{sat} augmente aux grandes longueurs d'onde en raison de la diminution du gain différentiel a_1 . Comme nous le prévoyons l'SOA A bis présente la valeur de P_{sat} la plus faible. Les valeurs obtenues ne dépassent pas 9 dBm à 1550 nm en raison de la méthode de mesure. Nous prévoyons de plus d'utiliser les SOA à des courants plus élevés de l'ordre de 1 A où la P_{sat} augmente. Cela sera illustré dans l'une des applications présentées dans la dernière section de ce manuscrit.

Les résultats présentés dans cette section sont en accord avec les structures théoriques visées. Les différences entre les composants suivent les variations de conception entre les structures. Les spectres de gain obtenus sont larges et la figure de bruit des SOA atteint des valeurs très faibles. La puissance de saturation n'est pas aussi élevée que prévue mais peut être améliorée dans les conditions réelles d'utilisation. Dans la section suivante nous explorons des pistes pour optimiser les composants.

0.4 Test de nouveaux concepts

Au cours de la thèse, plusieurs optimisations des SOA ont été proposées. Nous avons abordé dans les sections précédentes celles portant sur l'aspect large-bande et forte puissance. Nous nous intéressons à présent à la géométrie des composants que nous avons jusqu'à présent laissée de côté. Nous avons notamment étudié l'impact de la largeur du guide d'onde sur ses performances. Nous avons également testé des SOA

multi-sections pour l'amélioration conjointe de la puissance de saturation et de la figure de bruit des amplificateurs. Nous présentons dans cette section l'une de ces optimisations destinée à la mesure de gain intégrée sur puce.

0.4.1 Mesure de gain intégrée

Une fois mis en place dans un réseau ou un système optique le SOA n'est généralement plus accessible isolément. Cela est notamment vrai dans les circuits photoniques intégrés (PIC) où les SOA sont souvent utilisés et peuvent intervenir tant du côté des émetteurs en étant associés avec des lasers et des modulateurs, que du côté de récepteurs en amplifiant un signal avant une photodiode. Pour ces composants intégrés, la caractérisation est un réel problème. En effet les méthodes classiques de mesure du gain et du NF telles que présentées dans la section 0.3 ne leur sont pas applicables dans la mesure où elles font intervenir les pertes de couplage associées au composant afin d'obtenir le gain fibre à fibre. Elles nécessitent de plus de pouvoir accéder à la puissance optique en entrée et en sortie du composant ce qui est souvent impossible pour un composant intégré dans un PIC. Il serait néanmoins extrêmement intéressant d'avoir accès au gain optique des SOA intégrés afin de mieux contrôler leurs performances et comprendre les effets des facteurs environnementaux auxquels ils sont soumis. Cela n'est pas seulement vrai pour les PIC mais dans tous les scénarios d'utilisation des SOA.

Plusieurs méthodes ont été proposées pour mesurer la valeur du gain des SOA sans perturber le système optique dans lequel ils sont intégrés. Une caractérisation en température a par exemple été proposée. Elle établit un lien entre la différence de température de surface du SOA par rapport à une référence et le gain optique du composant [10, 11]. Malgré de bons résultats cette technique est difficilement incorporable dans une routine de mesure car elle nécessite des équipements spécifiques pour un suivi de température précis. D'autres groupes ont établi un lien entre le gain optique et l'émission spontanée du SOA, soit par une relation entre l'intensité de l'émission spontanée et le gain [12], soit en corrélant la longueur d'onde du pic d'ASE et le gain optique [13]. D'autres groupes ont divisé le SOA en trois sections et démontré une relation entre le gain optique et le rapport de tension électrique des sections d'entrée et de sortie [14]. Toutes ces méthodes requièrent une calibration, souvent à travers une mesure de gain traditionnelle. Elles demeurent de plus une évaluation indirecte du gain en établissant un lien entre celui-ci et une autre grandeur plus accessible.

Nous rappelons que la mesure directe du gain est donnée par le rapport entre les puissances de sortie (une fois ôtée la contribution de l'ASE) et d'entrée. Ces paramètres peuvent être déterminés en collectant une fraction de la lumière à l'aide de photodiodes dans la méthode présentée en [15] : deux photodiodes collectent une

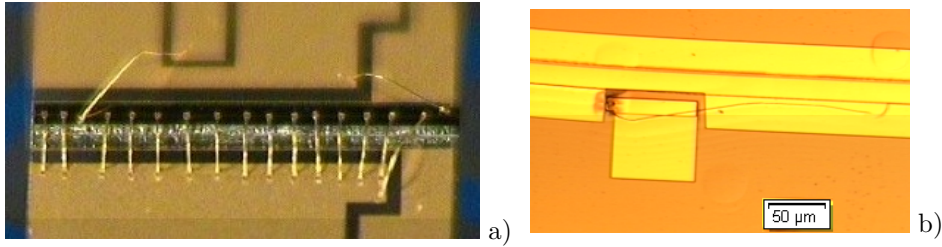


Figure 8 – a) SOA avec photodiodes intégrées, repérées sur la figure par les deux fils électriques rejoignant des électrodes séparées. b) Détail de la photodiode ($90 \mu\text{m} \times 90 \mu\text{m}$).

fraction de la lumière réfléchiée sur les lentilles utilisées pour le couplage à l'entrée et la sortie de l'SOA. Pour adapter cette méthode à l'utilisation recherchée il faut trouver une solution qui permette d'intégrer ces photodiodes directement sur la puce. Pour une puissance d'entrée connue, l'utilisation de photodiodes intégrées pour collecter une fraction du signal de sortie et en déduire le gain a déjà été présentée [16]. Nous proposons d'aller au bout de cette démarche en intégrant deux photodiodes sur puce pour une mesure directe du gain optique d'un SOA. Des guides couplés positionnés aux facettes d'entrée et de sortie collectent la même fraction du signal sur des photodiodes identiques. La méthode est testée pour une mesure de gain à plusieurs courants et différentes longueurs d'onde.

0.4.2 Simulation, mesure et résultats

L'implémentation des photodiodes est testée sur un SOA classique non-intégré dans un PIC afin de pouvoir facilement comparer les résultats avec la méthode de mesure de gain traditionnelle. Nous utilisons un SOA fonctionnant dans la bande de télécommunication C et doté d'une zone active comprenant des puits quantiques en InGaAsP. Le guide d'onde est enterré selon le processus technologique SIBH et comprend un cladding asymétrique. Le composant est long de 4 mm et le ruban est large de $4 \mu\text{m}$. Des simulations de propagation optique ont été réalisées pour concevoir les guides couplés. Leur largeur est fixée à $4 \mu\text{m}$ et dans la zone de couplage celle du guide principal est réduite à $2.5 \mu\text{m}$. L'espacement entre les deux guides est de $1.8 \mu\text{m}$ et la zone de couplage est longue de $70 \mu\text{m}$. La Figure 8 a) montre la puce tout entière et laisse apparaître le câblage des photodiodes. Une vue agrandie des photodiodes est montrée en Figure 8 b). Les deux coupleurs ainsi que les deux photodiodes sont identiques pour assurer la même responsivité.

Pour mesurer le gain optique du SOA, celui-ci est polarisé à plusieurs valeurs de courant. Dans le même temps, les photodiodes sont polarisées à une tension constante

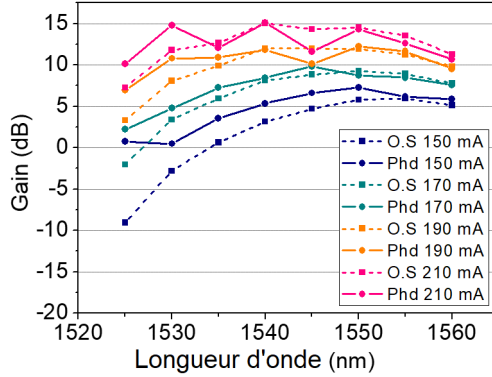


Figure 9 – Spectres de gain des SOA avec photodiodes intégrées. En trait continu, la mesure avec les photodiodes, en pointillé, la mesure classique.

de -1 V qui permet de favoriser la collecte des porteurs. Une source laser accordable en bande C fournit un signal optique à -23 dBm. Le composant est réglé à 25 °C. A chaque courant nous mesurons les photocourants des deux photodiodes, une première fois sans signal d'entrée pour identifier la contribution de l'ASE puis une seconde fois avec le signal pour véritablement mesurer le gain.

Le gain est calculé de la manière suivante : $G = (I_{out} - I_{outASE}) / (I_{in} - I_{inASE})$ avec I_{out} le photocourant en sortie en présence de signal, I_{outASE} le photocourant en sortie sans signal, I_{in} le photocourant en entrée en présence de signal et I_{inASE} le photocourant en entrée sans signal. Le gain ainsi mesuré est le gain intrinsèque de la puce puisqu'il ne prend pas en compte les pertes de couplage.

Pour comparer notre méthode de mesure par photocourant avec la méthode de mesure de gain classique, nous caractérisons le même SOA avec cette dernière. Lors de cette mesure, les photodiodes ne sont pas polarisées. La méthode classique donne le gain fibre à fibre car les pertes de couplage sont comprises dans les puissances optiques lues. Pour pouvoir comparer les mesures nous corrigeons donc la mesure de gain classique avec les pertes de couplage mesurées. Lors de ces mesures nous obtenions environ 5 dB de pertes de couplage. La Figure superpose les spectres de gain obtenus avec les deux méthodes entre 1525 nm et 1560 nm. Les deux méthodes donnent des résultats comparables ce qui est très encourageant pour la méthode proposée. De nouveaux tests seront réalisés pour confirmer ces bons résultats.

0.5 Applications

Nous proposons deux applications à nos SOA, toutes deux utilisant leurs propriétés large-bande : un laser en cavité externe très largement accordable et un module bi-SOA indépendant à la polarisation pour les réseaux d'accès. Dans les deux cas, la structure des SOA utilisés correspond au design B présenté dans les sections précédentes. Ces SOA combinent donc une structure à multi-puits quantiques large-bande avec un cladding asymétrique pour augmenter la puissance de saturation de l'amplificateur.

0.5.1 Laser largement accordable

Les lasers accordables font l'objet d'un grand intérêt depuis le développement du multiplexage en longueur d'onde. Utiliser un matériau large-bande pour augmenter l'accordabilité d'un laser à cavité externe a par le passé donné de bons résultats [17]. Dans le but de réduire la largeur de raie du laser pour le rendre utilisable dans les transmissions cohérentes ou des applications de détection (LIDAR, OCT), il est possible d'utiliser des circuits de guides d'onde en silice [18]. En mêlant ces deux approches nous démontrons un laser accordable sur 69 nm qui présente de plus une largeur de raie extrêmement étroite de l'ordre du kHz ainsi qu'une puissance de sortie atteignant 10 dBm [19].

Pour l'application laser le composant utilisé est un RSOA, un SOA réfléchissant dont l'une des facettes conserve une forte réflectivité pour un effet miroir. Ce composant est associé avec un circuit de guide d'onde en silice optimisé pour la forte puissance [18]. La facette du RSOA en contact avec la silice est tiltée à 7° et traitée anti-reflet. L'autre facette est au contraire clivée droite pour une réflectivité d'environ 30%. Le circuit en silice est composé de trois anneaux résonnants en série et d'une section de phase. Le laser est accordé par effet Vernier en chauffant les anneaux résonnants.

Le laser affiche une accordabilité de 69 nm présentée dans la Figure 10 a) pour une variation de courant de 5.4 mA sur un anneau résonnant. La puissance de sortie moyenne est de 10 dBm. La largeur de raie du laser a été mesurée à travers un montage auto-homodyne et on obtient une valeur à l'état de l'art de 2.7 kHz. Cette valeur est extraite par fit lorentzien de la mesure de bruit de phase présentée Figure 10 b). Le couplage entre le RSOA et la silice n'étant pas fixé mécaniquement il est sujet à des instabilités qui portent préjudice aux mesures. On peut dès lors s'attendre à une amélioration de la puissance de sortie et de la largeur de raie avec un montage plus stable [20].

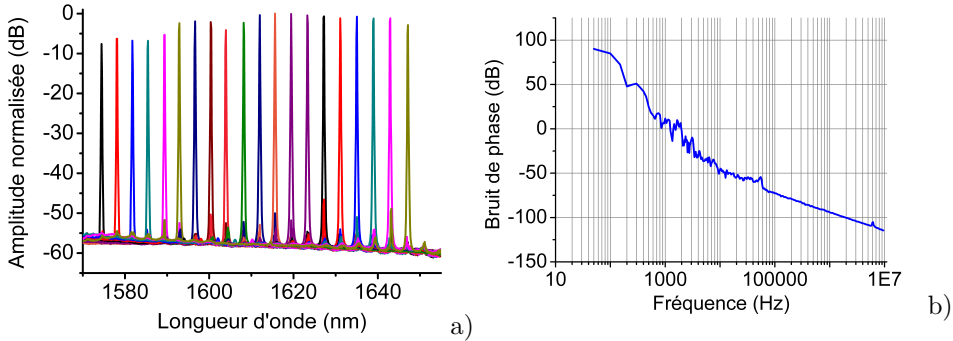


Figure 10 – a) Plage d'accordabilité du laser. b) Mesure de bruit de phase.

0.5.2 Amplificateur en ligne indépendant à la polarisation

Nous présentons également les performances d'un module indépendant à la polarisation comprenant deux SOA large-bande identiques. Dans les réseaux d'accès un amplificateur bi-directionnel est indispensable au niveau du terminal comme "booster" pour les signaux descendants et comme pré-amplificateur pour les signaux montants [21]. Dans NG-PON2 (Next Generation Passive Optical Network 2), l'une des solutions proposées pour l'accès, la bande-optique envisagée commence à 1524 nm pour les signaux montants et s'étend jusqu'à 1603 nm pour les signaux descendants nécessitant donc une large bande-passante optique [22]. Un amplificateur optique indépendant à la polarisation de large bande-passante peut également trouver des applications dans les transmissions multiplexées en longueur d'onde [23]. Pour un courant de 1 A nous démontrons une bande-passante de gain optique à -3 dB entre 1500 nm et 1620 nm d'une valeur maximale de 18.5 dB. Le composant présente également une puissance de saturation en sortie de plus de 20 dBm et une figure de bruit comprise entre 5 et 7.5 dB sur la plage de longueurs d'onde considérée.

Les SOA intégrés dans le module sont identiques à ceux présentés dans la section 0.3. Ils sont longs de 4 mm avec des rubans larges de $5 \mu\text{m}$, tiltés de 7° et traités anti-reflet sur les deux facettes. Pour obtenir un module indépendant à la polarisation nous utilisons deux SOA dans un schéma à diversité de polarisation réalisé en optique libre. Ce schéma est composé d'un séparateur de polarisation suivi des deux SOA et est intégré dans un module développé lors du projet Calipso par le III-V Lab et ses partenaires Kyla et Egide. La lumière polarisée TE va directement dans le premier SOA mais la lumière polarisée TM subit tout d'abord une rotation vers la polarisation TE avant de pénétrer dans le second SOA où elle peut alors être amplifiée. Après amplification, la lumière demeurée TE subit à son tour une rotation pour devenir TM afin d'assurer la symétrie des deux chemins optiques à l'intérieur du module. Le montage en optique libre permet d'obtenir des pertes

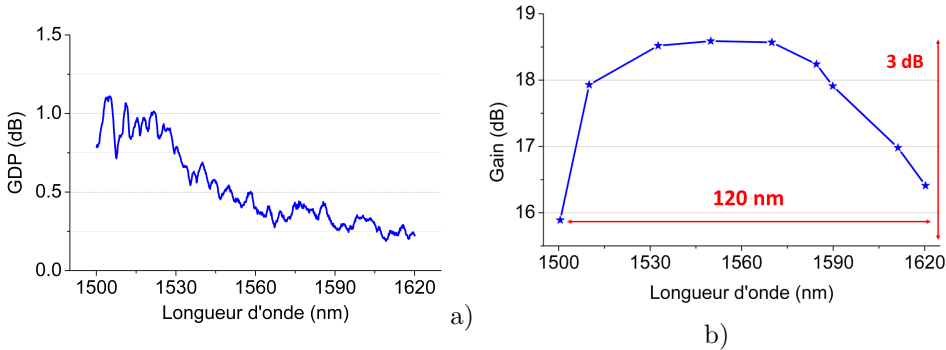


Figure 11 – a) Gain dépendant de la polarisation. b) Spectre de gain du module.

de couplage de l'ordre du dB. La paire de SOA est brasée à l'indium-étain (InSn) sur une embase dédiée pour une bonne conductivité thermique et une résistance électrique minimale. Le contrôle en température est assuré par un module Peltier commandé par une résistance thermique placée à mi-chemin entre les deux SOA.

La Figure 11 a) présente la dépendance du gain à la polarisation dans le module pour des longueurs d'ondes comprises entre 1500 et 1620 nm. Ce paramètre caractérise le rapport entre les gains TE et TM et quantifie de fait la qualité du schéma à diversité de polarisation. Dans la mesure où il ne dépasse pas 1 dB on considère que le module corrige effectivement la dépendance à la polarisation des puces. Pour ce faire on doit légèrement ajuster le courant des SOA aux valeurs suivantes : 1 A pour l'SOA 1 et 1.05 A pour l'SOA 2.

Pour ces courants, la Figure 11 b) montre le gain du module en fonction de la longueur d'onde pour une puissance d'entrée de 3.5 dBm. Nous obtenons un gain plat de 18.5 dB avec une variation inférieure à -3 dB sur 120 nm. La bande-passante de gain s'étend de 1500 nm à 1620 nm. Afin de déterminer la puissance de saturation nous mesurons le gain à des puissances d'entrée de plus en plus élevées. La puissance de saturation obtenue dans les bandes C et L est présentée Figure 12 a). Cette puissance présente une valeur minimale de 20 dBm et augmente jusqu'à 25 dBm à 1620 nm. La puissance de saturation est plus faible aux basses longueurs en raison de l'augmentation du gain différentiel. Le facteur de bruit est également présentée en Figure 12 b). Au-delà de 1570 nm le NF atteint 5 dB ce qui est à notre connaissance la valeur la plus basse jamais obtenue pour un SOA en module. Le NF augmente aux courtes longueurs d'onde à cause de la diminution du facteur d'inversion n_{sp} à haute énergie.

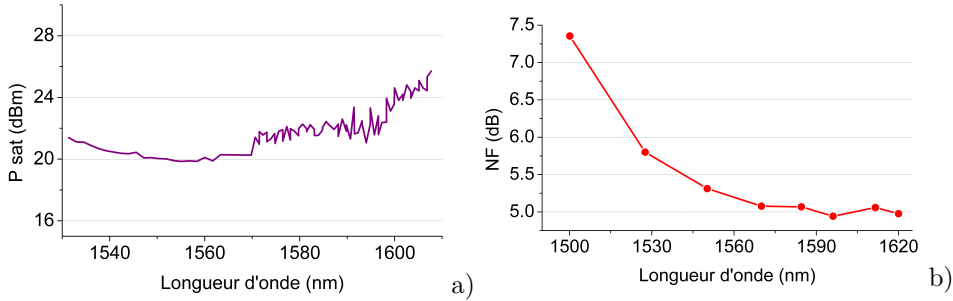


Figure 12 – a) P_{sat} du module. b) NF du module.

0.6 Conclusion

Nous nous sommes intéressés dans ce manuscrit au développement d'amplificateurs optiques à semiconducteur large-bande et forte puissance pour des applications dans les télécommunications optiques. Nous avons présenté les simulations effectuées lors de la conception des composants afin d'optimiser les performances des amplificateurs. Ceux-ci ont été fabriqués et testés au laboratoire. Ils présentent d'excellents résultats.

Nous avons également testé des optimisations géométriques des composants comme l'intégration de photodiodes sur l'amplificateur pour une mesure de gain sur puce. Enfin grâce à leurs performances ces amplificateurs ont pu être testés dans plusieurs applications dont un module amplificateur pour les réseaux d'accès et un laser largement accordable [19]. Les performances obtenues sont à l'état de l'art et les résultats obtenus démontrent l'intérêt de ces composants pour les futurs réseaux de télécommunications optiques. L'amélioration de leur différentes caractéristiques permet de les envisager en remplacement des amplificateurs traditionnels.

Acknowledgements

Je tiens à remercier les nombreuses personnes qui m'ont aidée et soutenue durant ma thèse, au III-V Lab comme au LPCNO.

En premier lieu mes encadrantes Dr. Hélène Carrère et Dr. Hélène Debregeas pour leur accompagnement bienveillant et leurs encouragements tout au long de la thèse. Dr. Romain Brenot également qui m'a proposé ce sujet, formée et encadrée pendant deux ans. Au-delà d'un encadrement scientifique et technique j'ai la chance d'avoir bénéficié de leur énergie et de leur enthousiasme pour leurs travaux de recherche.

Je remercie Prof. Michael Connelly, Dr. Joël Jacquet, Dr. Chantal Fontaine, Prof. Delphine Morini et Dr. Jérémie Renaudier d'avoir accepté de prendre part à mon jury de thèse.

Je souhaite également remercier toutes les personnes impliquées dans la fabrication, la caractérisation et le packaging des SOAs sans lesquels cette thèse n'existerait pas. Je remercie notamment Karim Mekhazni pour ses nombreux montages, Jean-Guy Provost, François Duport et Frédéric van Dijk pour leur aide et leurs explications lors des mesures, Catherine Fortin pour les traitements antireflets, Jean-François Paret, Frédéric Pommereau, Cosimo Calo et Alexandre Garreau pour leur aide et leur travail en salle blanche, tous les épitaxieurs, et plus particulièrement Carme Gomez et Arnaud Wilk pour les discussions sur les structures matériaux, Mathilde Makhsiyani pour son aide lors de la rédaction. J'ai eu l'opportunité de travailler sur le passionnant projet FUI Calipso dont je remercie tous les acteurs, au III-V Lab et en-dehors.

Un grand merci à Mohand Achouche qui m'a permis de venir travailler au III-V

Lab et à Pascale Téfaine pour son aide indispensable.

Bien que n'ayant pas forcément travaillé avec tous je voudrais remercier tous les membres du III-V Lab et du LPCNO que j'ai rencontrés, avec une pensée particulière pour les doctorants. Nos discussions informelles et notre camaraderie ont contribué à la réussite de ma thèse et m'ont enrichie aussi bien professionnellement qu'humainement.

Enfin je remercie ma famille et mes amis de m'avoir soutenue pendant ces trois années comme ils l'ont toujours fait.

Contents

Summary (English)	i
Summary (French)	iii
Résumé de la thèse en français	v
0.1 Introduction	v
0.1.1 Amplificateur optique à semiconducteur	v
0.1.2 Applications pour les télécommunications	viii
0.1.3 Etat de l'art des amplificateurs optiques à semiconducteur large-bande	viii
0.2 Structure matériau de l'amplificateur optique à semiconducteur . . .	ix
0.2.1 Conception d'un amplificateur optique à semiconducteur large- bande	ix
0.2.2 Conception d'un amplificateur optique à semiconducteur de puissance	xii
0.3 Résultats	xii
0.3.1 Mode optique	xiii
0.3.2 Bande-passante optique et gain	xiv
0.3.3 Facteur de bruit et puissance de saturation	xv
0.4 Test de nouveaux concepts	xvi
0.4.1 Mesure de gain intégrée	xvii
0.4.2 Simulation, mesure et résultats	xviii
0.5 Applications	xx
0.5.1 Laser largement accordable	xx
0.5.2 Amplificateur en ligne indépendant à la polarisation	xxi
0.6 Conclusion	xxiii
Acknowledgements	xxv

1	Concepts and State-of-the-Art	1
1.1	Semiconductor Optical Amplifier	1
1.1.1	Amplification medium	1
1.1.2	Semiconductor optical amplifier operation	4
1.1.3	Device characteristics	7
1.2	Applications in Telecommunications	9
1.2.1	Optical telecommunications	9
1.2.2	Wavelength-division multiplexing systems	10
1.2.3	Semiconductor Optical Amplifiers in Telecommunications	13
1.3	Wideband Semiconductor Optical Amplifier State of the Art	15
1.3.1	Integrated filters	15
1.3.2	Dual SOA	19
1.3.3	Quantum dots and multiquantum wells SOA	21
1.4	Context of the PhD	22
2	Material structure of semiconductor optical amplifier	25
2.1	Large-band semiconductor optical amplifier	26
2.1.1	Operating principle	26
2.1.2	Presentation of structures	33
2.2	High power semiconductor optical amplifier	36
2.2.1	Saturation output Power	36
2.2.2	Asymmetric cladding	38
2.2.3	Semi-insulated buried heterostructure	44
3	Characterization	49
3.1	From wafer to SOA	49
3.2	Optical mode	50
3.2.1	Experimental set-up	50
3.2.2	Results	51
3.3	Wideband optical bandwidth	55
3.3.1	ASE spectra	55
3.3.2	Experimental set-up for gain measurement	59
3.3.3	Optical gain	60
3.4	Noise figure and Saturation output power	63
3.4.1	Noise figure	63
3.4.2	Saturation output power	65
3.5	Impact of temperature	67
3.6	Conclusion	69
4	Geometry and integration of the semiconductor optical amplifier	71
4.1	Width of the semiconductor optical amplifier	72
4.1.1	Study of different SOA widths	72
4.1.2	Multimode interferometers	77
4.2	Multi-electrode semiconductor optical amplifier	78

4.2.1	Three-electrode amplifier	78
4.2.2	Experimental results	79
4.3	Integrated gain measurement	84
4.3.1	Applications	84
4.3.2	Proposed method	86
4.3.3	Design and simulations	86
4.3.4	Experimental set-up and results	87
4.4	Conclusion	90
5	Applications	91
5.1	Reach Extender for Optical Access Networks	91
5.1.1	Project presentation	92
5.1.2	Module description	93
5.1.3	Performances of the module	93
5.2	Tunable hybrid external cavity lasers	95
5.2.1	Tunable lasers	95
5.2.2	External cavity design	97
5.2.3	Hybrid laser	99
5.2.4	Hybrid laser characterization	100
5.2.5	Analysis	105
5.3	Conclusion	106
A	List of abbreviations	111
B	Derivation of saturation output power	115
	Bibliography	119

CHAPTER 1

Concepts and State-of-the-Art

This chapter introduces the concept of semiconductor optical amplifier with short explanation on the origin of amplification and description of the device. The amplifier characteristic parameters used in the following chapters are also presented. After this introduction of the device, its context of use in optical communications is given. We identify need for wideband amplifiers and current technologies blocking points. We show how semiconductor optical amplifiers could be a valid option in future wavelength-division multiplexing optical networks. We finally present previous work on wideband semiconductor amplifiers leading us to our main topic.

1.1 Semiconductor Optical Amplifier

1.1.1 Amplification medium

Two types of semiconductor materials are used in telecommunications for optical sources. Materials based on a gallium arsenide (GaAs) substrate and materials based on indium phosphide (InP) substrate. Figure 1.1 shows energy bandgap and lattice parameter for III-V compounds including GaAs and InP. Complementary optical bands can be accessed with these materials with GaAs covering 0.8 - 1.3 μm band and InP 1.3 - 1.5 μm . Different growth techniques have been elaborated

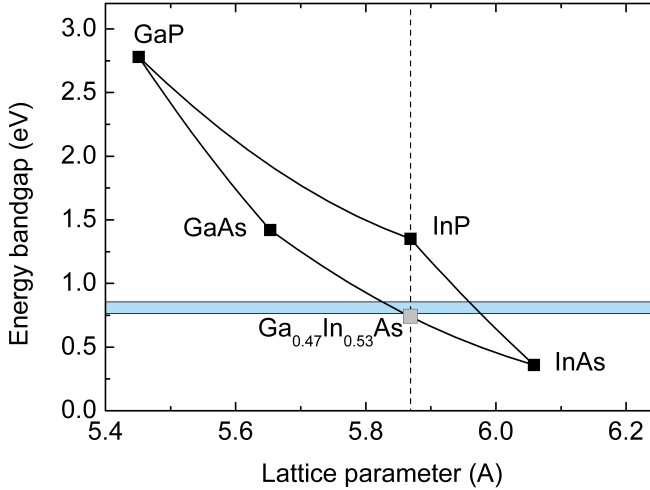


Figure 1.1 – Energy bandgap and lattice parameter of III-V compounds. Black squares give parameters of binary alloys, lines between them indicate intermediate ternary alloys. Blue area covers energies of interest for the PhD.

to obtain good quality semiconductor crystals with GaAs or InP. Both systems of material have a direct bandgap meaning that they have a conduction band (CB) and a valence band (VB) whose extremum have the same wave vector in the Brillouin zone and are separated by an energy bandgap E_g . Electric carriers injected by current can recombine and emit photons with energy close to E_g . Radiative recombination can follow two mechanisms: spontaneous emission or stimulated emission. In stimulated emission, an incident photon with energy E close to E_g triggers recombination of two electric carriers (electron and hole) generating a second photon identical to the incident photon. These coherent photons share the same phase, frequency and direction. Spontaneous emission is a random mechanism generating a photon with energy close to E_g but with random phase and direction. In both cases generated photons can participate again in stimulated emission. At the device level, repetition of the mechanism gives rise to optical gain and eventual lasing in the case of stimulated emission while repetition of spontaneous emission results in amplified spontaneous emission (ASE). Detailed explanation of recombination mechanisms can be found in [1, Ch. 1 & 4].

In order to inject electric carriers in active material for recombination, this material is sandwiched between two layers of materials with higher bandgaps, one n-doped and the other p-doped. Usually the active material itself is not a binary alloy GaAs or InP but a more complex alloy like InGaAsP in order to tune its bandgap. It is referred to as active region noted i for intrinsic material in opposition to

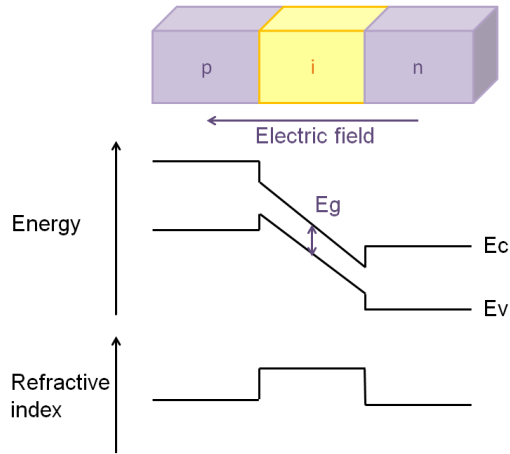


Figure 1.2 – Electron energy and refractive index for a p-i-n junction SOA structure.

doped layers. This superposition of different materials is called a heterostructure by opposition to a homojunction where all layers have an identical bandgap and composition. Two main effects arise in this structure, as shown in Figure 1.2. First carriers injection (both electrons and holes) is facilitated through a double heterojunction p-i-n and their confinement in the active region is favored by lower energy bandgap E_g . In this region both stimulated and spontaneous emissions can occur. Secondly a higher bandgap of surrounding layers (called confinement layers) also means a lower refractive index compared to the active material [24] and the heterostructure provides thus a vertical guiding of light. Waveguide can be etched and is then either surrounded by air in ridge structures or by another material in buried structures, typically InP. In both cases refractive index is lowered on the waveguide sides thus providing lateral confinement. Concentration of light in the active region statically increases probability of stimulated emission. This concentration is quantified by the optical confinement Γ which is the ratio between optical mode energy in active zone and total optical mode energy. Figure 1.3 presents a visual representation of Γ in active region and shows refractive index distribution in the structure. Γ is usually given in percentage.

Active region can be an uniform material with typical thickness of 50 to 500 nm, called bulk material. However structures based on multiple quantum wells (MQW) have been developed since the 1980s. A quantum well is a stacking of a thin layer of thickness in the order of 10 nm called well surrounded by two barrier layers of materials with higher bandgap energy. Carriers are therefore confined in the well and due to its small thickness they can only occupy some discrete energy levels. This phenomenon referred to as quantization of energy levels has been

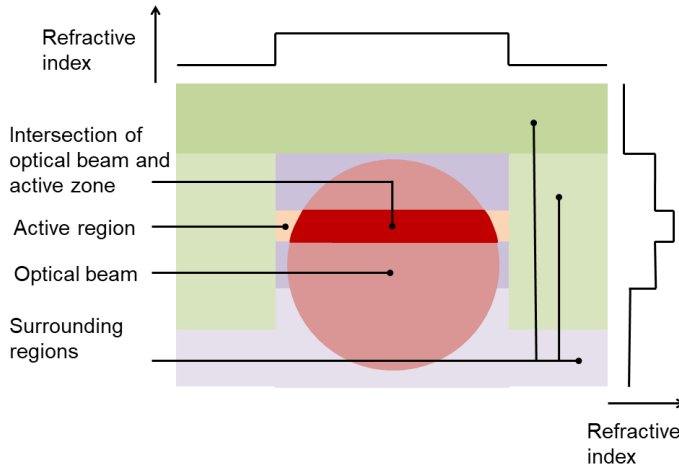


Figure 1.3 – Optical confinement Γ , given by the ratio of bright red and light red regions. Refractive index distribution is also indicated on the sides.

largely documented and its derivation can for instance be found in [1, Ch. Appendix 1]. High carrier density can thus be reached at these particular energy levels and increase radiative recombination efficiency due to efficient spatial confinement of both carriers. MQW are composed of several QWs on top of each other.

In QWs carriers are deprived of one degree of freedom. It is possible to deprive them of two or even three degrees of freedom in so called quantum wires and quantum dots (QD) illustrated in Figure 1.4. In QDs active material is reduced to a "0D" element surrounded by materials with higher energy bandgaps. It creates a multidimensional confinement causing a quantization of energy states in all three dimensions: all carriers are in the same energy state which further improves the effect on efficiency already observed in QWs. However technical realization of regular QDs distribution on a substrate is difficult and optical confinement can hardly exceed a few percents resulting in poor overall optical gain for a given current compared to bulk or QW SOAs.

1.1.2 Semiconductor optical amplifier operation

Semiconductor optical amplifiers (SOAs) are composed of an active waveguide delimited by two anti-reflection coated facets. Their structure is similar to a Fabry-Perot laser which first led to name them laser amplifiers in the 1960s, except there is no resonant cavity. Photons injected at one facet are amplified by stimulated emission in a single path and collected at the other facet. First gain materials were

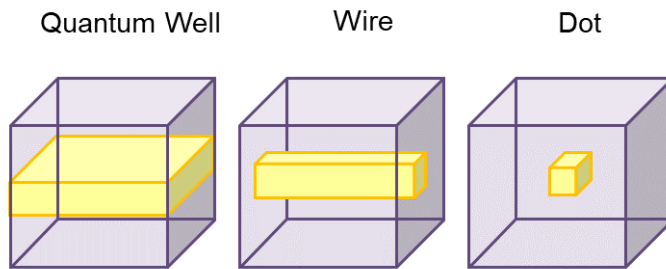


Figure 1.4 – Multidimensional carrier confinement in quantum well, wire and dot.

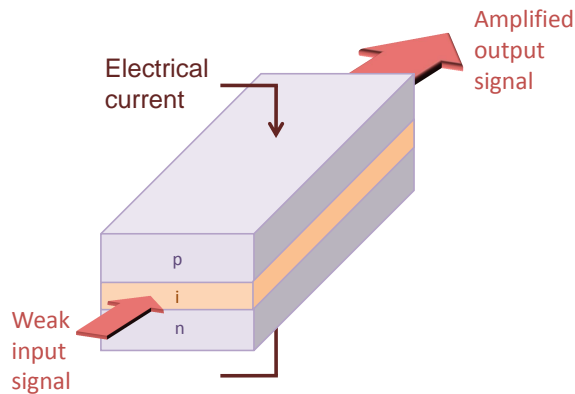


Figure 1.5 – Semiconductor optical amplifier.

made of GaAs homojunctions [25,26], later replaced with heterostructures [27–31]. Nowadays commercially available InP/InGaAsP SOAs provide amplification in the $1.3\ \mu\text{m}$ - $1.5\ \mu\text{m}$ range [2].

For a long time main difficulty was to reduce reflections at input and output facets to avoid lasing in a cavity. Thanks to great improvement of anti-reflection coatings in the 1980s devices have evolved toward high gain SOAs with very little reflectivity at their facets [32–34]. SOA waveguides usually do not have a particular direction of use but for clarity we will use in the following sections the terms input facet and output facet to distinguish between waveguide sides where optical signal is injected and collected.

Amplification in SOA can occur when an optical signal with wavelength correspond-

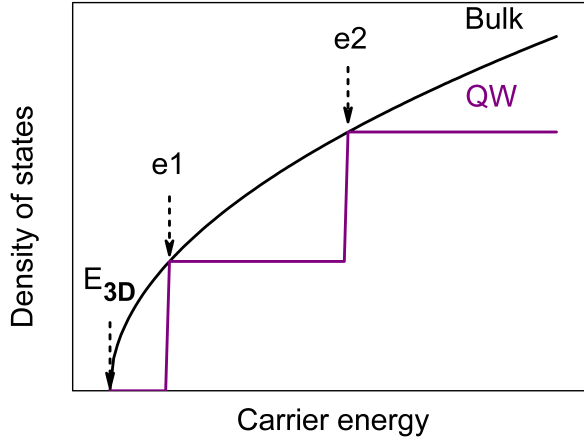


Figure 1.6 – States density dependence on energy for bulk and quantum well structures.

ing to a photon energy close to the bandgap energy of the SOA active material is injected at the SOA input facet. Electrical current applied in SOA active region increases carrier density up to population inversion allowing for amplification of the optical signal when stimulated emission compensates absorption and losses. Amplified signal is collected at the SOA output facet. Schematic representation of an SOA is given in Figure 1.5. Typical gain values for SOAs are between 20 and 30 dB over 30 to 80 nm of optical bandwidth [2, 3].

SOAs made from bulk, quantum wells or quantum dots active regions will present different properties. Due to thickness of their active layer bulk SOAs must usually operate at higher current to reach sufficient carrier density. Furthermore their density of states is continuous whereas QW SOAs have a staircase like density of states due to quantization, as shown in Figure 1.6. This particular shape allows to fill fewer states without gain in QW SOAs, thus increasing carrier injection efficiency. This effect is even stronger in QD SOAs. However, due to smaller dimensions of active material, optical confinement Γ is lower in QW SOAs than in bulk SOAs and even lower in QD SOAs. We will see in the next paragraph that it makes saturation output power greater in QW and QD SOAs. It is also interesting to note that QD SOAs gain can also be broadened by the inhomogeneous distribution of QDs size, composition, shape and strain [35]. Lastly multilayer structures used in QW and QD SOAs give the opportunity to introduce strain in the material resulting in the ability to control polarization sensitivity [36, Ch. 6].

1.1.3 Device characteristics

SOAs have three main parameters. First of them is fiber to fiber gain G which characterizes amplification by the SOA. It is defined as the ratio of signal output power P_{out} over the signal input power P_{in} and given in dB. The term fiber-to-fiber refers to gain value after coupling of the device in opposition to intrinsic gain value G_{chip} which does not have a practical application. With the hypothesis of an homogeneous carrier density, gain of the SOA can be derived as follows [37, Ch. 11],

$$G_{chip}(n) = \exp[(\Gamma g_m(n) - \alpha(n))L] \quad (1.1)$$

$$G(n) = C_1 C_2 G_{chip}(n) \quad (1.2)$$

with $g_m(n)$ material gain, $\alpha(n)$ losses, L waveguide length, and C_1 and C_2 respectively input and output coupling ratio between SOA and optical fibers (between 0 and 1). Loss coefficient $\alpha(n)$ comprises a waveguide intrinsic part and another part which depends on carrier density. α is mainly due to intervalence band absorption in both active layers and p-doped material.

This expression shows how high material gain, coming from large carrier density, and high optical confinement participate together to greater gain value. On the other hand losses tend to lower gain. Gain optical bandwidth is defined as the range of wavelengths around gain peak with gain higher than half maximum gain. In decibel scale it corresponds to all wavelengths with less than 3 dB gain difference with gain peak.

Second parameter of importance is the noise figure (NF) which quantifies noise brought to signal by the amplifier. It is defined as,

$$NF = \frac{SNR_{in}}{SNR_{out}} \quad (1.3)$$

with SNR_{in} and SNR_{out} corresponding to electric signal-to-noise ratios before and after the SOA. Equivalence between this electrical approach and an optical approach can be shown [38] and NF can be derived as follows [39]. It is important to note that input coupling losses must be taken into account in the NF derivation.

$$NF(n) = \frac{1}{C_1} \left(\frac{2P_{ASE}(n)}{G_{chip}(n)h\nu B_0} + \frac{1}{G_{chip}(n)} \right) \quad (1.4)$$

with $P_{ASE}(n)$ ASE power, $h\nu$ energy of amplified photons and B_0 filter bandwidth. We have $P_{ASE}(n)/B_0$ corresponding to the ASE spectral density. First term in equation 1.4 corresponds to signal-spontaneous emission beat noise and second term to shot noise. The latter can be neglected in high gain SOAs. Principal contribution to NF comes from beating between amplified signal and ASE [40].

ASE power can be written $P_{ASE}(n) = h\nu(G_{chip}(n) - 1)n_{sp}(n)$, leading to another expression of noise figure [41],

$$NF(n) = \frac{2(G_{chip}(n) - 1)n_{sp}(n)}{C_1 G_{chip}(n)} \quad (1.5)$$

with $n_{sp}(n)$ population inversion factor. This factor decreases when absorption becomes negligible compared to stimulated emission. In other words population inversion gets closer to 1 at high carrier density when electric carriers fill fundamental energy level. Expressions of $n_{sp}(n)$ can be found in [42, 43] and write:

$$n_{sp}(n) = \frac{n}{n - n_0} \frac{\Gamma g_m(n)}{\Gamma g_m(n) - \alpha(n)} \quad (1.6)$$

$$= \left[1 - \exp\left(\frac{h\nu - \Delta E_f}{kT}\right) \right]^{-1} \frac{\Gamma g_m(n)}{\Gamma g_m(n) - \alpha(n)} \quad (1.7)$$

In the first expression n_0 is the transparency carrier density where the stimulated emission becomes greater than absorption. At high carrier density, in case of total population inversion when excited energy level is more populated than fundamental level and if the propagation losses are negligible compared to the modal gain $\Gamma g_m(n)$, n_{sp} tends towards $n_{sp} = 1$. In the second expression ΔE_f is the difference between quasi-Fermi levels in the conduction and valence band. This second expression clearly shows the origin of the NF dependence on wavelength with $n_{sp}(n)$ being higher at shorter wavelengths.

For high values of gain, noise figure expression can be simplified and we obtain [41, 44]:

$$NF(n) = \frac{2n_{sp}(n)}{C_1} \quad (1.8)$$

Theoretical limit of NF is reached for perfect optical coupling at $C_1 = 1$ and $n_{sp} = 1$, leading to $NF = 2(3 \text{ dB})$. In practice SOA NF values are typically between 5 and 10 dB. To reduce NF it is crucial to keep input coupling losses as low as possible and to ensure high carrier density.

Finally a third useful parameter of SOA is its saturation output power P_{sat} . It is defined at a given carrier density and temperature as the output optical power for which the amplifier gain is half its nominal value G_0 . Its derivation can be found in Appendix B and leads to the following expression,

$$P_{sat} = \ln(2) \frac{A}{\Gamma} \frac{h\nu}{a_1 \tau} \frac{G_0}{G_0 - 2} \quad (1.9)$$

with $A = \text{width} \times \text{thickness}$ the section of the active region, a_1 the differential of g_m with respect to n , τ carriers lifetime and G_0 nominal gain value at the considered carrier density. High P_{sat} is desirable to extend linear regime of SOA. Section 2.2 presents development of high power SOA by decreasing Γ and increasing A .

1.2 Applications in Telecommunications

1.2.1 Optical telecommunications

Since the beginning of internet, the amount of transferred data has been constantly increasing. In the 2000s an acceleration of the phenomenon has started thanks to new technologies that have made greater bandwidth available and due to large diffusion of internet professional and domestic uses. Figure 1.7 illustrates exponential growth of internet traffic between years 2000 and 2014. Monthly data rate went from 75×10^6 GB in 2000 to 42×10^9 GB in 2014, an increase of more than 550 times its initial value. During the same period, global number of internet users has been multiplied by 921 and average traffic per user by 6,113 [45]. Forecasts for the next couple of years still predict always growing volumes. In order to keep up with this quick pace, optical transmission systems which provide most of the world's connections must constantly evolve.

From first optical transmissions to nowadays complex networks, big developments have already changed the way data circulate around the world. Different axis have permitted to increase traffic rate. First wavelength-division multiplexing (WDM) which makes use of several wavelengths for parallel transmissions. Total data flow rates is then multiplied by channels number. Going hand in hand with increase of spectral density, this technology has permitted to greatly improve data traffic rate.

Among other developments, design of optical devices compatibles with high data flow rates have contributed to networks improvement. State-of-the-art photo-receptors and modulators can for instance work with modulation frequencies higher than 100 Gb/s and 50 Gb/s respectively [46–49]. Starting with modulation of amplitude, optical transmissions have first moved to phase modulation, then polarization modulation and to multilevel modulation. Basic non-return-to-zero (NRZ) code has made way for multilevel amplitude modulation like PAM-4 or quadrature amplitude modulation like QAM64. Evolution of modulation formats toward more complex constellations diagrams which transmits more data has also allowed quicker transmissions.

These three axis of development are combined together for even better performances. However these data flow rate improvements come at a cost as they may require complex optoelectrical components. Depending on expected performances and cost options different solutions coexist consequently in optical networks. We distinguish three networks levels: Long Haul, Metro and Access. Long haul corresponds to high capacity links for intercontinental or interstate distances which usually includes in-line repeaters. Metro corresponds to smaller distances of about 100 km and Access to connection to end-users for distances below 20 km. Expected

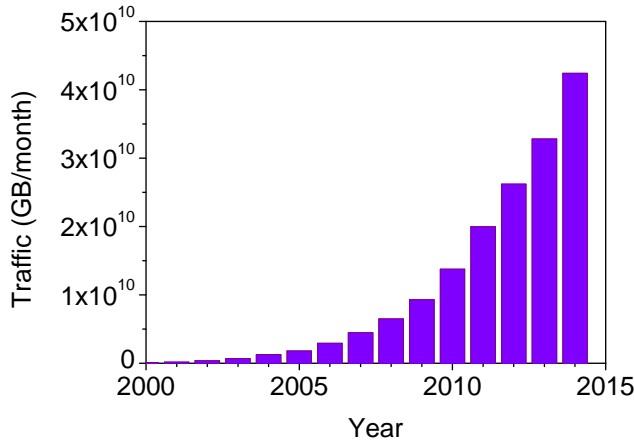


Figure 1.7 – Exponential increase of monthly data traffic between 2000 and 2014. Source: Cisco blog [45].

performances on these optical networks are fixed by standards given by the International Telecommunication Union (ITU) in order to ensure compatibility of optical networks around the world. They adjust through time to prepare the future of optical communications. A discussion of standards evolution can be found in [50, Ch. 18]. In this work we focus on WDM systems and their use in both long haul and access applications.

1.2.2 Wavelength-division multiplexing systems

Main transmission mean in optical communications is optical fiber. Since first transmissions, optical fibers have evolved to reduce propagation losses and chromatic dispersion which distort transmitted signals. Figure 1.8 presents propagation losses of commercial optical fibers at different wavelengths. Chromatic dispersion (CD) in commercially available fibers is displayed in Figure 1.9. Close to zero around 1300 nm, CD increases with wavelength and reaches 16 ps/(nm.km) at 1550 nm. Because of its zero dispersion and moderate optical losses, O-band located between 1260 and 1360 nm was originally used.

O-band is notably used in access networks as its zero dispersion allows use of low cost and less precise transmitters like directly modulated lasers (DML). Cost is a critical parameter for access networks as a great number of components is needed to distribute signal to all users. Other components were later developed for use in

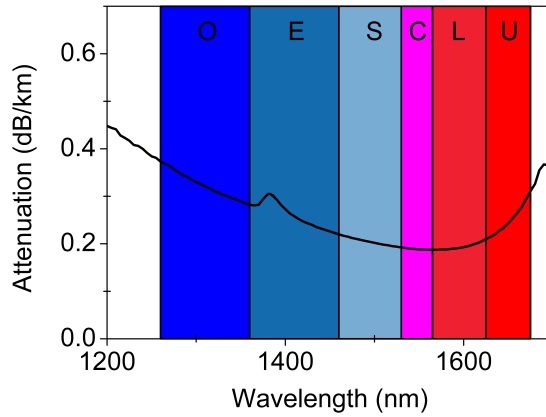


Figure 1.8 – Optical fiber losses around 1550 nm.

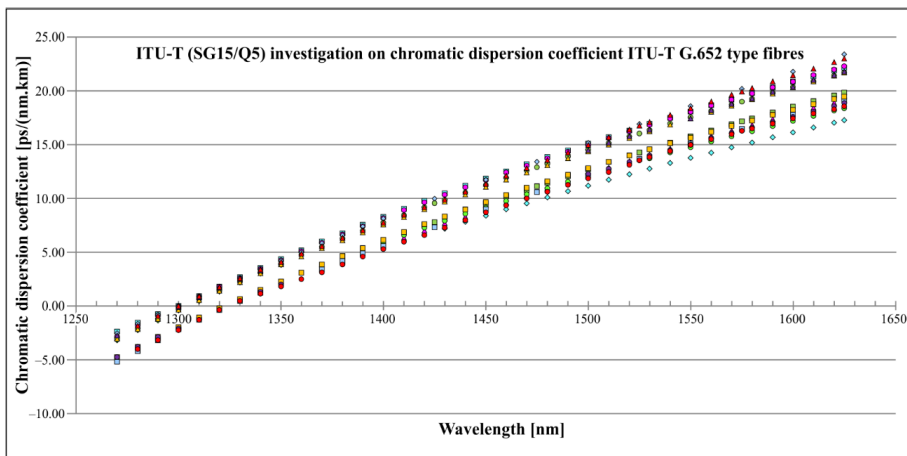


Figure 1.9 – Maximums and minimums of chromatic dispersion in commercially available optical fibers. Each color corresponds to a different vendor. Source: ITU Recommendations G652

O-band (Original)	1260-1360 nm
E-band (Extended)	1360-1460 nm
S-band (Short)	1460-1530 nm
C-band (Conventional)	1530-1565 nm
L-band (Long)	1565-1625 nm
U-band (Ultra-long)	1625-1675 nm

Table 1.1 – Telecommunication optical bands

the C-band (between 1530 and 1565 nm). Table 1.1 presents telecommunication optical bands with corresponding wavelengths. To this day access networks did not need amplifiers but evolution of standards and development of fiber-to-the-home (FTTH) require their use. For cost reasons use of bidirectional amplifiers to amplify both upstream and downstream signals is studied. In proposed Next Generation Passive Optical Network 2 (NG-PON2) these bandwidths start at 1524 nm for the upstream and expands till 1603 nm for the downstream therefore requiring a wideband amplifier [22].

In the case of long-haul transmissions it is important to transmit as many channels as possible to increase total data rate. In these dense WDM transmissions, having a bit of dispersion is paradoxically useful as it prevents cross-talk between adjacent channels which propagate at different speeds. For this reason O-band was abandoned for C-band, a minimum for optical losses with higher chromatic dispersion. Long-haul networks are made of multiple spans of about 100 km and signal is amplified between each span. In long-haul applications amplifiers must have high gain to compensate for long distance losses and high saturation output power to amplify a great number of channels. Network structure also makes noise figure of the amplifiers a critical parameter as noise is added in each span.

In the 1990s the invention of erbium-doped fiber amplifiers (EDFAs) and their commercialization have permitted transmission over longer distances and multiwavelength operation on a single fiber [51, 52]. EDFAs are composed of a glass doped with Er^{3+} ions whose most accessible transition between energy levels (${}^4I_{13/2} \rightarrow {}^4I_{15/2}$) corresponds to a wavelength between 1530 and 1600 nm depending on the glass composition. It makes EDFAs particularly adapted for amplification in optical fiber as they can cover the C-band. To fill the excited level with carriers, the EDFA is pumped with a laser of higher energy, usually at 980 nm. Excited carriers can then decay from higher energy levels to level ${}^4I_{13/2}$ and participate in stimulated emission at 1550 nm [53, Ch. 11].

Before their invention it was not possible to simultaneously amplify optical signals

at different wavelengths so each signal had to be converted into electronics at each repeater. EDFAs have therefore led to a simplification of amplification in WDM transmissions. First field trials of WDM systems including EDFAs were presented in 1990 by Bell Labs [54]. Since then they have been broadly deployed and extensively studied for WDM applications in the C-band [55,56]. Laser sources are also easily available in this region which further participated in the choice of C-band for most transmissions.

To keep up with increasing demand on high speed transmissions, spectral efficiency of C-band transmissions has been constantly improving by combining higher level modulation formats with dense WDM and higher flow rate, by forward error-correcting codes (FEC) and more recently by coherent detection. Nevertheless in the last few years spectral efficiency seems to be reaching a plateau. New solutions must be found to cope with predicted augmentation of data flow rate. One of the best options could be an extension of optical bandwidth outside C-band [57]. Available optical bands which have not been used so far can be seen in Figure 1.8. Use of extended telecommunication bands, namely C+L-band or even S+C+L band would allow insertion of more DWDM channels without reaching regions with high optical fiber losses.

Typical EDFA bandwidth is 40 nm centered in the C-band or L-band but extended bandwidths of 75 nm have been demonstrated by associating a C-band EDFA with a L-band EDFA [58,59]. This approach involves a complex set-up and moreover it only doubles the optical bandwidth when it should be multiplied by at least three to cover an extended S+C+L band. EDFA can reach high gain between 20 and 50 dB depending on the pumping power, with maximal gain efficiency in the order of 1 dB/mW [55,60,61]. For large gain and high pump power, NF of an EDFA drops and can nearly reach theoretical limit of 3 dB but usual values are comprised between 4 and 6 dB [53,61,62]. All these characteristics have made them an essential device for long-haul transmission and the most used optical amplifier. However they are intrinsically limited to operate only in the C-band or L-band. To develop DWDM in extended bandwidths a new amplification solution must be found.

Could SOA be a valid solution for wide amplification required in access and long-haul transmissions?

1.2.3 Semiconductor Optical Amplifiers in Telecommunications

Since their invention in the 1960s SOAs have been a subject of interest for optical communications due to promising features. Their small size and semiconductor

SOA	EDFA
Gain > 25 dB	Gain > 24 dB
Must be used in linear regime with $P_{sat} < 20$ dBm	Can be used in saturated regime with output power > 20 dBm
6-8 dB NF	4-6 dB NF
~ 80 nm bandwidth between 1250 and 1600 nm	~ 40 nm bandwidth in C-band or L-band
Polarization dependence varies with design	Polarization independent

Table 1.2 – Comparison of SOA and EDFA typical amplifier characteristics.

composition make them easy to integrate in photonic integrated circuits (PICs). They have soon earned the role of laser booster-amplifiers [63] and photodetector pre-amplifiers [64]. They can also be used in non-linear regime for complex functions like wavelength conversion or logic-gate functions [65,66].

EDFAs have so far been preferred for inline amplification due to their high gain, low noise figure, polarization independence and ability to operate under saturation regime. Table 1.2 compares relevant characteristics of SOA and EDFA [67]. SOAs are penalized by poor noise figure, operation regime restricted to linear regime and polarization dependence for most designs. Yet with large bandwidths, SOAs show promises for WDM systems. Their ability to operate on a bandwidth of about 80 nm anywhere between 1250 nm and 1600 nm gives them great flexibility. Such wideband amplifiers could be used in future access networks [21,68] and SOA make good reach extender candidates for fiber-to-the-home (FTTH) applications [69] and future exploration of extended telecommunication bands.

To go further and imagine use of SOA in future WDM systems with large optical bandwidth and high number of channels, several challenges must be resolved. First a larger optical bandwidth of more than 100 nm must be obtained to overcome stagnation of spectral density by adding more channels. Then performances comparable to EDFAs in terms of gain, saturation output power and noise figure must be reached to easily integrate SOAs in optical networks. Third polarization dependence must be mitigated for in-line amplification. Following section presents what has been proposed so far to increase SOA bandwidth above 100 nm.

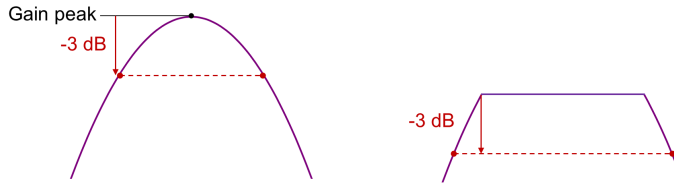


Figure 1.10 – Broadening of bandwidth by gain truncation.

1.3 Wideband Semiconductor Optical Amplifier State of the Art

Very diverse solutions have been explored to increase SOA bandwidth. We propose a non-exhaustive review of well-known solutions in literature and leads developed internally at III-V Lab. Given potential applications of SOA covering C+L band, III-V Lab has indeed started long ago to study large bandwidth SOAs. Some of the given options resulted in large bandwidth but we will see that none of these solutions was able to provide desired specifications for implementation in WDM optical networks.

1.3.1 Integrated filters

For an SOA polarized at a given current, optical bandwidth is defined as wavelength range with gain within 3 dB of gain peak value. SOA gain spectra have parabolic shapes and as illustrated in Figure 1.10 they quickly broaden below gain peak value. If we could truncate upper part of the gain spectrum it would turn into a flat trapezoidal shape with a larger 3 dB bandwidth. Figure 1.10 schematically illustrates this idea. However truncating the spectrum also lowers maximum gain value meaning that trade-off between large bandwidth and high gain should be found.

Requested trapezoidal shape could be obtained with integrated optical filters, that introduce losses at gain peak wavelengths and level total gain spectrum. Distributed Bragg reflectors (DBRs) were at first good candidates and Figure 1.11 presents a scheme of an SOA with integrated DBR. Additionally for this application DBR must be tilted so that filtered signal is radiated away to avoid lasing. Such structures were made at III-V Lab with different tilt angles. Figure 1.12 displays pictures of three of these structures. Unfortunately none of the devices worked properly. When tilted angle was high enough to avoid lasing it decreased filter efficiency. No

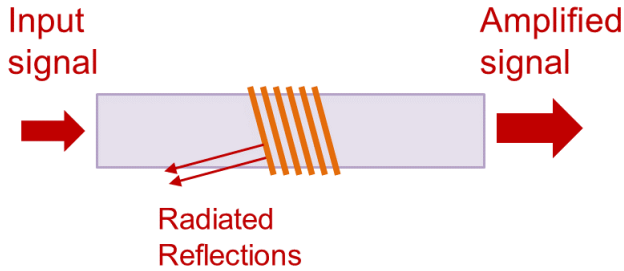


Figure 1.11 – Integrated distributed Bragg reflector for gain leveling.

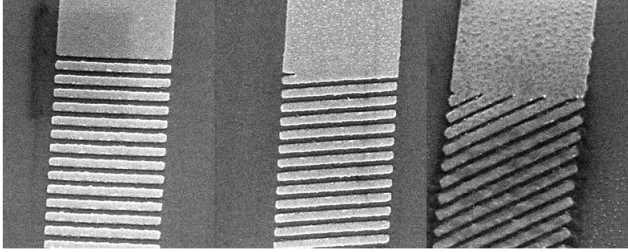


Figure 1.12 – Pictures of three integrated DBR with different tilts made at III-V Lab.

trade-off could be found for these structures.

Another option was to use photonic crystals, periodic structures designed to act as filters at specific wavelengths. Despite good results the idea was abandoned due to complexity of fabrication process and difficulty to obtain reproducible performances.

It is difficult to integrate filters into an SOA waveguide without disturbing signal transmission. However this idea can more easily be applied to reflective SOAs (RSOAs). These devices are very similar to SOAs but with one reflective facet. Signal input and output are thus on the same side. RSOAs notably find application in tunable external cavity lasers in which a broadband gain is desirable to extend laser tuning range but they can also be used as broadband light sources. Compared to SOA, reflective facet of RSOA offers one degree of freedom more for integration of an optical filter. Reflective facet is indeed located half-way through light path in the device but is easily accessible and high reflectivity is not a problem compared to SOA. Three possible filters were studied at III-V Lab, beginning with DBR placed this time at the reflective facet to enhance reflectivity at a specific wavelength and thus gain. By choosing this wavelength at the limit of optical spectrum, the

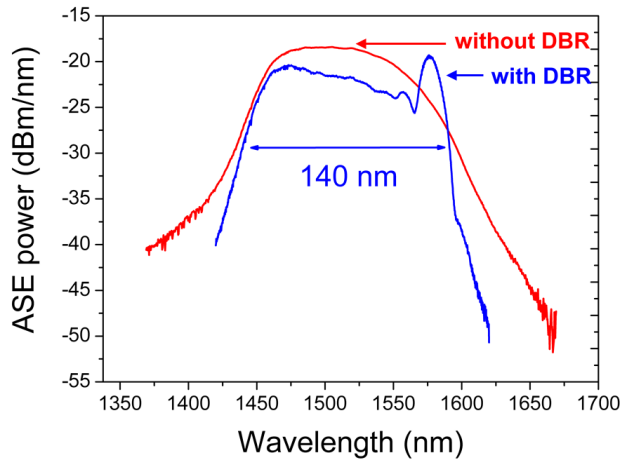


Figure 1.13 – Emission spectrum of SOA with and without DBR

later is slightly extended. Figure 1.13 shows comparison of a regular SOA emission spectrum with the one of an SOA with DBR designed to operate at 1580 nm. A peak is clearly visible at this wavelength and extends emission bandwidth to 140 nm. This device cannot be used as an SOA due to big variations in its spectrum amplitude but its wide emission spectrum makes it a very good superluminescent light-emitting diode (SLED).

Second option is a filtering reflective coating at the back facet of the RSOA as represented in Figure 1.14 b). Coatings are made of thin stacked layers of oxides (SiO_2 and TiO_2). Both reflective and anti-reflective coatings can be made with this method. Simulations have showed possibility to filter central wavelengths with an elaborate coating including more layers. Figure 1.14 a) shows a simulation of the extreme case where the filter completely cuts one wavelength. For our application the shape of the filter had to be adapted to the gain spectrum without completely canceling central wavelength reflectivity. Nevertheless this coating process was too complex and sensitive and after unsuccessful trials it was decided to try another approach.

In final option output of the SOA is coupled to a multiplexer splitting signal into different channels, then reflected and multiplexed back into the SOA. This solution is schematically represented in Figure 1.15. Depending on wavelength each channel is sent to a variable reflector which levels signal power to the same value. At recombination all channels have thus same power level. Figure 1.16 shows amplification of six channels by the same C-band SOA with and without variable reflectors. With

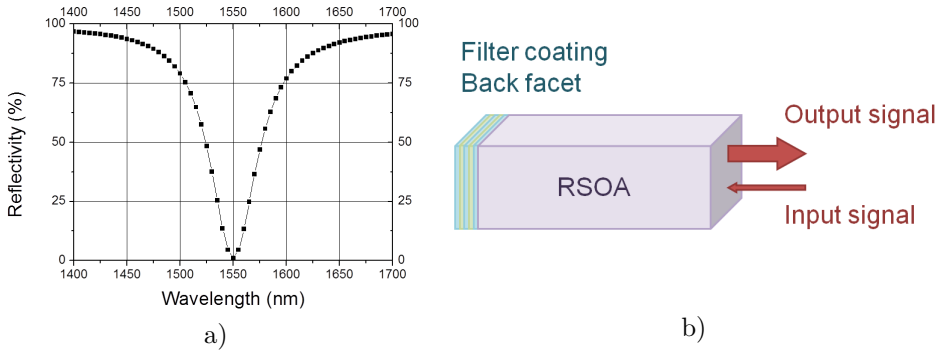


Figure 1.14 – a) Simulation of filter coating reflectivity b) Schematic of RSOA with filter coating.

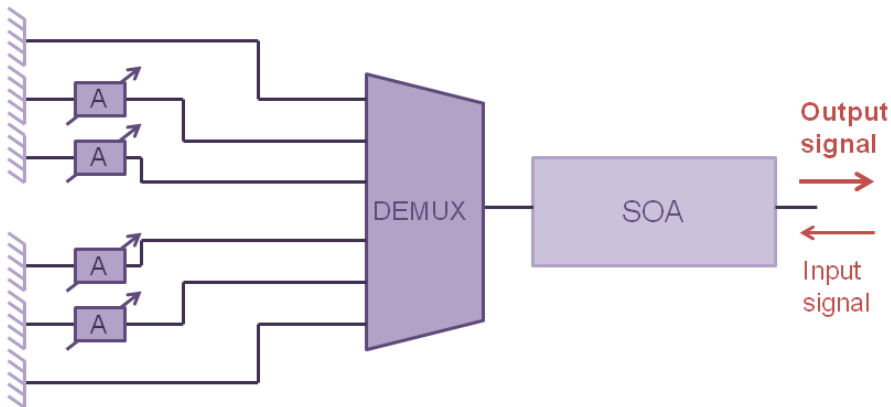


Figure 1.15 – Six variable reflectors equalize SOA gain on a large bandwidth.

this system amplified channels present less than 3 dB difference versus 10 dB for without variable reflectors. Signal power is of course leveled at lowest channel value which might be problematic for gain specifications. This solution shows promising results but is not an integrated solution and therefore does not fulfill required specifications.

Putting in application gain spectrum truncation is technologically complex and shows little results for transmission SOAs. Variations of this idea for RSOA show promising results for application as SLED or tunable laser. Instead of extending SOA bandwidth by considering its largest part, why not join two regular SOA bandwidths in a single device?

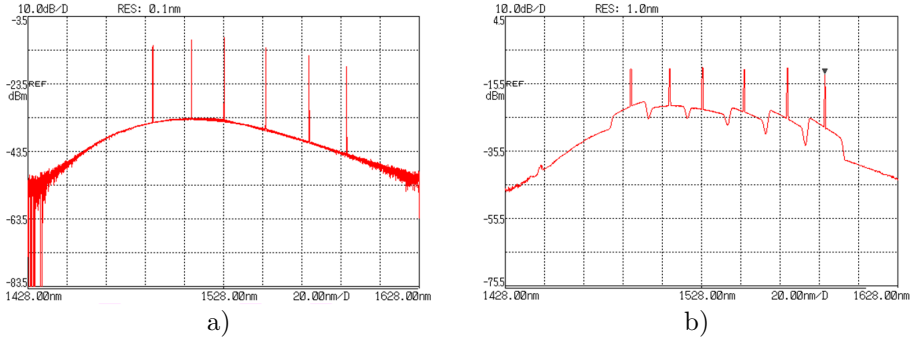


Figure 1.16 – Amplification of six channels a) without variable reflectors and b) with variable reflectors

1.3.2 Dual SOA

A straightforward solution consists of using two SOAs with adjacent optical bandwidths and allocate half bandwidth of interest to each SOA. A demultiplexer and a multiplexer are used to split signal in two depending on wavelength. Figure 1.17 a) displays the case of S+C band amplifier with chosen SOAs at 1450 nm and 1500 nm respectively. Figure 1.17 b) shows resulting amplifier optical bandwidth of about 120 nm. This solution efficiently provides a device with large optical bandwidth. But in order to center the SOAs at distinct wavelengths, composition of the active regions must be different. It makes integration of the dual SOA device complicated as two different material growths must be realized. This issue makes this dual SOA fabrication more complicated or impose a more complex approach based on hybrid integration of discrete elements. Furthermore when the SOAs gain bandwidths overlap as in the case shown in Figure 1.17 b), if the demultiplexer does not split signal at a precise wavelength, even small phase discrepancy at recombination can cause interferometric noise and perturb signal in the overlap region. Devices with separate SOA bandwidths like for instance a O+C dual SOA, do not encounter this issue but are also less relevant for required application.

To avoid complicated epitaxial growth of two parallel SOA active regions one may think of stacking both regions vertically instead of placing them in parallel. Regions of different materials in the case of bulk SOA or quantum wells of same composition but different thicknesses in the case of QW SOA can be imagined. Figure 1.18 illustrates the latter. However these heterogeneous structures have different density of states and non-uniform carrier density in the QWs which degrade broadband properties. Lin et al. showed influence of stacking order on broadband operation in such structures [70]. Because wells positioned near n-doped layer trap carriers first, thicker wells with lower energy levels must be placed closer to n-doped layer to

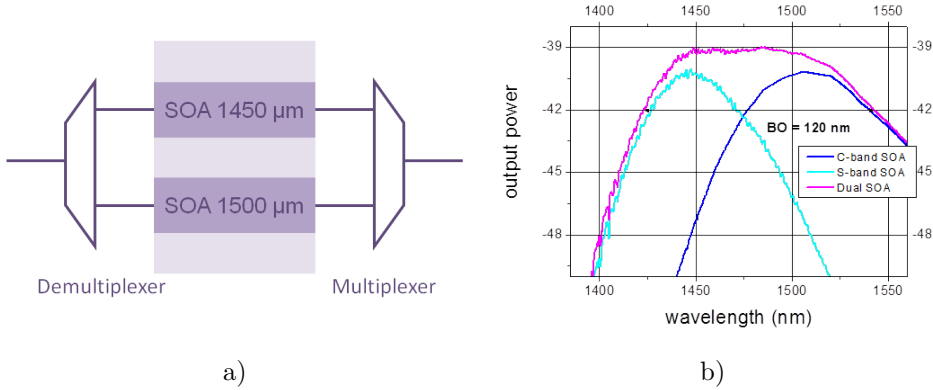


Figure 1.17 – a) Dual SOA representation. b) Dual SOA optical bandwidth.

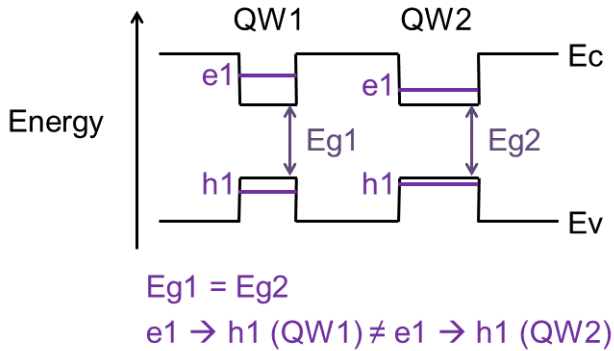


Figure 1.18 – Quantum wells with identical composition but different thickness.

insure sufficient gain at corresponding wavelength. When carrier density increases carriers reach thinner quantum wells with higher energy levels. Gain increases quickly at corresponding wavelength resulting in an extended optical bandwidth. With this method Lin et al. realized a broadband SOA used in a tunable external-cavity laser with tuning range of 240 nm [71]. Difficulty for this kind of structure lies in the control of QWs composition and thickness for a balanced structure with sufficient gain at all wavelengths.

An elegant solution to integrate different material structure on a sole device is allowed by selective-area-growth (SAG) technique. SAG allows to vary deposition rate on a wafer by using oxide mask patterns and MOVPE selectivity [72]. Using this technique thickness and composition of quantum wells can be changed along a

propagation axis, then processed into a waveguide. A broadband gain material has been obtained with this method by Zhang et al. to realize a tunable laser of 200 nm tuning range [73]. Use of this technique for SOA seems however complicated as regions emitting at high wavelengths likely absorb lower wavelengths. A structure with small energy transition region first will absorb input signal at lower wavelength. But if this region is positioned at the end it will absorb amplified signal at lower wavelengths. In both cases having a flat gain over a wide bandwidth is close to impossible. This is why this structure can only be used as gain material and without specification on flatness.

Joining different active structures in a single device efficiently extends optical bandwidth, but control of gain flatness remains difficult. Other teams have focused more on optimization of a given material to push performances to their limits.

1.3.3 Quantum dots and multiquantum wells SOA

As presented in Section 1.1 QDs SOAs can have very flat gain spectra. Thanks to this property large -3 dB-bandwidth of about 80 nm have been obtained for QD SOA by Akiyama et al. [74]. These SOAs also exhibited large gain and high saturation output power, but due to QD material growth mode the SOAs were polarization dependent and mainly amplified transverse electric (TE) polarization. Further work on the topic has led to polarization independent QD SOA with 80 nm gain bandwidth [75]. This is still below the objective of 100 nm and NF of 9.5 dB of these QD SOAs remains too high.

In 2005 Morito et al. presented a MQW SOA with wide gain bandwidth, high saturation power and low NF [4, 5]. To reduce NF while keeping a low confinement factor, effort was put in reducing propagation losses to keep $\frac{\Gamma g_m(n)}{\Gamma g_m(n) - \alpha(n)}$ in Equation 1.6 as low as possible and thus low n_{sp} . Meanwhile thin 5 nm quantum wells were designed to obtain good separation of energy levels and benefit from quasi constant state density of QW SOAs. Resulting SOA has a 120 nm optical bandwidth between 1450 and 1570 nm with a 18 dB gain peak, saturation output power of 19.6 dBm and NF below 4.5 dB. These results remain up to this date among best performances for large band SOA. However we will see in the next chapter limitations of this approach.

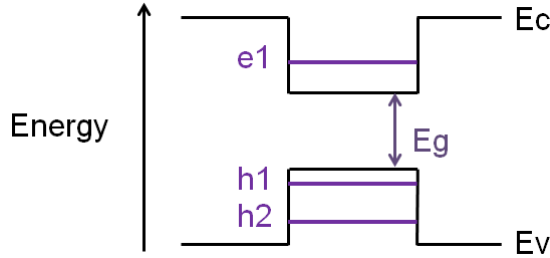


Figure 1.19 – Quantum well with two hole energy levels.

1.4 Context of the PhD

Purpose of the PhD was to develop a wideband SOA for use in WDM optical networks. Required specifications for this application include gain of at least 15 dB, saturation output power above 20 dBm and noise figure below 7 dB. Main specification is a 3 dB-optical bandwidth of about 120 nm.

Many studies have already been done on the subject at III-V Lab and by other research teams as presented in previous section. Table 1.3 lists some of the most interesting results on SOAs including large band, high power or low NF SOAs. Among best results stand 5 nm-MQW SOAs developed by Morito et al. in 2005. Not only do they present excellent performances but their fabrication is also relatively simple compared to other proposed solutions. In a similar manner we chose to develop MQW SOA that would meet all specifications without requiring a complex technological processes. Results appear on Table 1.3 last line. Our technological choices will hopefully make industrialization of the device possible.

Chapter 2 presents physic principle of wideband SOA developed during my PhD.

My work during the PhD was to optimize material composition of the SOA to meet all specifications. It included working on wideband properties and mode propagation as well as improvement of saturation output power. Both aspects are presented in Chapter 2 and characterizations of the devices can be found in Chapter 3. As SOA performances also depend on the device geometry, Chapter 4 will detail this topic and propose some optimization. Finally as developed SOAs have already found some applications we will present their implementation in optical systems in the last chapter of this thesis, Chapter 5.

Laboratory	Year	Optical bandwidth	Gain	P_{sat}	NF	Material	Polarization insensitive	Reference
Bell Labs & TIT	1993	30 nm	24 dB	23 dBm	/	GaInAs MQW	Not given	[76]
Philips Optoelectronics	1996	100 nm	22 dB	13 dBm	9 dB	InGaAs MQW	Yes	[77]
Fujitsu	2003	/	19 dB	17 dB	7 dB	InGaAsP bulk	Yes	[78]
Corning	2003	35 nm	15 dB	17 dBm	6 dB	MQW	Yes	[79]
Lincoln MIT	2005	120 nm	13 dB	31 dBm	9 dB	InGaAsP MQW	No	[80]
Fujitsu	2005	120 nm	15 dB*	19.6 dBm*	4.5 dB*	InGaAsP MQW	No	[4]
Fujitsu	2005	120 nm	15 dB	22 dBm	5.7 dB	InGaAsP MQW	Yes	[5]
Fujitsu & Todai	2005	50 nm	25 dB ?	19 dBm ?	5 dB ?	InAs QDs	Not given	[74]
Fujitsu	2008	90 nm	12.6 dB	12.8 dBm	6.5 dB	GaInNAs MQW	Yes	[81]
Lincoln MIT	2008	/	13 dB	29 dBm	5.5 dB	InGaAsP MQW	No	[82]
Lincoln MIT	2009	100 nm	13.8 dB	29 dBm	5.5 dB	InGaAsP MQW	No	[8]
III-V Lab & LPCNO	2010	100 nm	/	/	/	InGaAsP MQW	Yes	[83]
IBM & HHI	2015	80 nm	27 dB*	10 dBm*	6 dB*	InGaAsP MQW	No	[84]
III-V Lab & LPCNO	2017	120 nm	18.5 dB	20 dBm	7.5 dB	InGaAsP MQW	Yes	[19]

Table 1.3 – State of the art of wideband SOAs. (*) indicates chip value instead of fiber-to-fiber value, (?) indicates lack of precision on this aspect.

Material structure of semiconductor optical amplifier

Over the course of ten years, three projects have framed researches on wideband SOAs at III-V Lab.

- Project ANR Arome (Amplificateur optique à semiconducteur pour les Réseaux Optiques Métropolitains et Accès) (2008-2010) gathering III-V Lab, LPCNO (Laboratoire de Physique Chimie des Nano-Objets), Orange Labs, LPN (Laboratoire de Photonique et de Nanostructures), IEMN (Institut d'Electronique, de Microélectronique et de Nanotechnologie) and LTCI (Laboratoire de Traitement et Communication de l'Information)
- Project Ultrawide (Amplificateur intégré ultra-large-bande pour systèmes optiques WDM améliorés) (2010-2013) gathering Alcatel-Lucent Bell Labs France, III-V Lab, Kyliya, Télécom SudParis, SUPELEC and ENIB (Ecole Nationale d'Ingénieurs de Brest).
- Project FUI Calipso (High Capacity ultra Large systems based on Integrated Powerful SOA) (2014-2017) gathering Nokia Bell Labs France, III-V Lab, Kyliya, Télécom SudParis and Egide.

Many ideas have been tested during project Arome including the ones described in previous chapter. But only one was pursued in Ultrawide and Calipso. This

original idea was to use large quantum wells with two energy transitions to induce stimulated emission at two wavelengths for a broad optical bandwidth. We will see in Section 2.1 optimization of the quantum wells and designed structures. We have previously explained the importance of saturation output power for wideband SOAs. In section 2.2 we will describe the material structure and fabrication process used to improve saturation output power.

2.1 Large-band semiconductor optical amplifier

2.1.1 Operating principle

2.1.1.1 Band Structure Engineering

One asset of compound semiconductors lies in the freedom they offer for band structure engineering. Thanks to the high control of epitaxy techniques, it is possible to artificially modify the electronic structure of semiconductor materials. This opens up an efficient and controlled way to cover continuously a broad spectral range for optical emission and absorption, and to build multilayers for various applications. Considering the natural electronic band structure of semiconductor crystals (energy bandgap, carriers mass, etc. . .) as a starting point for application in devices, a combination of strain and quantum confinement can lead to great improvements of the semiconductor device characteristics.

In other words the semiconductor band structure can be tuned in an artificial fashion to suit device specifications [85]. The main ideas of band structure engineering were originally proposed by A.R. Adams and E. O'Reilly in United Kingdom and in parallel E.O. Kane and E. Yablonovitch in USA in 1986 [86], [87]. These authors predicted that the modified band structure of strained III-V quantum well structures should lead to significant benefits for diode laser performances, i.e. reduced threshold current, improved efficiency, improved temperature sensitivity and better high speed performance thanks to a better match between electrons and holes effective masses and a reduction of Auger and inter-valence band absorption loss mechanisms [6, 85–88].

First successful application of compressive strain for 1.5 μm InGaAs/InGaAsP multiple quantum well strained lasers was demonstrated in 1989 [89]. Nowadays huge impact of strained layers is well illustrated by their use in almost all the optical devices based on III-V semiconductors for telecommunications (lasers and SOAs). Using strain in addition to MQW layers composition and thickness offers an extra degree of freedom to design our structures.

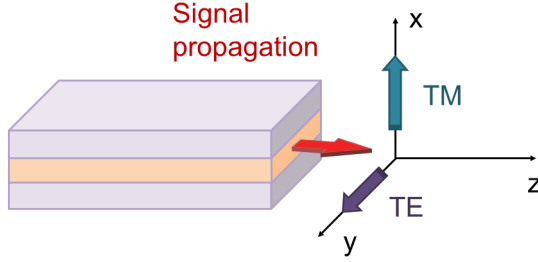


Figure 2.1 – Light propagation along x-axis and polarization representation along the axis, TE along y-axis and TM along x-axis.

2.1.1.2 Polarization Sensitivity

A critical effect of strain in MQW is to breakup holes energy levels degeneration and split heavy-hole (HH) and light-hole (LH) bands. Strain can be either compressive for a positive lattice mismatch or tensile for a negative one. Compressive strain reduces in-plane HH mass and makes heavy-hole band lie at the top of the valence band. On the contrary, in the case of tensile strain, the valence band maximum can be a LH state.

Relative position of HH and LH bands is important as transitions to one or the other will result in two different polarizations of light. To understand the origin of this effect we need to recall the principles of gain calculation in QWs, detailed in [90, 91]. Assuming that light propagates along z-axis, electromagnetic wave can either oscillate along y-axis in transverse electric mode (TE) or along x-axis in transverse magnetic mode (TM) as shown in Figure 2.1.

Material gain is calculated as follows:

$$g_m = \frac{e^2 \hbar}{m_0^2 n c \epsilon_0} \frac{1}{\hbar \omega} \frac{1}{w_{QW}} (1 - e^{-\frac{1}{kT}(\hbar \omega - \Delta E_F)}) \sum_n \sum_m \int_0^{+\infty} \frac{k_{\perp}}{\pi} |M_{nm}(k_{\perp})|^2 f(E_m^C(k_{\perp}) - E_{Fc}) \left(1 - f(E_{Fv} - E_n^V(k_{\perp}))\right) \frac{\hbar \gamma_{int}}{(\hbar \omega - E_m^C(k_{\perp}) - E_n^V(k_{\perp}))^2 + (\hbar \gamma_{int})^2} dk_{\perp} \quad (2.1)$$

where $\Delta E_F = E_{Fc} - E_{Fv}$, and with w_{QW} the quantum well width, $f(E_m^C - E_{Fc})$ and $f(E_{Fv} - E_n^V)$ the Fermi-Dirac conduction and valence band occupancy numbers. E^C and E^V are the carrier energies in conduction and valence band, respectively, and E_{Fc} and E_{Fv} are the quasi-Fermi levels of conduction and valence band, respectively. $\gamma_{int} = \frac{1}{\tau_{int}}$ is the reciprocal of intraband relaxation time. The dipole

matrix element coupling electron and hole states writes:

$$M_{nm}(k_{\perp}) = \langle \Psi_m^C | \epsilon \cdot p | \Psi_n^V \rangle \quad (2.2)$$

Here, ϵ is the light polarization. For electron-heavy hole recombination in the envelope function approximation, this latter expression can be rewritten:

$$M_{nm}(k_{\perp}) = \langle F_m^C | g_n^V \rangle \langle u_C | \epsilon \cdot p | u_{V,h} \rangle \quad (2.3)$$

and for electron-light hole recombination:

$$M_{nm}(k_{\perp}) = \langle F_m^C | f_n^V \rangle \langle u_C | \epsilon \cdot p | u_{V,l} \rangle \quad (2.4)$$

$\langle F_m^C | g_n^V \rangle$ and $\langle F_m^C | f_n^V \rangle$ are the envelope function overlaps of electronic (F_m^C) states with heavy (g_n^V) and light (f_n^V) hole states, respectively. $\langle u_C | \epsilon \cdot p | u_V \rangle$ depends on the wave polarization and on the periodic Bloch functions of the conduction and valence band edges, its values for propagation along z-axis are given in Table 2.1 [92]. We have,

Polarization:	ϵ_x	ϵ_y	ϵ_z
Transition $e \rightarrow hh$	forbidden	$\frac{\Pi}{\sqrt{2}}$	impossible
Transition $e \rightarrow lh$	$\frac{2\Pi}{\sqrt{6}}$	$\frac{\Pi}{\sqrt{6}}$	impossible

Table 2.1 – Selection rules for interband transitions obtained from the absolute value of the matrix element $\langle u_C | \epsilon \cdot p | u_V \rangle$ in $k_{\perp} = 0$.

$$\Pi = \frac{-i}{m_0} \langle S | p_x | X \rangle = \frac{-i}{m_0} \langle S | p_y | Y \rangle = \frac{-i}{m_0} \langle S | p_z | Z \rangle \quad (2.5)$$

with $|S\rangle$, $|X\rangle$, $|Y\rangle$ and $|Z\rangle$ the band edge Bloch functions of s-like conduction band and p-like valence band at Γ point.

In the considered case of propagation along z-axis, only TE mode is allowed (polarization along y-axis) for electron-heavy hole recombinations ($e \rightarrow hh$). For electron-light hole recombination ($e \rightarrow lh$), both polarizations are possible (electric field along y-axis (TE) or along x-axis (TM)). Hence, for TE mode, transition matrix element writes:

$$|M_{nm}^{TE}(k)|^2 = \Pi^2 \left(|\langle F_m^C | g_n^V \rangle|^2 + \frac{1}{3} |\langle F_m^C | f_n^V \rangle|^2 \right) \quad (2.6)$$

TM emission is only due to electron-light hole recombinations. In these recombinations the corresponding TM transition is twice more intense than for TE polarization emission:

$$|M_{nm}^{TM}(k)|^2 = \frac{2\Pi^2}{3} |\langle F_m^C | f_n^V \rangle|^2 \quad (2.7)$$

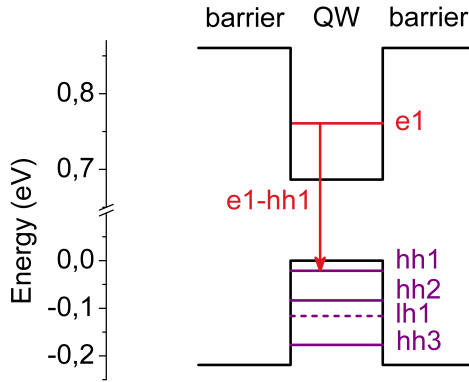


Figure 2.2 – Simulated energy levels for a 5 nm InGaAsP quantum well with well material $In_{0.673}Ga_{0.327}As_{0.948}P_{0.052}$ and barrier material $In_{0.804}Ga_{0.196}As_{0.410}P_{0.590}$.

Most optical fibers do not hold polarization state of light. When arriving in the SOA optical signal can therefore be in any combination of TE and TM polarizations. For this reason components for optical networks must be polarization independent. Polarization independence can be inherent to the amplifier chip or be implemented in the chip packaging. It is in any case an important feature to consider when designing a line amplifier.

2.1.1.3 Starting point of quantum wells design

Best performances for wideband SOAs were obtained by Morito et al. with 5 nm InGaAsP MQW [4]. They obtained a 120 nm bandwidth between 1450 nm and 1570 nm with maximum gain of 18 dB at 1500 nm. The SOA also had high saturation output power of 20 dBm and a 4.5 chip NF was claimed. Active layer was composed of thin MQW with largely separated energy levels. Without information on the exact composition of wells and barriers, we simulated different structures with gaps around 1550 nm and 0.8% compression for the wells. Simulation shows that in such structures only one electron energy level can exist whereas several hole levels coexist as presented in Figure 2.2. All transitions start therefore from the same electron level but toward distinct hole levels. In these conditions separation between HH and LH levels could only be compensated with high tensile strain. These structures are therefore hardly polarization insensitive.

Simulation indicates that first hole level is hh1 as shown in Figure 2.2. Main transition $e1 \rightarrow hh1$ is placed at 1586 nm in the simulation which is slightly higher than what we may read from published gain spectrum. This $e1 \rightarrow hh1$ transition corresponds to TE polarization. Next energy levels are hh2, lh1 and hh3 and transitions towards these levels are simulated at 1470 nm, 1415 nm and 1324 nm respectively. Among these wavelengths only the first is located within the bandwidth presented in the article, the two others being further away. Transition $e1 \rightarrow hh2$ is normally forbidden by selection rules which can be broken at high current injection but will never provide the 18 dB gain presented in the article. It is more likely that this structure makes use of the staircase like density of state in QW SOAs to extend its optical bandwidth. Energy levels being well separated, flat density of states in-between allows to populate higher energy states without reabsorbing high energy photons, thus resulting in a wide gain bandwidth. On the other hand high current density must be reached to obtain the wide gain bandwidth: 17 kA/cm^2 for the studied 5 nm MQW. SOA with such high operating current is hardly implementable in optical networks which may be the limitation of this approach.

This analysis brings a thought on the design of the SOA MQW. Desired solution must indeed give wide optical gain bandwidth at reasonable current density, have a relatively straightforward epitaxial growth and ideally keep polarization independence. Starting from these requirements we elaborated a new structure.

2.1.1.4 First structure

Chosen approach consists in using transitions between fundamental ($n = 1$) and excited states ($n \geq 2$) of both electrons and holes in the quantum wells. Using this technique, Miller et al. have shown a gain material with about 100 nm bandwidth with 1% tensile-strain quantum wells [93]. In this study, due to the high value of tensile strain, light emission is due to the transition between electrons and light hole states, and is strongly TM polarized. However, this solution can be extended to less strained quantum wells, in which first heavy and light hole state levels have almost the same energy value [94]. Then, similarly to bulk materials in which hole states are degenerated, TE=TM condition can be carried out and in the meantime, bandwidth enlargement becomes possible thanks to quantization effects.

Suitable quantum well for TE=TM emission must provide similar lh1 and hh1 energies in $k = 0$. Chosen quantum well first consisted of a $\text{In}_{0.53}\text{Ga}_{0.47}\text{As}_{0.96}\text{P}_{0.04}$ layer tensile strained on InP substrate, with a lattice mismatch of -0.15%. Barrier material consisted of quaternary alloy Q1.17 named after its bulk emission wavelength at 1.17 μm which is almost lattice matched on InP (0.05% compressive strain). Composition and thickness of the wells were adjusted to best fit specifications. Emission wavelength was designed to be around 1550 nm in the C-band.

Two confined electron levels were needed to obtain two distinct electronic transitions. To do so thick QWs were used and their thickness was tuned to precisely control splitting between both electron levels. Barrier bandgap was chosen high enough for efficient confinement of both holes and electrons in the wells. Finally heavy/light hole levels splitting was controlled thanks to reasonable strain values in quantum wells. Strain in well layers is even slightly compensated by opposed strain in barriers bringing total strain value close to zero.

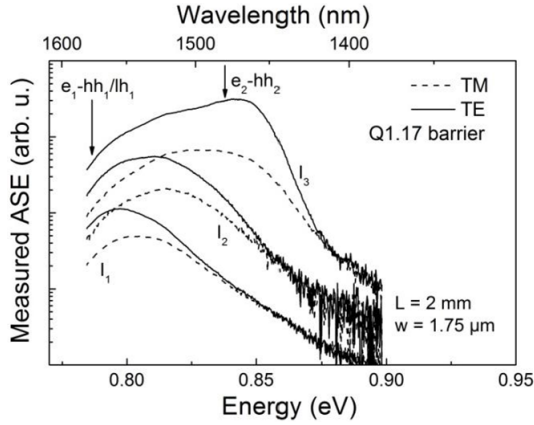


Figure 2.3 – Measured ASE power of $In_{0.53}Ga_{0.47}As_{0.96}P_{0.04}$ MQW SOA for $I_1 = 50$ mA, $I_2 = 100$ mA and $I_3 = 200$ mA after Carrère et al. [83].

Based on this band structure engineering, SOAs have been fabricated and characterized. TE (solid line) and TM (dashed line) amplified spontaneous emission as a function of energy are reported in Figure 2.3 for different injection currents. Due to the low energy splitting between first level $hh1$ and second level $lh1$ ($\Delta E = 5$ meV), $e1 \rightarrow hh1$ and $e1 \rightarrow lh1$ transitions cannot be distinguished experimentally at operating temperature and are presented as one transition on the graph, along with second main transition $e2 \rightarrow hh2$. Calculated energy splittings between $e2 \rightarrow hh2$ and $e1 \rightarrow hh1$ or $e1 \rightarrow lh1$ are 64 meV and 59 meV respectively. These values are in good agreement with the experimentally measured splitting, which is about 55 meV. An increase of the injection current results in a significant increase of ASE bandwidth, signature of the population of second energy level. A maximum measured ASE bandwidth value of 98 nm was obtained with this structure for an injected current of 200 mA.

This solution presents the advantage to allow control of the bandwidth tilt. Indeed at low injection current maximum gain is obtained at long wavelengths but this tilt changes at higher injection current as second transition acquires more gain. This is illustrated in Figure 2.4. Injection current giving the flattest optical bandwidth is called flat gain current I_m . This property to adjust gain spectrum tilt is critical

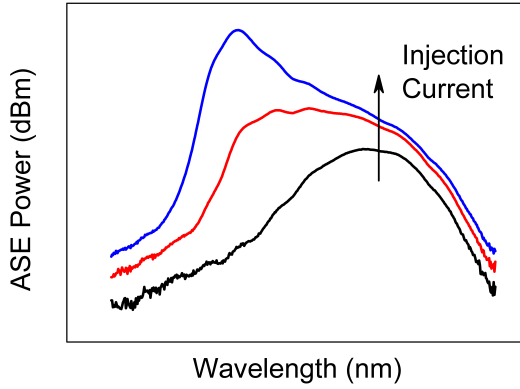


Figure 2.4 – Evolution of the ASE spectrum tilt with injection current. At low injection current (black curve) gain is maximal at longer wavelengths. Largest bandwidth is obtained at I_m (red curve). At higher current (blue curve) spectrum tilt is inverted as gain becomes maximal at shorter wavelengths.

for use in DWDM long-haul transmissions in extended S+C+L band as optical signal in such large bandwidth is subject to stimulated Raman scattering. Raman scattering in optical fibers amplifies photons at wavelengths typically 90 nm higher than signal for an optical signal at 1550 nm. Transmission channels at higher wavelengths therefore benefit from amplification by shorter wavelengths channels. Over long distances channels power distribution thus becomes tilted with maximum at longer wavelengths. Having an amplifier gain spectrum tilted in the opposite direction allows equalization of the channels power distribution at each span. This is highly desirable to obtain a flat channel power distribution at the end of the transmission line.

2.1.1.5 Proposed structure

First results with tensile strained QWs were promising and proved feasibility of the two transitions approach. However to match our specifications we needed to design a structure that could display both large optical bandwidth in C+L band and high saturation power. To do so we decided to implement a so-called asymmetric cladding in order to improve saturation output power. This technique will be detailed in the next section. It involves growing extra layers beneath the active region with slightly higher refractive index. Unfortunately this additional growth increases Γ_{TE}/Γ_{TM} optical confinement ratio when it is necessary to maintain this ratio below 2 and as close to one as possible to keep polarization independence.

In the chosen configuration compensating for $\Gamma_{TE} > \Gamma_{TM}$ would mean increasing tensile strain at much higher values to maintain $\Gamma_{TE}g_{mTE} \approx \Gamma_{TM}g_{mTM}$ by increasing g_{mTM} to compensate for the low Γ_{TM} value. This is detrimental to the structure as it degrades material quality and can even induce dislocations. Having such different confinement factors for TE and TM polarization also means different optical modes and is accompanied by dissimilar propagation losses. These differences impact both noise figure and saturation output power of the SOA and further separate TE from TM amplification.

All these reasons make simultaneous implementation of polarization independent MQW and asymmetric cladding difficult and a choice had to be made regarding our structures. It was decided to privilege high saturation power over polarization independence at the chip level and to develop a polarization diversity scheme in the SOA packaging for use in optical networks. Thus polarization independence is obtained, not at the chip level but for packaged SOAs.

Once the decision was made, it was even decided to accentuate TE amplification to obtain maximal efficiency at this chosen polarization. To do so tensile strain in the MQW was replaced by compressive strain to favor HH levels. It was also decided to move first transition at lower energy by QW design to shift optical bandwidth towards L-band and obtain a centered S+C+L band SOA. Subsection 2.1.2 presents structures resulting from these developments and packaging approach for polarization independence.

2.1.2 Presentation of structures

During the PhD five wideband SOA structures were designed and fabricated together with the same process. Resulting wafers therefore share identical fabrication conditions and different performances should on average only arise from design. In this section we will discuss predicted characteristics of these five structures in terms of bandwidth and gain.

Based on previous experiences of wideband structures in projects Arome and Ultrawide a structure matching specifications for FUI project Calipso was designed. Specifications focused on a TE SOA with optical bandwidth of 120 nm providing gain in an extended S+C+L band between 1490 nm and 1610 nm. Specifications concerning gain value, noise figure and saturation output power will be detailed in the following section.

To position the SOA gain bandwidth we define the quantum well first transition at the bandwidth upper limit around 1620 nm. Both well and barrier materials are chosen to obtain desired transition energy. Photoluminescence (PL) measurements

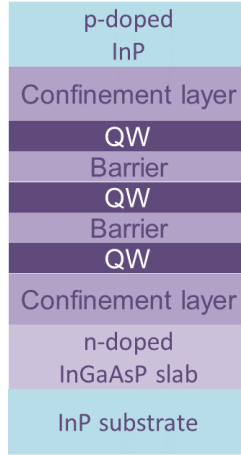


Figure 2.5 – Representation of stacking for a 3 QWs structure.

are chosen for experimental validation of the materials as wavelength of photoluminescence peak corresponds to first transition energy. PL measurements also serve as specification language between design and epitaxy. We have seen in the previous section how composition, thickness and strain for wells and barrier are chosen in order to obtain 120 nm wide gain bandwidth. In our first structure called structure A, quantum well materials are adapted to match requested bandwidth location.

Four variations of this structure were also designed to mitigate fabrication uncertainties. For clarity of the variations explanations a schematic representation of a 3 QWs structure layers stacking is presented in Figure 2.5. First variation is very close to structure A as it keeps identical quantum wells, we called it structure A bis. Only difference is thicker confinement layers to increase optical confinement and hence optical gain. Indeed we have seen in section 1.1 gain dependence on optical confinement with Equation 1.1. Structure A bis was meant as a back up for structure A in case of insufficient optical gain.

Second variation, named B, was a change in requested PL wavelength from 1620 nm to 1640 nm to further cover the upper end of L-band. Simulations showed that a slight change in well material composition was necessary to modify first transition energy. The operation also modifies second transition energy by about the same amount.

Last two structures were meant to increase energy difference between successive energy levels and weaken second well transition $e_2 \rightarrow hh_2$. In the past, some structures have presented a second transition involving a too efficiently confined

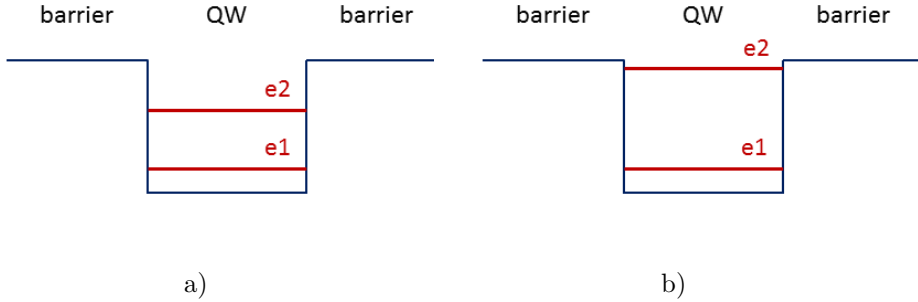


Figure 2.6 – Upper part of a quantum well with a) both electron energy levels confined b) energy level e2 close to barrier CB.

second electron level. In these structures second transition starts operating stimulated emission at relatively low carrier density giving flat gain but of low value. If the second electron energy level is pushed closer to CB barrier level as shown in Figure 2.6, thermal activation of carriers will be enough for some carriers to leak in the barrier and will delay stimulated emission. Higher carrier density will thus be necessary to obtain optical gain from second transition, letting first transition achieve higher gain at flat bandwidth. To this end structure C was designed with smaller gap barrier material. On the other hand, structure D was designed with slightly thinner wells. It splits electronic levels further apart which strengthens first transition and also increases gain bandwidth.

Material composition of wells and barriers for each structure was determined by keeping levels of elements III constant for all layers and varying only elements V. It corresponds to the actual molecular beam epitaxy (MBE) growth process where elements III are kept constant between well and barrier layers for better stability of the sources temperature. To design each structure we start from structure A and adjust only necessary parameters to reach the other desired structures.

Having explained the physical principle behind our broadband SOAs and how we designed five wideband structures, let us now present another critical aspect of SOAs material structure design: improvement of saturation output power with an asymmetric cladding and adapted technological process.

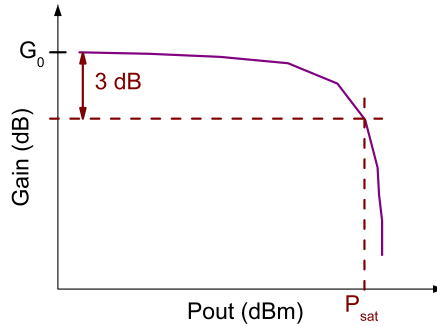


Figure 2.7 – Typical variation of SOA gain with output power at fixed injection current and temperature.

2.2 High power semiconductor optical amplifier

2.2.1 Saturation output Power

2.2.1.1 Definition and stakes

We have seen the definition of saturation output power in section 1.1. Figure 2.7 presents typical variation of gain with output power in a SOA. At constant current density and temperature, gain is constant at low values of P_{out} . As the input power increases so does the output power, following $P_{out} = GP_{in}$. At first gain is unaffected by variations of the input power and the regime is linear. But after a certain point gain starts decreasing as carrier density becomes insufficient to cope with high photon density. Saturated regime is reached when gain loses half of its value. Value of the output power at this point is called saturation output power and is used as indicator of SOA performances.

Being in saturated regime can be desirable for some applications like self or cross-gain modulation and four wave mixing. But in WDM applications it is necessary to have a high saturation output power to operate in linear regime. Non-linear regime can indeed cause signal distortions and limits maximal gain. In the case of DWDM many low power channels must be amplified resulting in fairly high total optical power received by the amplifier. Similarly a power booster amplifier must amplify an already powerful signal. In both cases input power is high but must not disturb performances of the amplifier. Given our large bandwidth this parameter is especially important to add additional channels to existing systems without saturating the amplifier. For our SOAs a saturation output power of at least 20 dBm is therefore required which allows the equivalent of 100 channels at

0 dBm each. We also want gain of at least 15 dB, and NF < 7 dB.

2.2.1.2 How to improve P_{sat} ?

Equation 1.9 derived in Appendix B is recalled here:

$$P_{sat} = \ln(2) \frac{A}{\Gamma} \frac{h\nu}{a_1\tau} \frac{G_0}{G_0 - 2}$$

This equation is obtained with the strong hypothesis that losses are negligible ($\alpha = 0$) which is not the case in real structures. We also neglect ASE power as $P_{ASE} \ll P_{sat}$. This equation however provides guidelines to improve saturation output power of a SOA by showing the influence of diverse parameters. For high gain values we consider $\frac{G_0}{(G_0-2)} \approx 1$ and we obtain the following proportionality relation:

$$P_{sat} \propto \frac{A}{\Gamma} \frac{h\nu}{a_1\tau} \quad (2.8)$$

First term of this equation A/Γ is the optical mode cross section and refers to the waveguide geometry with $A = w \times d$ cross-section surface of the active region and Γ confinement in this region. For high P_{sat} an option is to play on these parameters by increasing the size of the active zone or reducing Γ . However even if A and Γ are easily modifiable, consequences of these changes go beyond P_{sat} . Modifying A implies a direct change of the waveguide geometry with repercussions on optical mode propagation. If the waveguide becomes too wide it will for instance no longer be single mode. Similarly decreasing Γ directly lowers optical gain which must remain above 15 dB to meet our specifications.

Augmentation of the active zone section A is usually obtained by increasing the waveguide width w . It can be done for the entire waveguide but P_{sat} ultimately depends on the width at the SOA output. Structures with tapers like the one presented in Figure 2.8 can be developed to increase w at the end of the SOA [95]. Limiting enlargement of the waveguide to its end avoids having to increase injection current to reach the same carrier density as in narrower structures. Drawback of this kind of waveguide is alteration of the optical mode geometry at the output which can increase coupling losses.

Other option to increase P_{sat} consists of decreasing differential gain a_1 or shortening carrier lifetime τ . This was for instance the goal in Morito SOA [4] by enhancing recombination process and saturating material gain in the thin QWs at high carrier density. Nevertheless this approach is more demanding as it involves modifying the active material of the amplifier. Different variables in the equation also depend



Figure 2.8 – Waveguide with large taper at the output facet.

from each other. For instance a higher confinement factor tends to lower carrier lifetime which should increase P_{sat} . But this effect is not visible as higher Γ directly lowers P_{sat} .

In the case of a broadband SOA, dependence of saturation output power on wavelength must also be taken into account. Indeed through differential gain a_1 , P_{sat} varies throughout the bandwidth and is intrinsically higher at long wavelengths [96]. If our target of $P_{sat} > 20 \text{ dBm}$ is met at 1500 nm it should thus also be the case at higher wavelengths.

2.2.2 Asymmetric cladding

2.2.2.1 Presentation

In the 2000s asymmetric structures with higher refractive index in the n-doped layers started to appear. First developed for lasers, the aim of such structures was to decrease overlap of the optical mode with lossy p-doped layers to reduce propagation losses [97]. Losses are higher in p-doped layers as they mainly originate from intervalence band absorption (IVBA) which depends on hole density. Soon these structures, called asymmetric cladding, were applied to SOAs in the C-band and demonstrated enhanced P_{sat} [7]. By attracting the optical mode toward the n-doped layers it is not only confinement in the p-doped layers Γ_p but also in the active material Γ_{QW} which is reduced thus improving P_{sat} .

Reducing Γ_{QW} also reduces optical gain. The decrease of α through Γ_p slightly counterbalances this effect, but to really compensate for Γ_{QW} reduction in the gain formula, the SOA must be made longer. Decrease of Γ_p is also beneficial to NF through the inversion factor n_{sp} .

For an even greater effect, asymmetric cladding can be associated with enlargement

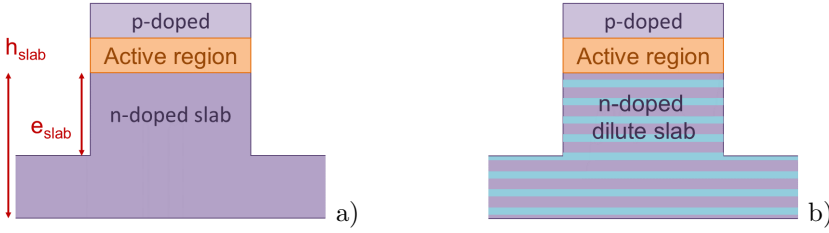


Figure 2.9 – Two different kinds of asymmetric cladding a) bulk slab b) dilute slab.

of the waveguide. Large widths can be used while staying single mode thanks to an effect observed by Marcatilli which allows a multimode waveguide to operate single mode when coupled to a slab [98]. Using this principle large dimensions SOAs with so called slab-coupled optical waveguides (SCOWs), have been developed and show excellent performances [9]. At 1540 nm a 10 mm long SOA with $\Gamma \approx 0.5\%$ and width of $5.4 \mu\text{m}$ has showed P_{sat} of 29 dBm, gain of 13.8 dB and NF of 5.5 dB. These performances were obtained for a high injection current of 5 A and at $T = 16^\circ \text{C}$ [8]. Given big dimensions of the SOA injection current must be high to provide sufficient carrier density. Nevertheless these performances are impressive all the more as the amplifier bandwidth almost reaches 100 nm. As previously discussed P_{sat} and NF performances vary alongside the optical bandwidth.

Another advantage of the asymmetric cladding is the fact that it is integrated in the waveguide outside of the active zone and does not disturb its properties. In our case it should for instance not affect our wide band MQW design. This compatibility with our structure and good results presented by other groups have led to the decision to integrate an asymmetric cladding in our structure for wideband high power SOAs.

2.2.2.2 Dilute and bulk slabs

I was in charge of conducting a campaign of optical simulations to integrate an asymmetric cladding to our five structures. Simulations were conducted on design A and then verified on the other designs. The aim was to obtain a single mode structure with $\Gamma \approx 5\%$ for a width of $5 \mu\text{m}$ by varying layers beneath the active region. First decision to make was the nature of the slab layers. In previous work two approaches had been tried, a bulk slab and a dilute slab composed of a alternated stack of InGaAsP alloy and InP. Both kinds of structure are shown in Figure 2.9. Dilute slab presents the advantage to be tuned more easily for the desirable refractive index by changing layer thicknesses. For a chosen couple

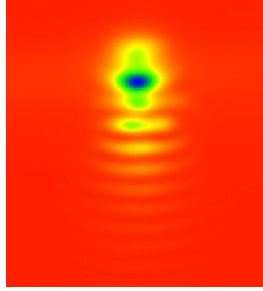


Figure 2.10 – Near field measurement of a SOA with dilute slab made at III-V Lab.

of materials, thickness and number of layers can be varied which allows to finely adjust mean refractive index n_r . It is also possible to vary it along the slab. For a bulk slab n_r is defined by the choice of material. In both cases material must be compatible with an epitaxial growth on InP. This is especially critical for the bulk slab as a thick slab can be subject to dislocation when it presents an even small lattice mismatch with the substrate. Materials must therefore be chosen carefully. Strain is a bit less critical for the dilute slab growth as the alternated InP layers periodically reset strain to zero. It should also be noted that epitaxial growth of this kind of structure takes time and that stability of the MBE reactor is therefore critical.

Some of the past structures with a dilute slab had shown troubled optical mode like the one presented in Figure 2.10. These odd stripes were never observed on bulk slab structures. Moreover in my simulations for this kind of structures I observed the alternated layers thickness to be critical. Indeed to obtain a high average index of refraction, we chose an alternation of n-doped InP and InGaAsP alloy with higher n_r . In simulation these high n_r layers tend to attract the optical mode and if made thick enough they induce a split of the optical mode in two separated lobes. A design was created but because of the increased risk presented by a dilute slab the effort was rationalized toward bulk slab structures and only the latter was made.

2.2.2.3 Optical simulations

Simulations are done with software Fimmwave, edited by Photon Design. The software calculates possible optical modes in a waveguide section defined by user. The section is defined both vertically as a stack of layers with different refractive indexes and laterally by the possibility to place several stacks of different composition and width side by side and etch them when needed. Each material is defined by

Layer	n_r
Quantum well	3.55
Barrier	3.332
p-doped InP	3.165
n-doped InP	3.160

Table 2.2 – Refractive indexes used in optical simulations.

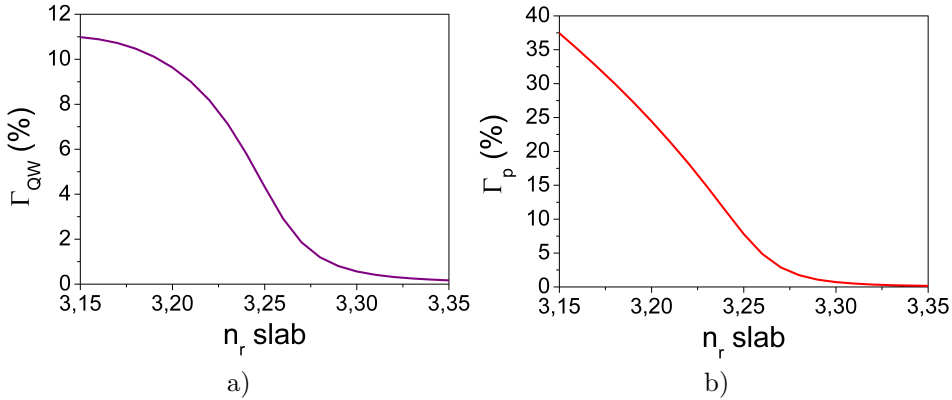


Figure 2.11 – Variation of the confinement factor with refractive index of bulk slab a) in the quantum wells b) in the p-doped InP layers.

its refractive index. First difficulty is therefore the accurate choice of n_r for each layer. We based our simulations on refractive indexes in use at III-V Lab for similar structures and listed in Table 2.2. These indexes are based on Broberg model [99]. By doing so we could more easily compare our results with previous work even in the probable case of inexact absolute values.

Different bulk slab structures were simulated to develop a satisfying asymmetric cladding. Three parameters were tested: refractive index (through material composition) of the slab, thickness of bulk layer $h_{b,slab}$ and etching depth in the slab e_{slab} . Fabrication process is detailed in the next sub-section and presents etching of the waveguide. Simulation output parameters were confinement in the MQW and p-doped layers, divergence of the main optical mode and existence of additional modes. We also wanted a robust structure that could withstand variations due to experimental uncertainties.

To obtain a sufficiently high refractive index we chose to use a InGaAsP alloy which could be grown as a thick layer on InP. Simulations were done to choose a material whose refractive index would give a satisfying value of optical confinement

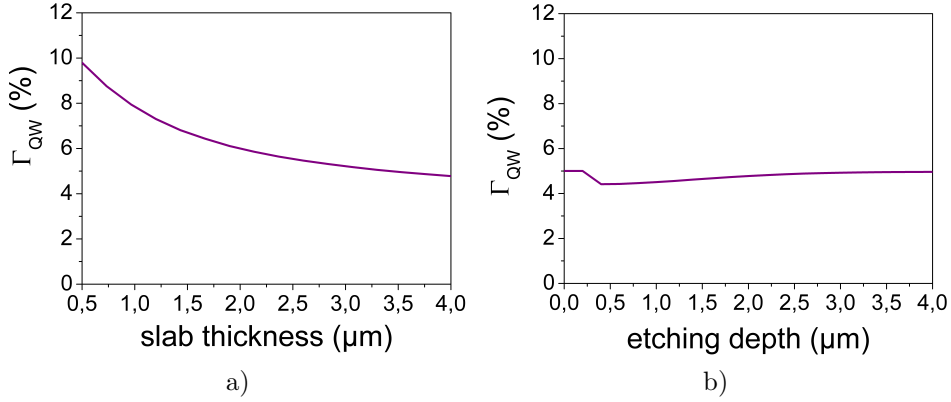


Figure 2.12 – Variation of the confinement factor in the quantum wells with a) slab thickness b) etching depth.

in the MQW. Figure 2.11 shows variations of Γ with n_r of the bulk slab both in the active region and in p-doped InP. Confinement logically decreases as n_r increases and attracts the optical mode. To obtain $\Gamma_{QW} \approx 5\%$ we chose a material with refractive index close to 3.25. Corresponding confinement in p-doped InP is around 8 %.

With this material similar simulations were conducted to determine the slab thickness and etching depth. Figure 2.12 presents simulations of optical confinement in the quantum wells as a function of the slab thickness and etching depth of the slab. Having a thicker slab helps attracting the optical mode which is normally centered around the active region whose refractive index is much higher. A thickness of 4 μm is necessary to reach $\Gamma = 5\%$. Etching depth of the waveguide does not modify much optical confinement. But its impact is decisive for the single-mode character of the waveguide and optical mode geometry. If the etching depth is too small the mode cannot be confined in the MQW and is diffused in the slab. But if the etching is too deep the effect of the slab is also affected. An etching depth of about 1.5 μm in the slab is chosen to avoid this situation. The waveguide multimode cutoff width is found around 4.5 μm in simulations. However higher order modes are less confined in the active zone and thus less amplified. In practice a 5 μm waveguide still exhibits single-mode operation.

We simulate then total stacking for structures A, A bis, C and D for comparison of their optical modes. Structure B is not simulated as we do not have a modeling tool precise enough to estimate refractive index variation between structures A and B. Plots of the simulated optical modes TE₀ are displayed in Figure 2.13. The different structures present expected characteristics in terms of mode geometry. Due to thicker confinement layers optical mode in structure A bis is more confined

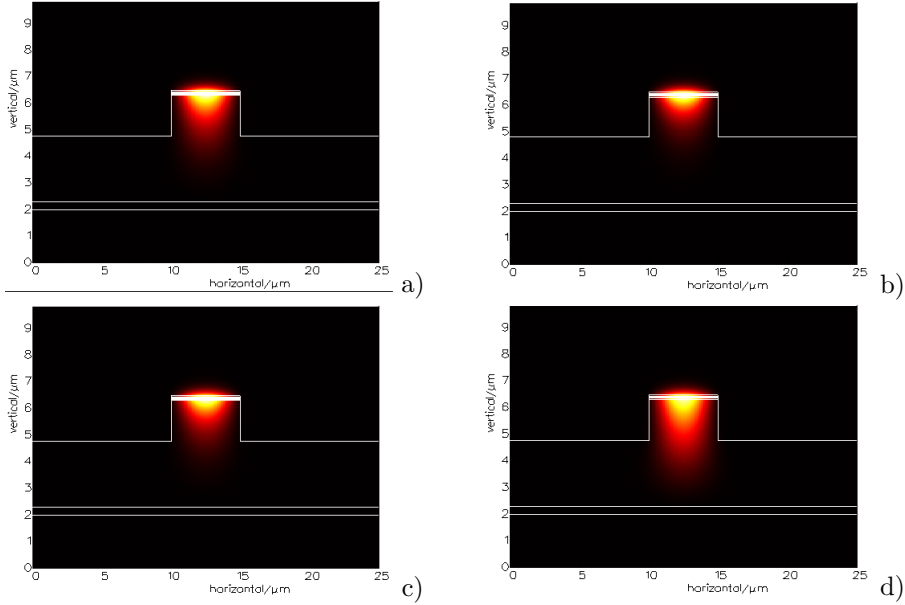


Figure 2.13 – Simulated optical mode TE0 for a) Structure A b) Structure A bis c) Structure C d) Structure D.

in the active zone. Change of barrier material induces a small change in their refractive index which does not affect much mode geometry in structure C. Finally thinner quantum wells modify balance of refractive indexes in structure D and the optical mode is visibly less confined in the active region.

Simulation results for a $5 \mu\text{m}$ waveguide with $4 \mu\text{m}$ thick slab and etching depth of $1.55 \mu\text{m}$ in the slab are presented in Table 2.3 and confirm our analysis on optical confinement. Values of divergence are also given to estimate how well the SOA output signal will couple to following optics. For all structures the optical mode is slightly elliptic but both horizontal and vertical full width at half maximum (FWHM) divergence angles are comprised between 15° and 22° which is a good value for efficient fiber coupling. Thanks to these characteristics no taper is needed to adapt the mode before coupling. Mode effective refractive indexes are close which is not surprising given the modes similarities.

As previously explained a large waveguide can operate single-mode when coupled with a slab layer. Our simulations indicate indeed a multimode waveguide with a TE mode present between slab and active region. Figure 2.14 shows this mode in structure A simulation. This mode has an effective index of 3.238 and is much less confined in the active region with $\Gamma_{QW} = 1.1\%$. We will see in the characterization

Design	$\Gamma_{QW}(\%)$	$\Gamma_P(\%)$	Divergence (FWHM) (°)		Effective index for TE0
			Horizontal	Vertical	
A	4.8	8.8	16.1	19.8	3.247
A bis	6.2	10.6	17	21.8	3.249
C	5.5	10.1	16.5	20.6	3.248
D	3.9	8.1	16.5	19.7	3.246

Table 2.3 – Characteristics of simulated optical TE0 modes.

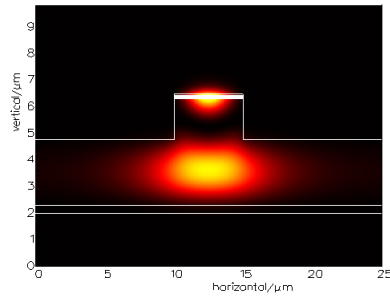


Figure 2.14 – Slab optical mode present in simulations.

section that due to low gain of this slab mode our structures operate nevertheless single-mode.

Asymmetric cladding is incorporated to the SOA original stacking during epitaxial growth. Wafers are then processed to define the SOA waveguides. Fabrication process is as equally important as design and epitaxial growth for the SOA performances. Following subsection describes characteristics of the process and optimization for high power components.

2.2.3 Semi-insulated buried heterostructure

SOA can be fabricated with a relatively simple technological process compared to other devices or PICs. Nevertheless the fabrication process dramatically influences SOA performances on two main aspects. First at the electrical level where the SOA PiN junction under direct polarization can be modeled by a diode and an equivalent series resistance R_s in series. It is desirable to minimize this resistance to reduce power consumption and prevent electrical leakages. Furthermore SOA

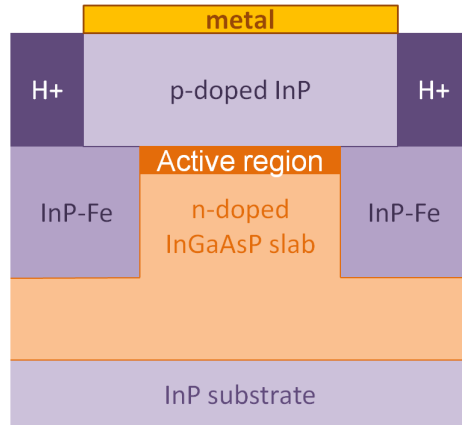


Figure 2.15 – Schematic structure of waveguide processed with SIBH.

performances are particularly sensitive to temperature and higher resistance value also means higher Joule effect and increased SOA self-heating. Maintaining low R_s value is therefore beneficial to temperature management which reduces cooling system power consumption. Second critical aspect of the fabrication process is also linked to thermal management of the SOA and consists of insuring good heat dissipation for efficient thermal regulation.

Chosen process to cope with these requirements is semi-insulating buried heterostructure (SIBH) which consists of burying the waveguide in an insulating material. This structure is shown in Figure 2.15. During a first epitaxial growth the InGaAsP slab and the active region are grown on an InP substrate. Then the waveguide is etched down to $1.5 \mu\text{m}$ in the bulk slab. A second epitaxial growth consists of growing an insulating layer of InP on the sides of the waveguide. Finally a layer of p-doped InP is grown on the wafer. To avoid electrical leakages regions away from the waveguide are bombarded with high energy protons and turn p-doped InP in an insulating layer. This step also improves injection efficiency by preventing current injection on the waveguide sides. Electrical contact on the waveguide is insured by a metal layer deposited on top of the p-doped InP.

InP dissipates heat better than InGaAsP alloys. Burying the waveguide in InP is therefore beneficial for thermal management of the SOA. Surrounding InP is doped with iron to increase its resistivity and thus prevent electrical leakages in the InP. Efficiency of the insulating InP layer is directly linked to the waveguide etching depth. Indeed resistance of the Fe-doped InP increases with its thickness. At high injection current despite the resistivity difference between waveguide and surrounding InP layers fraction of the current might pass through InP causing an

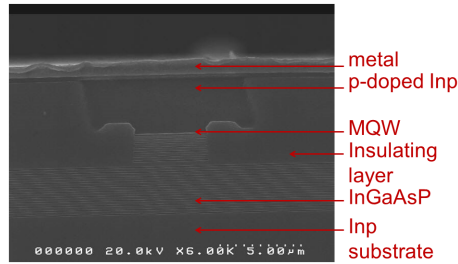


Figure 2.16 – Scanning electron microscopy (MEB) picture of SIBH processed waveguide.

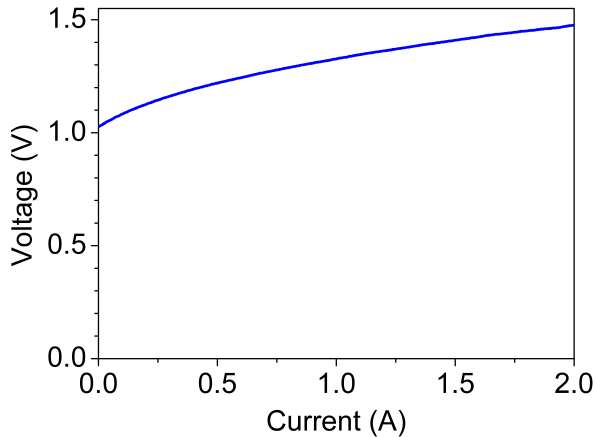


Figure 2.17 – Voltage as a function of injection current.

electrical leakage. A deeper etch can be used to avoid these leakages by increasing resistance of the InP layer. However it must take into account conditions defined by optical simulations to not interfere with the slab properties. With an etching depth of $1.5 \mu\text{m}$ in the slab our structure is well adapted for high injection currents. Figure 2.17 shows measured voltage as a function of injection current in one of our structures. Even at high currents the curve is close to linear meaning that the resistance is almost constant and that little leakage occurs.

Other buried processes can be compared to SIBH, notably shallow ridge which is extensively used for SOAs and buried ridge stripe (BRS) processes. Schematic illustrations of both processes are shown in Figure 2.18. Contrary to SIBH, in shallow ridge technological process, the waveguide is etched above the active layers. While this approach perfectly works for classic SOAs, the addition of the asymmetric cladding makes it unusable for our designs. Not etching the slab strengthens its

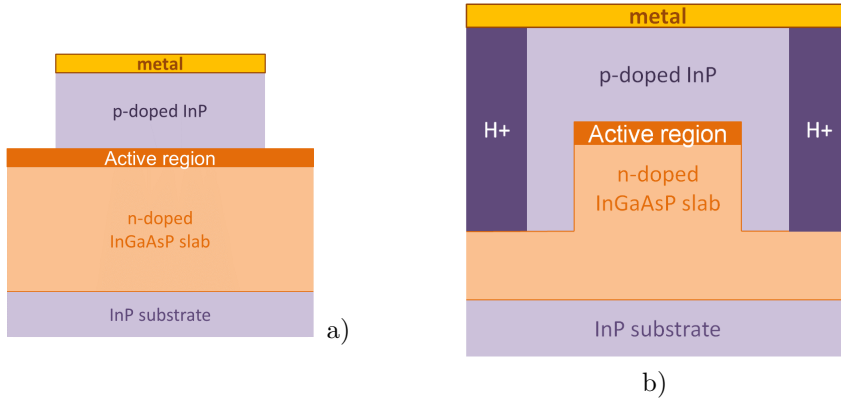


Figure 2.18 – Illustration of different technological processes a) shallow ridge b) BRS.

attraction on the optical mode and main mode is diffused in the slab which prevents efficient guiding of light in the active layers. Air surrounding the waveguide also poorly dissipates heat, making thermal management more difficult. Furthermore, non injected InGaAsP on the waveguide sides may absorb part of the signal.

In the BRS process, the sides of the waveguide are etched below the active zone and buried in another material, providing lateral guiding of light. BRS process consists for its part in burying the waveguide in p-doped InP and insulate it away from the waveguide with high energy protons, comparably to SIBH. While R_s and heat dissipation are good, there is still an increased risk of electrical leakage at high current compared to SIBH.

Conclusion

In this chapter we have presented how material structure of developed SOAs was chosen. Two axis were studied, one to broaden SOA optical bandwidth to 120 nm and another to improve SOA saturation power. In both cases simulations were conducted to test proposed solution and adapt it to our fabrication restrictions and specifications. First we simulated a MQW structure with two electronic transitions to obtain a wideband device. Chosen design amplifies TE-polarization only. Five structures were designed with small variations to test structure stability and be protected against experimental variability. All simulated structures present wide gain bandwidth

Proposed wideband SOAs can not be used in DWDM transmissions without having a high saturation output power. We developed a high power structure compatible with our wideband design by incorporating an asymmetric cladding. This element is composed of a thick InGaAsP layer placed beneath the active region. Its composition, thickness and etching were chosen after optical simulations to obtain the desirable characteristics in terms of optical confinement and mode geometry. Influence of the fabrication process was also taken into account to obtain the best device performances.

Each of the designs was experimentally tested by fabricating a wafer with SIBH process. Next chapter focuses on characterization of obtained SOAs and comparison of their performances.

Characterization

We have detailed all steps of the SOA design and fabrication toward a high power wideband amplifier in the previous chapter. In this chapter we present characterizations of the different SOAs made during the thesis including the five designs detailed in section 2.1. We evaluate the SOA performance in the light of our specifications of a 120 nm optical gain bandwidth, gain > 15 dB, P_{sat} of 20 dBm and NF < 7 dB. We also compare the structures to see the impact of the different designs and evaluate accuracy of simulations.

3.1 From wafer to SOA

A wafer comprises a lot of SOAs which number is determined by the masks design. A production mask will optimize the number of devices on the wafer whereas a research mask like ours presents diverse devices to be tested. At the end of the technological process the wafer is thinned and metal is deposited at the back for electrical contact. To separate individual SOAs the wafer must be cleaved into cells, arrays and finally individual chips. We first cleave arrays of fifteen SOAs of the same length, 4 mm in our case which compensates for small Γ value. To avoid reflection at the facets our waveguides are 7° -tilted. This characteristic must be taken into account when designing the mask to allow cleaving of the devices without sacrificing half of them as can be seen in Figure 3.1.

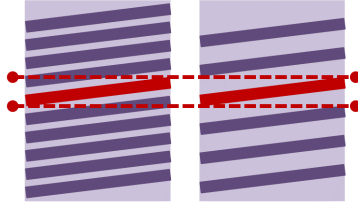


Figure 3.1 – Cleaving of tilted SOAs in non-optimized (left) and optimized (right) masks.

Arrays of SOAs are then anti-reflection coated to obtain 10^{-4} reflectivity at the facets. Anti-reflection coating which consists of thin $\text{SiO}_2/\text{TiO}_2$ layers deposition is done on SOA arrays rather than individual chips for practicability. Electrical and optical characterization can already be done at this stage but thermal management of the chips remains unsatisfying on bare chips. Individual SOAs are therefore cleaved and brazed on specific submounts which allow good temperature management. Each submount comprises a thermal resistance measuring temperature close to the chip. The thermal resistance serves as captor for a Peltier module placed beneath the submount. For all characterizations temperature is regulated at 25°C .

The submount also facilitates electrical injection of the SOA which is wire bonded to an electrode and brazed on another. Both electrodes are accessible to electrical probes which are then connected to a Keithley 2400 current source. Finally as SOAs are 7° -tilted light goes out of the waveguide with a 23° angle following Snell-Descartes law. To avoid having to rotate optical fibers, the SOA is positioned with an 23° angle on the submount so that light goes out perpendicular to the submount edge. This feature greatly facilitates chip positioning thereafter.

3.2 Optical mode

In the previous chapter we simulated the waveguide optical mode for all five structures and calculated corresponding divergence angles. In this section we measure these values for comparison with simulations.

3.2.1 Experimental set-up

A first approximation of the mode geometry can be obtained by using an infrared card which turns infrared light around $1.55\ \mu\text{m}$ into visible red light. This method

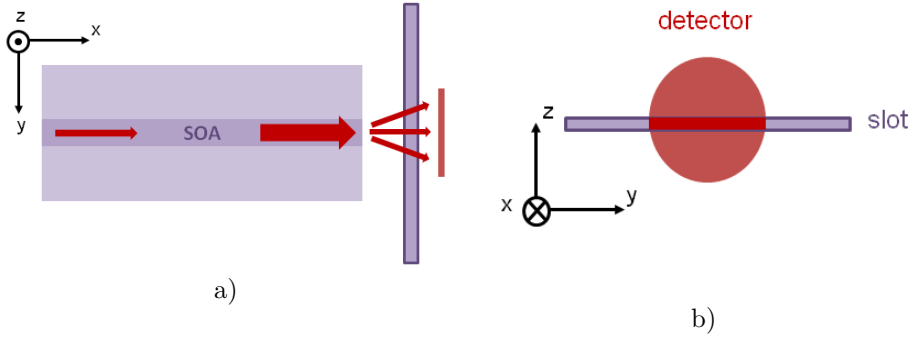


Figure 3.2 – a) Schematic presentation of the farfield measurement set-up viewed from above b) Front view of the detector and slot.

only gives a rough idea of the mode geometry and is used to quickly check if the mode is approximately circular. A more precise method consists in doing a far-field measurement to obtain an image of the optical mode outside the SOA. Measurement set-up consists of an array of photo-diodes which measures light power at a given angle defined by a thin slot placed in front of the detector and in the SOA facet plane. A schematic view of the set-up is shown in Figure 3.2. At the outside facet of the SOA, optical beam starts to diverge from the waveguide mode geometry. Knowing the distance between SOA facet and detector, the latter being centered on the waveguide, power distribution can be related to the divergence angle. For a circular mode this far-field distribution is Gaussian.

3.2.2 Results

Figures 3.3 and 3.4 present experimental curves of the far-field measurements at 0° (horizontal slot) and 90° (vertical slot) for the wafers associated with our five designs. Measurement is done for $5\ \mu\text{m}$ -wide and $2\ \text{mm}$ -long Fabry-Perot waveguides at injection current of $400\ \text{mA}$, above threshold current. Each curve is fitted with a Gaussian model to extract full-width at half maximum divergence angle. Gaussian model fits well all experimental curves and extracted divergence angles are presented in Table 3.1. Angles are comprised between 14° and 19° which is adapted to the optical fibers used for coupling of the device. Small difference between horizontal and vertical divergence angles shows a slightly elliptic mode. All values are in good agreement with optical simulation with a maximum deviation of 2.4° between simulation and measurement and a mean deviation of less than 1.5° .

It is also possible to do a multi-angle measurement from 0° to 360° to obtain a

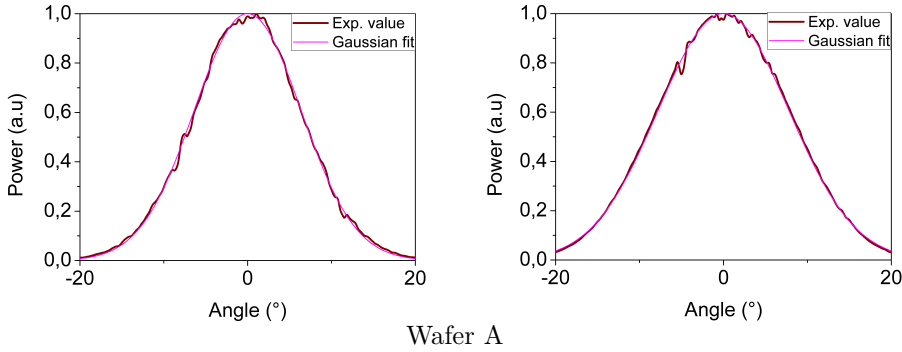


Figure 3.3 – Divergence measurements and Gaussian fits. On the left column horizontal divergence, on the right column vertical divergence.

Design	Divergence (FWHM)			
	Experimental values		Simulated values	
	Horizontal	Vertical	Horizontal	Vertical
A	15.1	18.4	16.1 °	19.8 °
A bis	16.1	19.4	17 °	21.8 °
B	14.1 °	19.1 °	16.1 °	19.8 °
C	14.5 °	19.0 °	16.5 °	20.6 °
D	15.2 °	19.1 °	16.5 °	19.7 °

Table 3.1 – Comparison of simulated and measured divergence angles.

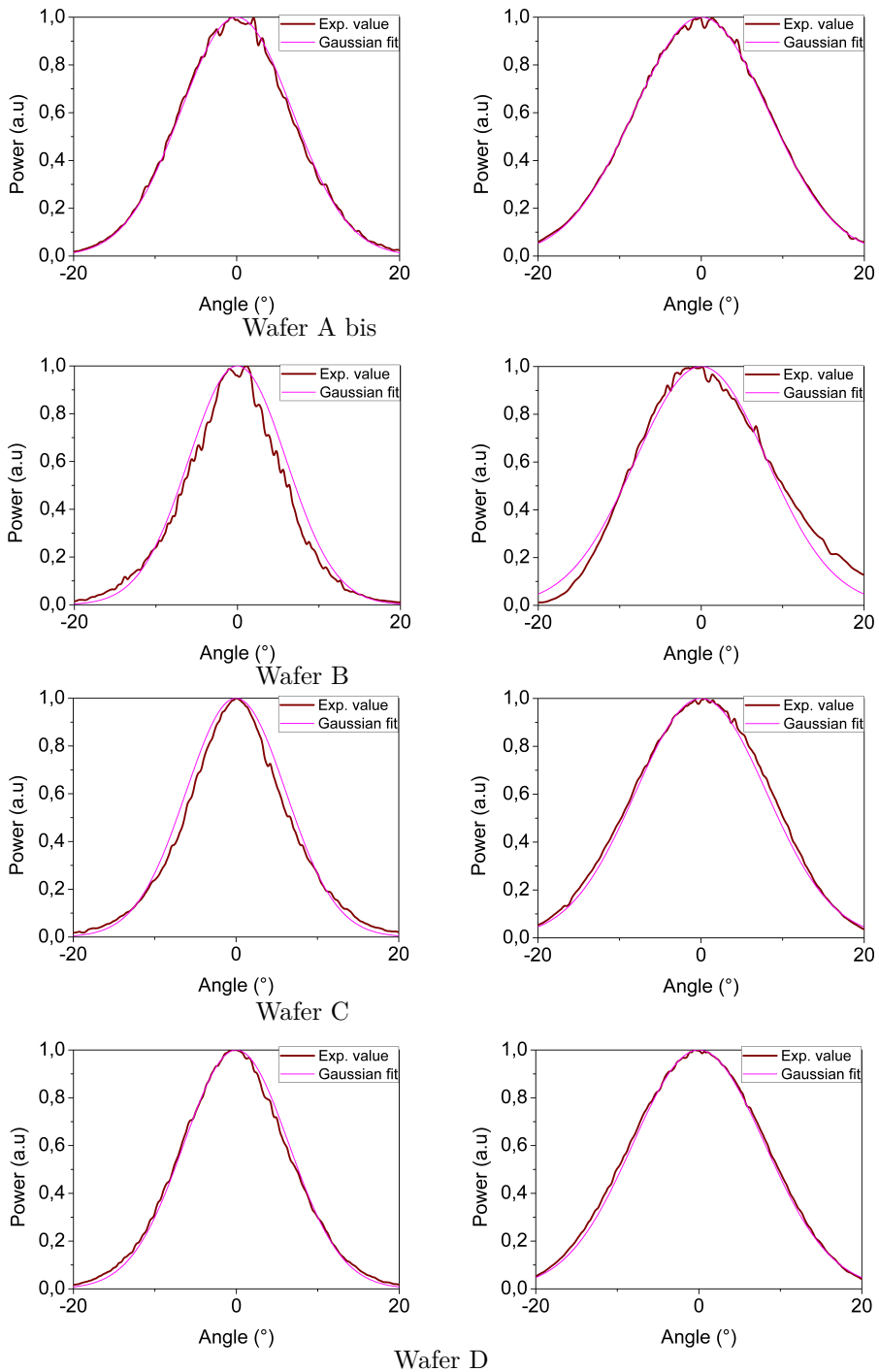


Figure 3.4 – Divergence measurements and Gaussian fits. On the left column horizontal divergence, on the right column vertical divergence.

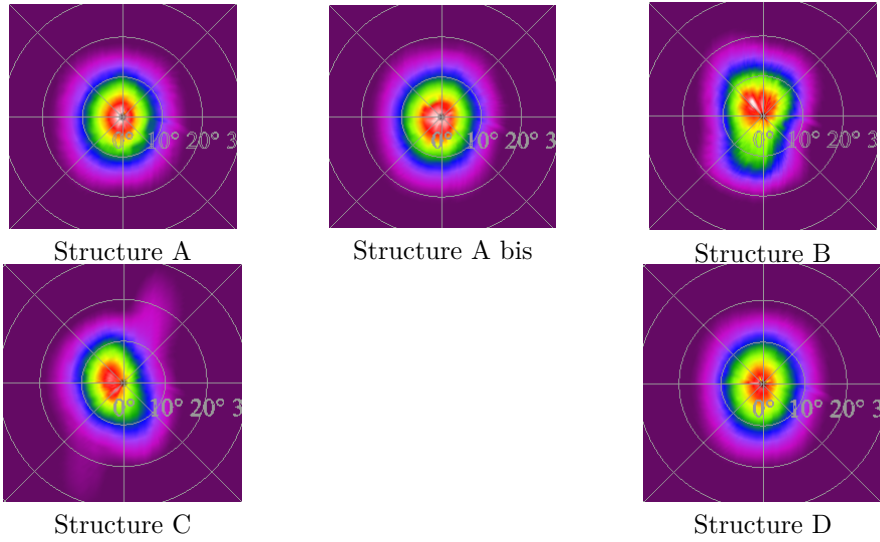


Figure 3.5 – Farfield measurements of $5 \mu\text{m}$ wide waveguides at 400 mA from the five structures.

two-dimensions plot of the optical mode. Plots obtained with a step of 3.6° are displayed in Figure 3.5. In the plots red indicates high optical power and purple low optical power. These pictures confirm the quasi-circular shape of the optical mode for all wafers. This characteristic is important for good optical coupling between SOA and following optics like fibers. We have seen in Section 1.1 how coupling losses affect gain and NF of a SOA. Maintaining low coupling losses is critical to obtain high performances devices and these quasi-circular optical modes are essential to this objective.

In the next two sections we present characterizations of five SOAs originating from the five wafers presented in the previous chapter. For simplicity we name the SOAs after the associated wafers and designs. We have therefore SOAs A, A bis, B, C and D. All measurements referring to one SOA are done on the same chip. All SOAs are 4 mm-long and 5 μm -wide and are measured in the same conditions. Apart from the chips themselves only differences between the measurements are coupling losses which are non exactly reproducible. In these conditions valid comparisons of the SOAs performances can be made.

3.3 Wideband optical bandwidth

3.3.1 ASE spectra

Bandwidth of a SOA can be first assessed by measuring its ASE spectrum. Indeed spontaneous emission occurs at the wavelengths corresponding to the quantum wells transitions. With two different transitions the ASE spectrum of our SOAs is also broaden and both transitions are visible. The ASE spectrum can be quite different from the gain spectrum when the SOA gain is subject to longitudinal spacial hole burning (LSHB). In this case the carrier density varies throughout the waveguide, being maximum in the middle of the SOA and minimum at the SOA facets. This variation in carrier density creates a difference between ASE and gain spectra. For a SOA without LSHB, ASE and gain spectra are similar in shape but are usually shifted current: stimulated emission consumes more carriers than spontaneous emission meaning that more current is needed to obtain the same level filling.

To measure the ASE spectrum the SOA is electrically injected by direct polarization of the PiN diode. Using the ASE power, one facet of the waveguide is coupled to an optical fiber by maximizing collected optical power. Optical fiber is connected to a MS9710B Anritsu optical spectrum analyzer (OSA) which measures and displays optical power for a wide range of wavelengths. For this measurement both facets of the SOA are equivalent as ASE is the same at both ends of a symmetric waveguide. It is thus interesting to compare optical power at both facets to detect eventual defects in the waveguide or at one facet.

Figure 3.6 presents ASE spectrum of SOA A at different injection currents. This spectrum perfectly illustrates the operating principle of our wideband SOA. At first only one transition is visible around 1620 nm and as current increases so does optical power for this first peak. Soon the spectrum starts to broaden as electronic levels fill and second transition starts presenting gain. Around 400 mA

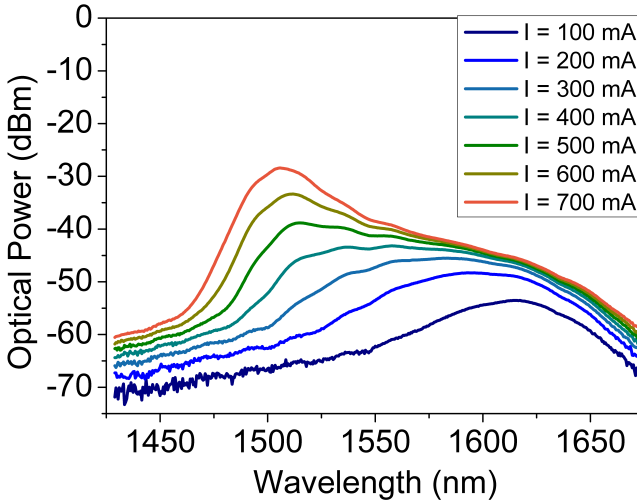


Figure 3.6 – ASE spectrum of SOA A as a function of injection current.

the spectrum is flat and wide. At higher currents carriers fill the second electron level and second transition starts presenting more gain than the first, creating a second peak around 1510 nm. Optical power at the second peak keeps increasing but saturates at 1620 nm.

The ASE spectrum presents the desired characteristics as the two electronic transitions result in wide optical bandwidth. It is however interesting to compare this experimental bandwidth with our previous simulations in terms of position and bandwidth range. Similarly it is interesting to compare ASE spectra of the different designs. Figure 3.7 shows superposition of the ASE spectra at 400 mA with simulated material gain for structure A. Carrier density used in material simulation does not directly translate into current density, it is therefore complicated to compare corresponding curves. However it appears clearly that simulation predicts broader spectra than what is experimentally obtained. Experimental spectra expands from 1510 nm to 1615 nm whereas simulated spectra extends between 1325 nm and 1690 nm. This large difference is due to the fact that theoretical model does not take into account all absorption and recombination phenomena that affect the spectrum width.

Figure 3.8 shows comparison of ASE spectra from the five SOAs. Given their different designs the SOAs ASE spectra can have different optical power levels. However we do not consider coupling losses when measuring an ASE spectrum as they only affect measured power level. For this reason we normalize all spectra at 0 dBm and only compare them in terms of bandwidth. Figure on the left shows

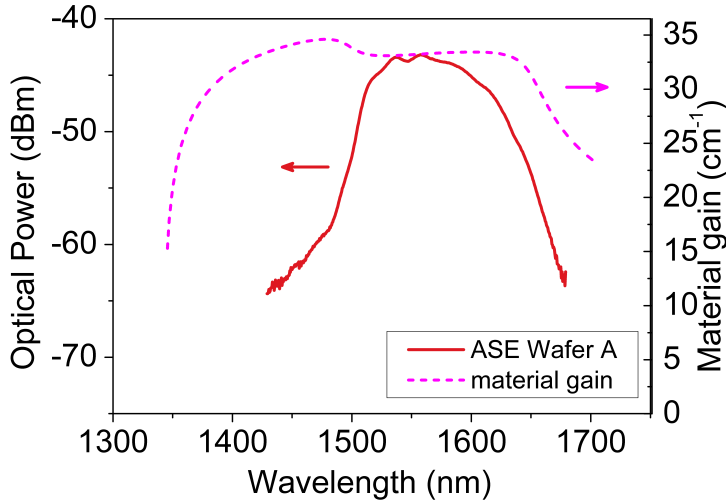


Figure 3.7 – Comparison of ASE spectrum from SOA A and simulated material gain for structure A.

all spectra at 400 mA which is the current giving a flat spectrum for SOA A. Structure A being our reference it is interesting to compare the other wafers with it and we have normalized the wavelength so that their upper limit corresponds to spectrum A. It is first reassuring to note that all spectra are quite similar even if small differences arise. SOA A is logically has a narrower spectrum due to its high confinement. Designs C and D were meant to reach a flat spectrum at higher injected current due to larger splitting between electron energy levels. This is verified in the second figure with flat spectrum current I_m respectively at 400 mA for SOA A, 470 mA for SOA C and 600 mA for SOA D with also a larger bandwidth. This result confirms the stronger effect of QW width reduction on flat gain current compared to a slight change in barrier composition. A more surprising observation is a wavelength shift for SOA D. Second transition was indeed expected at shorter wavelengths from simulations but the entire spectrum is shifted. PL peak of Wafer D was already deviated toward shorter wavelengths in first characterizations but it is unclear if this smaller deviation is enough to explain the spectrum shift. Table 3.2 resumes characteristics of the five SOAs ASE spectra.

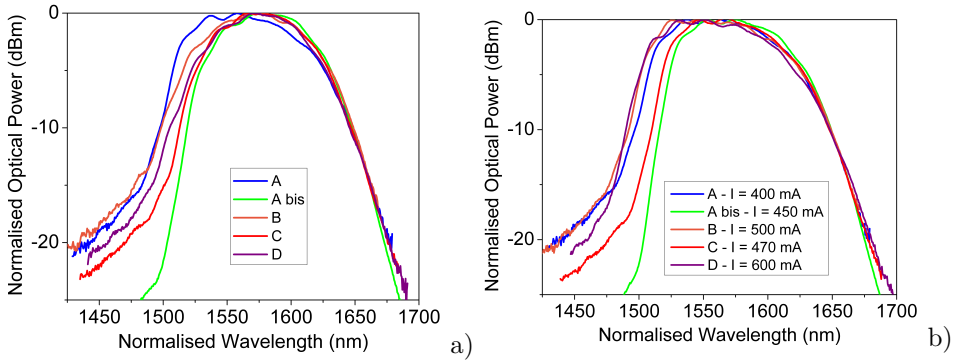


Figure 3.8 – ASE spectra of SOAs A, A bis, B, C and D a) at 400 mA b) at flat ASE current.

Design	Flat ASE current	Bandwidth range	Bandwidth limits
A	400 mA	100 nm	1512 - 1612 nm
A bis	450 mA	88 nm	1512 - 1600 nm
B	mA		
C	470 mA	94 nm	1512 - 1606 nm
D	600 mA	104 nm	1489 - 1593 nm

Table 3.2 – Characteristics of the ASE spectra.

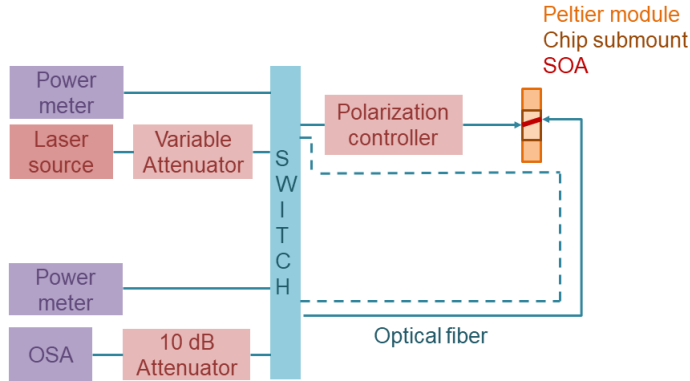


Figure 3.9 – Schematic representation of optical gain measurement set-up.

3.3.2 Experimental set-up for gain measurement

Gain measurement is a bit more complex than ASE spectrum measurement as it necessitates an input optical signal at a given wavelength but main elements remain the same. Optical set-up of the gain measurement is shown in Figure 3.9. It comprises three main blocks: input block, SOA main block and output block linked by an optical switch from LIGHTech Fiberoptics Inc. The switch can link the SOA block to one element or the other in the input and output blocks. For instance during coupling of the SOA to optical fibers, main block is linked to power meters on both sides.

Input block comprises a Ando AQ2140 power meter mainly used for optical coupling and a tunable laser source EXFO FLS-2600B used as input signal for gain measurement. Laser tuning range is between 1510 nm and 1612 nm and has a maximum output power of 0 dBm which limits measurements of our wideband SOAs. In the input block laser is followed by a HA9 variable optical attenuator from JDS Uniphase for control of the input signal power level. After the switch the main block comprises a polarization controller to only inject TE polarization in the SOA and finally the SOA itself. The SOA is brazed on a submount placed on a Peltier module. An ILX LDC-3722B controller manages the Peltier module with temperature information from the thermal resistance placed on the submount. The output optical fiber returns to the switch to reach the output block. It can be linked to a second power meter, an Agilent 8163A also used for optical coupling or to an Anritsu MS9710B OSA. All elements are linked with optical fibers. The switch also allows to short-circuit the main block for direct measurement of injected source in SOA optical power and wavelength. This short-circuit optical fiber is represented by a dash line in Figure 3.9.

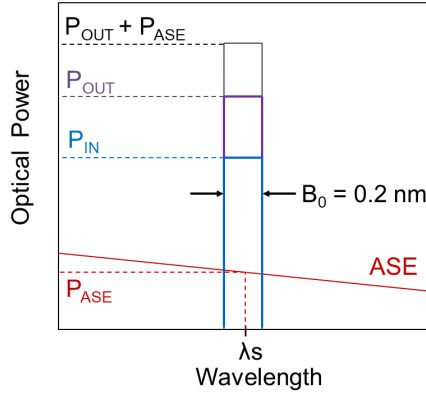


Figure 3.10 – Representation of optical power reading on OSA.

Principle of classical gain measurement can be found in [53]. It consists of measuring ratio of output power over input power. Input power can be measured quite easily right before the SOA but output power is not directly measured due to the impact of ASE power. Figure 3.10 shows how ASE power must be subtracted from read value of optical power to obtain output power. From there gain is calculated using formula $G = 10 \log\left(\frac{P_{out}}{P_{in}}\right)$. We fix $P_{in} = -25$ dBm for all gain measurement to be in linear regime with all SOAs. For characterization purpose we measure coupling losses for each SOA but all presented values are fiber-to-fiber values. Coupling losses for all SOAs are comprised between 1.5 and 2 dB. We measure gain at different laser wavelengths, limited by the laser tuning range. In the last chapter we present a more exhaustive characterization thanks to external collaboration in the frame of FUI project Calipso with measurements from 1500 to 1620 nm.

3.3.3 Optical gain

We present gain measurements for SOAs A, A bis, B, C and D. We start with SOA A by showing gain spectrum for different currents in Figure 3.11 a). Again we observe predicted behavior with increasing current which brings final confirmation of the SOA wideband character. Flattest gain spectrum is found at an injection current of 500 mA. This current is referred to as flat gain current I_m . Figure 3.11 b) shows how gain increases with current for eight wavelengths between 1510 and 1610 nm. Around 500 mA longer wavelengths curves cross with shorter wavelengths curves confirming the value of I_m . We compare in Figure 3.12 obtained gain spectra at 400 mA and 500 mA with flattest ASE spectrum obtained at 400 mA. As stimulated emission consumes more carriers than amplified spontaneous emission, flat gain current is higher than flat ASE current. Nevertheless very good agreement is found

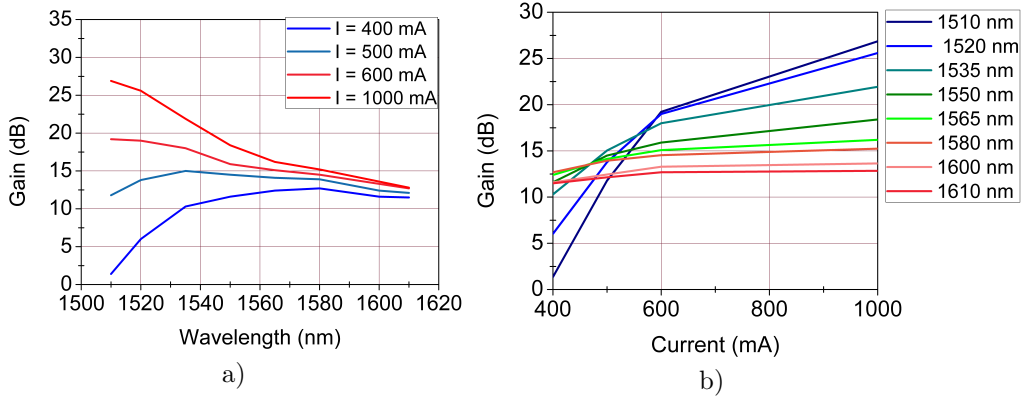


Figure 3.11 – a) Gain spectra of Wafer A SOA b) Gain as a function of current between 1510 and 1610 nm.

between flattest spectra of gain and ASE. At 500 mA maximum gain is 15 dB at 1535 nm and 100 nm measured bandwidth is limited by the laser source tuning range and not by the SOA. We expect thus SOA bandwidth to extend a bit further than 1510 and 1610 nm.

Gain spectra of the other SOAs are presented in Figure 3.13. All spectra present similar shapes with little variations of range and position. For better comparison we plot together in Figure 3.14 all spectra at 500 mA, flat gain current of SOA A. In this plot differences between SOAs appear more clearly. SOA A presents flattest spectrum and other SOAs still have slightly less gain at shorter wavelengths as they are still below flat gain current. It is interesting to note that SOA A presents in fact the lowest gain value of all SOAs. This gain difference does not arise from design and SOA A and B should in theory present same gain. It originates therefore probably from fabrication either epitaxy or technological process and illustrates gain sensitivity to fabrication conditions. In theory SOA A bis present 30% more confinement than SOA A. In practice we measure a gain difference of around 8 dB between both SOAs. A notable difference is also present between SOAs A bis and D while their confinements are similar.

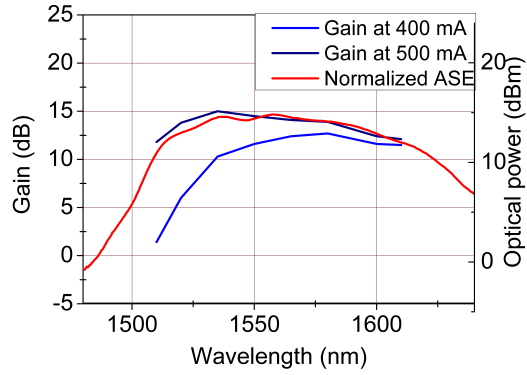


Figure 3.12 – Comparison of ASE and gain spectra in SOA A.

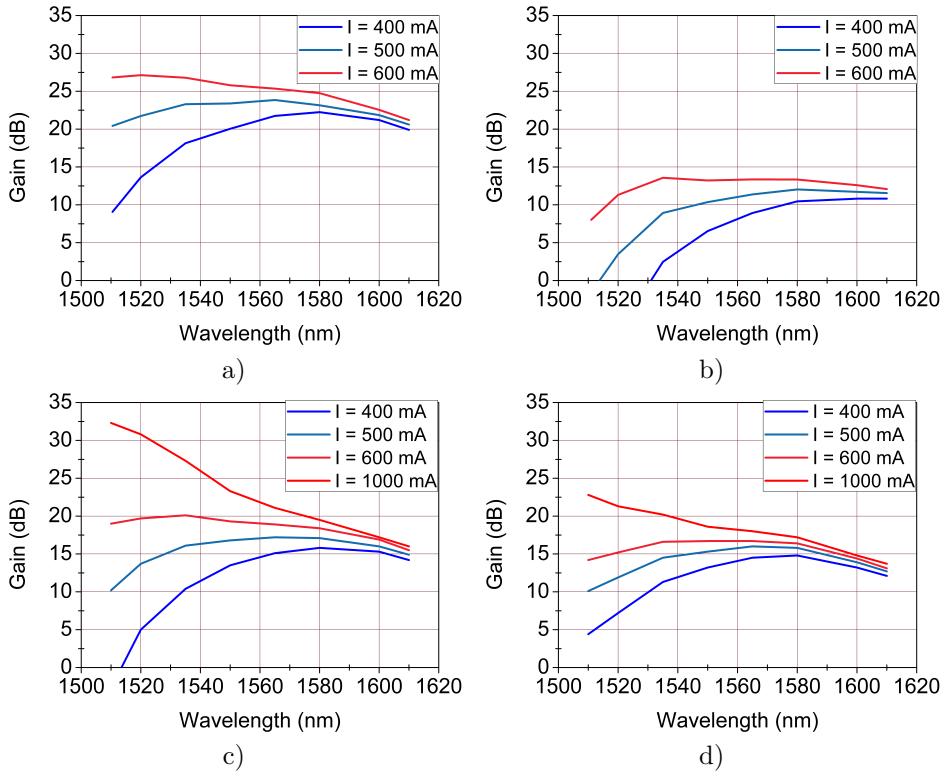


Figure 3.13 – Gain spectra of a) SOA A bis b) SOA B c) SOA C d) SOA D.

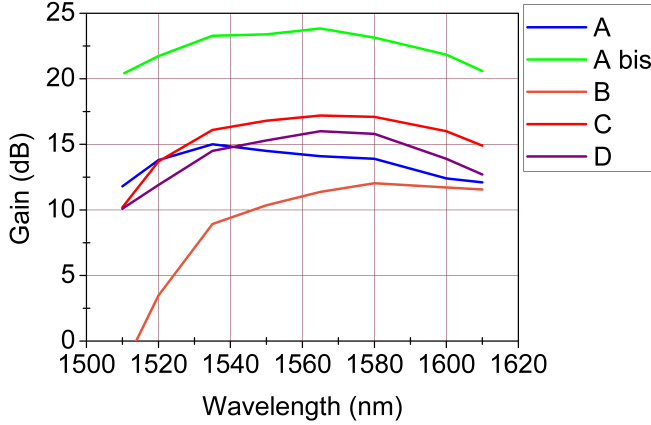


Figure 3.14 – Gain spectra of the five designs SOAs at 500 mA.

3.4 Noise figure and Saturation output power

3.4.1 Noise figure

NF is calculated with equation 1.4: $NF = \frac{2P_{ASE}}{G_{chip}h\nu B_0} + \frac{1}{G_{chip}}$. With a minimum gain value of 12 dB for SOA A we can neglect $\frac{1}{G_{chip}}$ and only consider first term of the equation. When measuring gain we also measure P_{ASE} as explained in previous section. We can therefore easily calculate NF from gain measurement. We must nevertheless be careful to take into account B_0 which corresponds to the OSA filter bandwidth i.e its resolution. We chose for our measurements to work with a 0.2 nm resolution.

Figure 3.15 shows NF variations with wavelengths at different currents for the five SOAs. In all curves longer wavelengths have far better NF than shorter wavelengths. This result originates from the wavelength dependence of inversion factor n_{sp} described in Section 1.1. First energy levels are more populated and have a lower n_{sp} . Similarly n_{sp} decreases when carrier density increases which explains why NF improves at low wavelength for higher currents. For all SOAs NF tends toward a limit close to 4 dB at 1610 nm. For design D it reaches 7 dB at 1510 nm for an injection current of 1 A but for the other SOAs it remains closer to 9 dB. Figure 3.16 shows NF spectra of all five SOAs at 500 mA. At this current SOA D presents best performances and SOA A bis the highest NF.

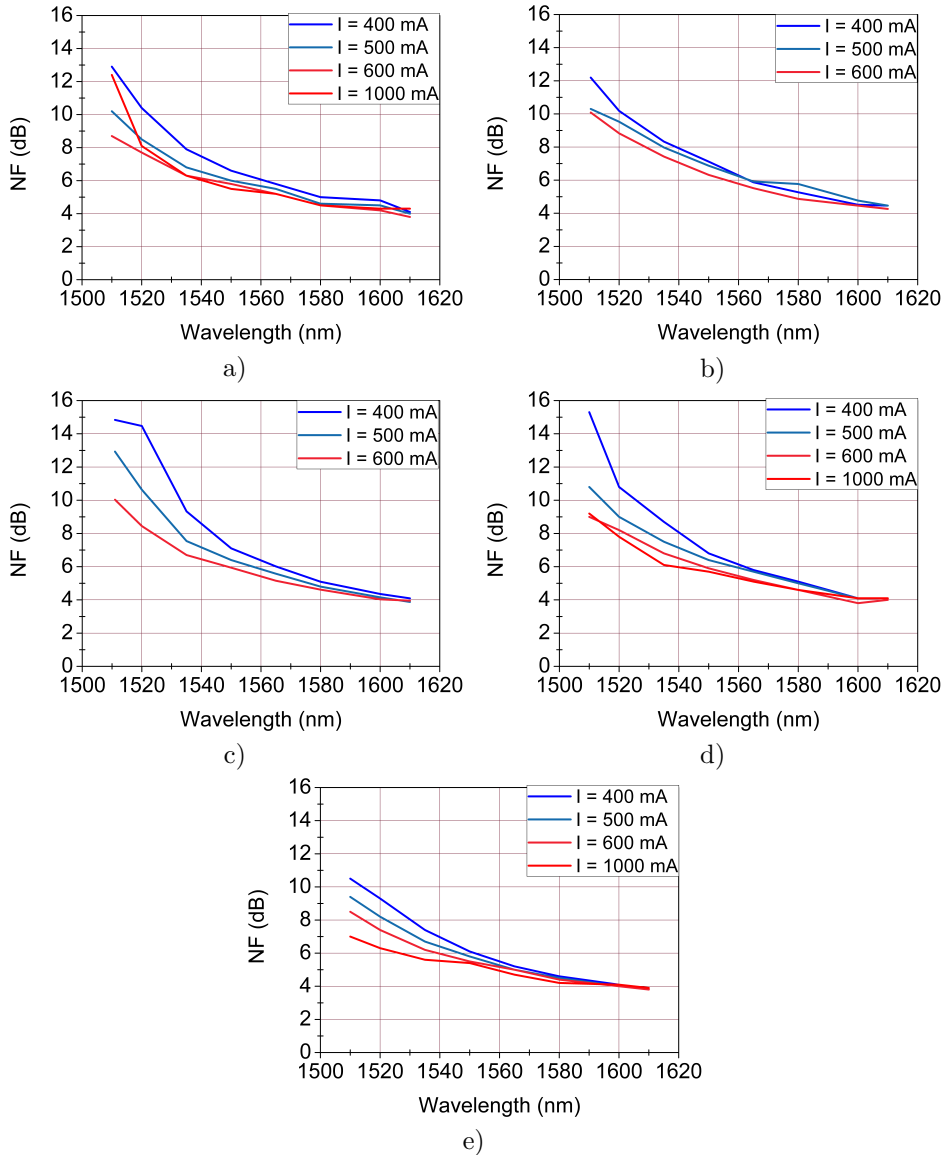


Figure 3.15 – NF spectrum at different injection currents a) SOA A b) SOA A bis c) SOA B d) SOA C e) SOA D.

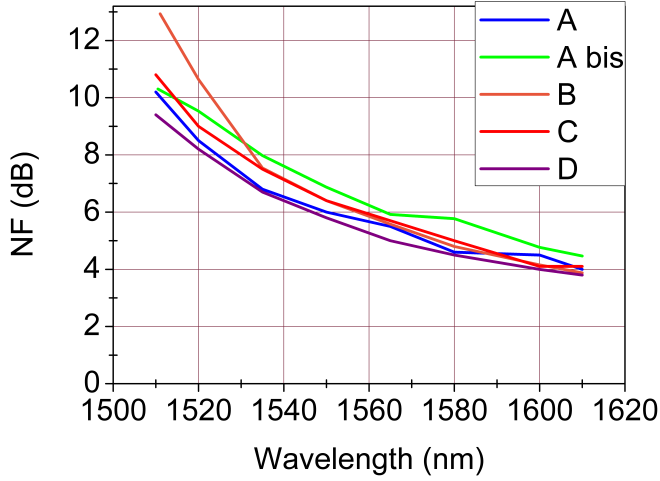


Figure 3.16 – NF of the five SOAs as a function of wavelength at $I = 500$ mA.

3.4.2 Saturation output power

P_{sat} is extracted from plot of gain as a function of optical output power. Its value is read on the graph at $G = G_{max} - 3$ dB. P_{sat} determination is thus a gain measurement with identical set-up as in previous gain measurements. Characterization is done at constant injection current and for different wavelengths. To vary the output power we change input power of the SOA. This is done by using the variable attenuator placed after the laser source. Then when attenuation reaches its minimum value, we use the laser source to keep increasing input power. Unfortunately laser source used for the experiment is limited to 0 dB. It was therefore necessary to add an amplifier to the set-up to reach sufficiently high optical power to measure P_{sat} . We used an C-band Optronix A1904 EDFA with gain of 10 dB.

Narrow bandwidth of EDFA prevented us to measure P_{sat} on the desired bandwidth and we had to restrain our spectrum to four points at 1535 nm, 1550 nm, 1565 nm and 1580 nm for SOAs A, B, C and D. Luckily characterizations realized in the frame of project FUI Calipso went beyond these limits and P_{sat} measurement on an extended bandwidth are presented for design B in the last chapter of this thesis. The EDFA was added for P_{sat} measurements only. Due to its higher gain and lower saturation power SOA A bis could be measured without EDFA, at the same wavelengths than during gain and NF measurements.

Plots of Gain as a function of the output power are shown in Figures 3.17 for the same injection current of 500 mA for all SOAs. Four curves are plotted on each graph, corresponding to chosen wavelengths except for SOA A bis with eight wave-

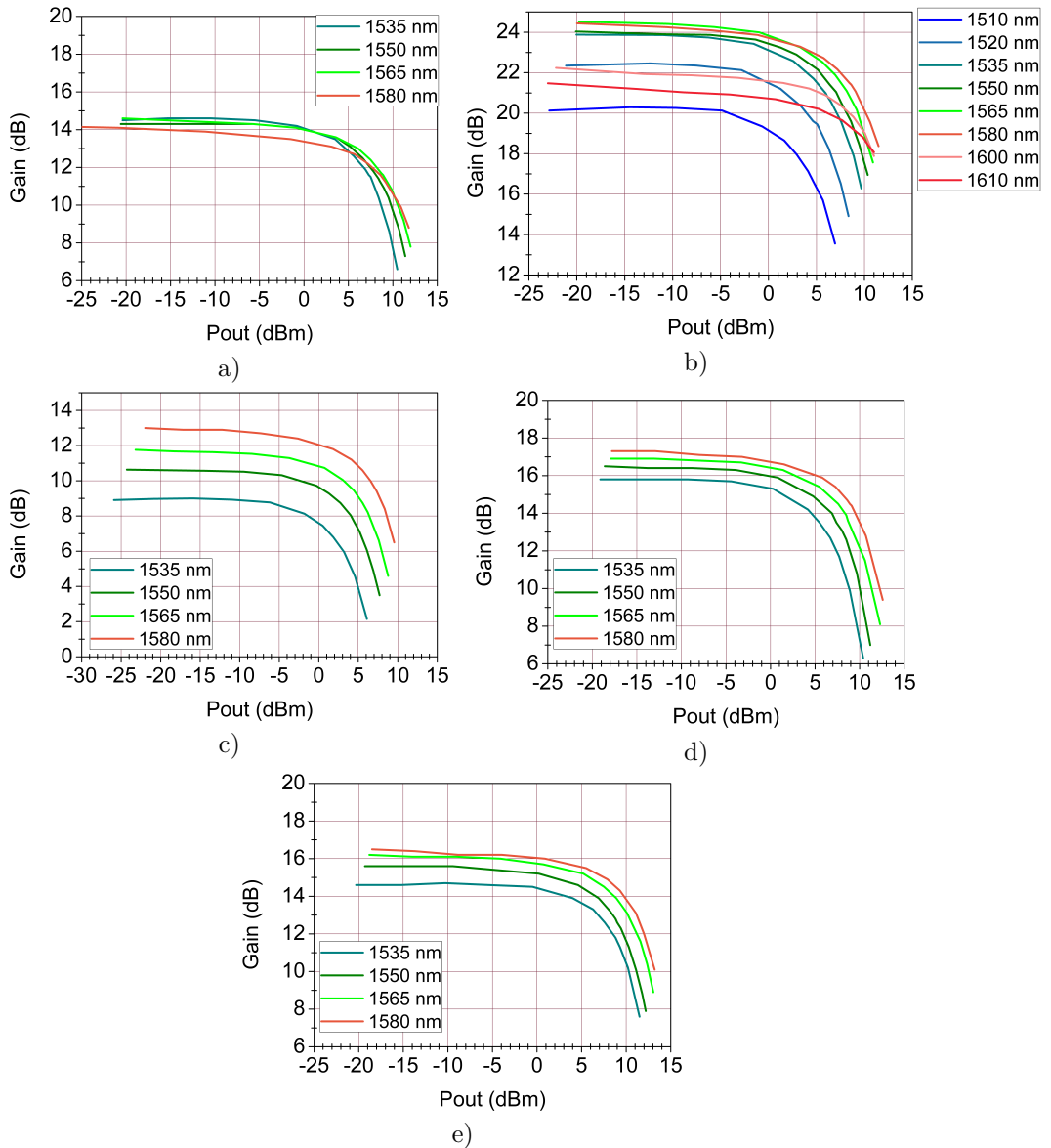


Figure 3.17 – Gain as a function of P_{out} at $I = 500$ mA for different wavelengths for a) Wafer A SOA b) Wafer A bis SOA c) Wafer B SOA d) Wafer C SOA e) Wafer D SOA.

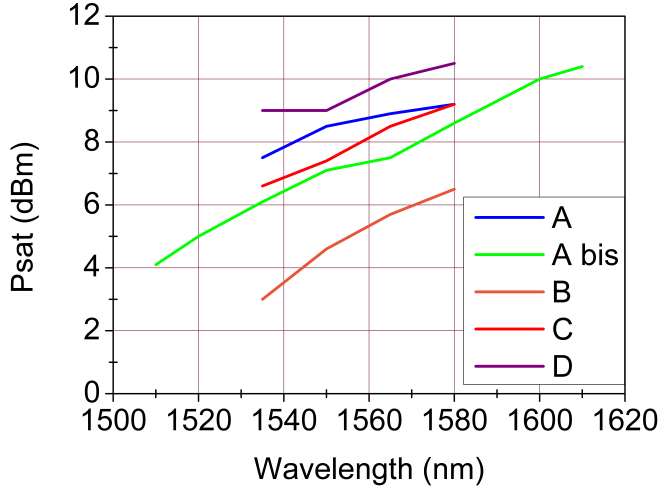


Figure 3.18 – P_{sat} of five designs SOAs as a function of wavelength at $I = 500$ mA.

lengths. P_{sat} values can be extracted from each graph. For an easier interpretation Figure 3.18 displays extracted values for all five SOAs. As predicted by theory P_{sat} is better at longer wavelengths. We also observe that SOA A bis has lowest P_{sat} among all SOAs which is logically caused by its higher optical confinement.

3.5 Impact of temperature

We measured the effect of temperature on SOA A bis. Figure 3.19 shows gain values at three wavelengths for temperatures between 15°C and 50°C . Gain decreases with temperature due to temperature dependence of g_m . This effect is particularly visible at shorter wavelength. At 50°C the SOA has no gain below 1530 nm.

We also present in Figure 3.20 variations of NF for SOA A bis when we vary the value of regulated temperature. Unsurprisingly NF is better at low temperatures. Up to 30°C its variation remains below 1 dB from minimal value but at higher temperature NF increases suddenly at shortest wavelengths showing again the importance of efficient thermal management.

Finally we measured P_{sat} at different currents. Figure 3.21 presents both measurement curves and extracted P_{sat} . We observe an increase of P_{sat} with injection current. This is due to diminution of differential gain a_1 at high carrier density meaning that carrier density variations have less impact on gain. However when

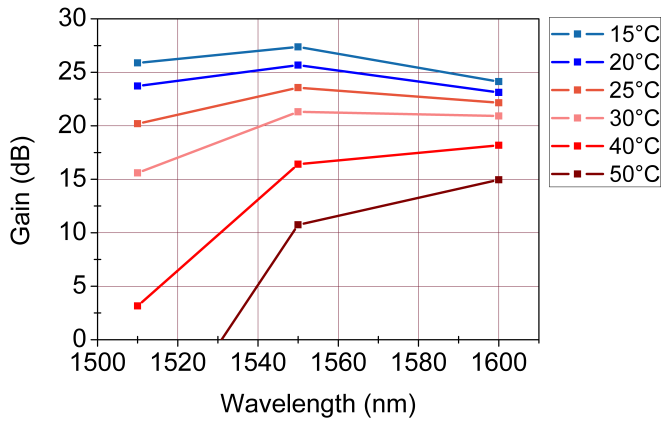


Figure 3.19 – Variation of SOA A bis gain with temperature.

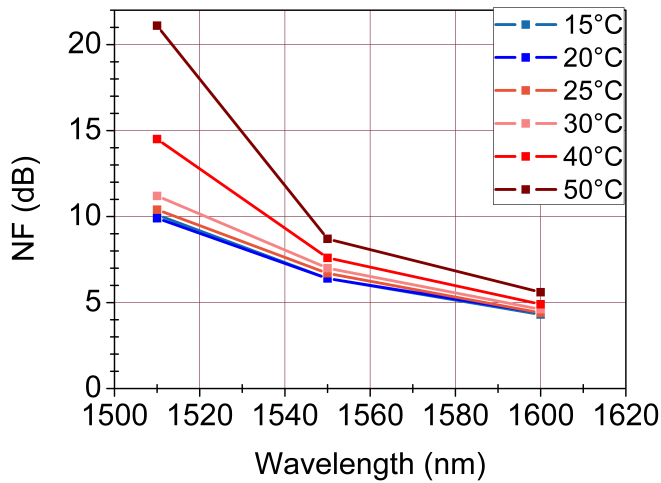


Figure 3.20 – Variation of SOA A bis NF with temperature.

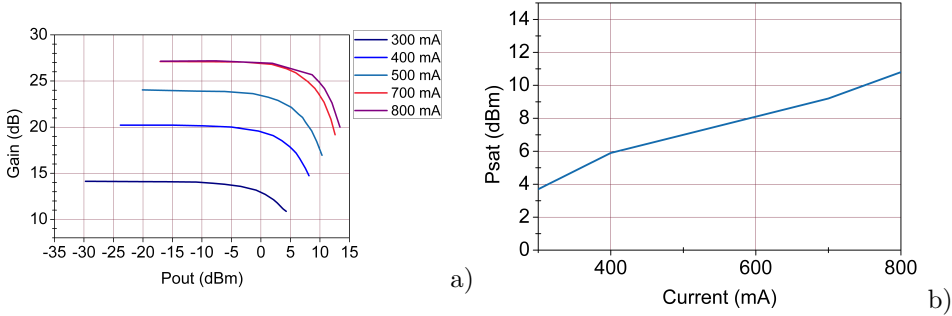


Figure 3.21 – Influence of current on P_{sat} in SOA A bis. a) Curves of gain variations with output power at different currents. b) Plot of P_{sat} as a function of current.

current becomes too high this effect is counterbalanced by temperature elevation and P_{sat} starts decreasing. It appears therefore that temperature regulation plays a critical role in the component performances and must be carefully designed in the SOA packaging.

3.6 Conclusion

We have characterized individual SOAs from our five designs on three different aspects: large gain bandwidth, NF values within this bandwidth and saturation output power at 500 mA. We have also measured their far-field distribution and divergence angles. These measurements show satisfying results on several aspects. First they display a relative homogeneity between the components in the sense that characterized parameters share same order of magnitude for all SOAs. It is very positive as all SOAs originate from variations of the same structure. It demonstrates therefore stability of this original structure. Of course differences also appear in these measurements. But they can mostly be explained by design variations which is a second cause of satisfaction.

Some of the results are remarkable. Optical modes are almost circular with divergence angles between 14° and 20° which helped us to reach coupling losses below 2 dB. Optical gain bandwidth reaches 100 nm for all SOAs and goes probably further for some of them. NF value goes down to 4 dB in the L-band and remains below 7 dB in the whole bandwidth for two designs at 1 A.

Only slightly disappointing aspect is saturation output power with maximum around 10 dBm. However we have reasons to hope for improvement of the performances un-

der real-use conditions. Indeed despite temperature regulation on measuring bench, thermal dissipation is slightly improved when packaged in module and thermal regulation of the chip is more efficient. During project Calipso, a specific module was precisely developed with adapted Peltier module. Furthermore we presented in this chapter measurements at currents close to 500 mA for widest gain spectra. However in real-use scenario injection current is higher to obtain a tilted gain spectrum. We have seen that saturation output power improves at higher currents. We will see in the last chapter of the thesis that measurements on module at high current gave far better results in terms of saturation output power.

CHAPTER 4

Geometry and integration of the semiconductor optical amplifier

In the previous chapters we focused on the development of wideband high power semiconductor optical amplifiers. In this chapter we propose to improve the amplifier performances through waveguide geometry. We first study the impact of the waveguides width in one of our five designs. The rest of our study is done on III-V Lab semiconductor optical amplifiers with a regular bandwidth and comprising an asymmetric cladding for high saturation output power. These amplifiers made of InGaAsP multi-quantum wells operate in the C-band and have 4 μm -wide and 4 mm-long waveguide. We present in the second section a tri-electrodes waveguide to study the effect of current distribution in the amplifier. We finally propose a novel integrated gain measurement method easily implementable in circuit integrated semiconductor optical amplifiers.

4.1 Width of the semiconductor optical amplifier

We have studied in Chapter 2 the optimization of an SOA material structure for high power operation. Starting from Equation 1.9,

$$P_{sat} = \ln(2) \frac{A}{\Gamma} \frac{h\nu}{a_1\tau} \frac{G_0}{G_0 - 2}$$

We have proposed a solution to improve P_{sat} by adding an asymmetric cladding beneath the MQW which drags the optical mode down, thus decreasing Γ . This solution also allows single-mode operation of wider waveguides and enlargement of the waveguide is beneficial to P_{sat} through the increase of $A = \text{width} \times \text{thickness}$ and to limit the device heating under operation. In this section we propose an experimental study of the waveguide width impact on P_{sat} , gain and NF.

4.1.1 Study of different SOA widths

In this study we consider three SOAs from our reference structure A. These 4 mm long SOAs are identical except for their waveguide width of 4 μm , 4.5 μm and 5 μm . Characterizations of the 5 μm waveguide were already presented in Chapter 3, we now compare them with equivalent measurements of the two other waveguide widths. We start with comparison of far-field measurements to control potential changes of the optical mode geometry. Figure 4.1 presents 2D far-field measurements. The three modes look alike and present a quasi-circular shape. Figure 4.2 presents these measurements at 0° (horizontal axis) and 90° (vertical axis), fitted with a Gaussian profile. Extracted values of the divergence angles θ_h and θ_v are compared with simulations in Table 4.1. While vertical divergence remains almost the same, horizontal divergence angle is more sensitive to the waveguide width reduction and we obtain: $\theta_{h4\mu\text{m}} > \theta_{h4.5\mu\text{m}} > \theta_{h5\mu\text{m}}$. However at 4 μm it appears in Figure 4.2 that the beam does not fit a Gaussian profile anymore. Obtaining a quasi-circular beam for the 5 μm -wide waveguide is a very good result and proves optimization of the cladding. Regular material structures indeed usually result in much thinner waveguide width limit for single mode operation.

We then present the same measurements already performed on the five designs: ASE, gain, NF and P_{sat} spectra. Measurements are done with the same experimental set-up and methods. Temperature is regulated at 25°C . Measurements of the three different widths are grouped on the same graphs in Figure 4.3. Starting with ASE spectra we immediately observe that the flat spectrum current is different depending on the waveguide width. Blue and dashed orange curves show indeed ASE spectra of the 5 μm and 4.5 μm wide SOAs at 400 mA and display different

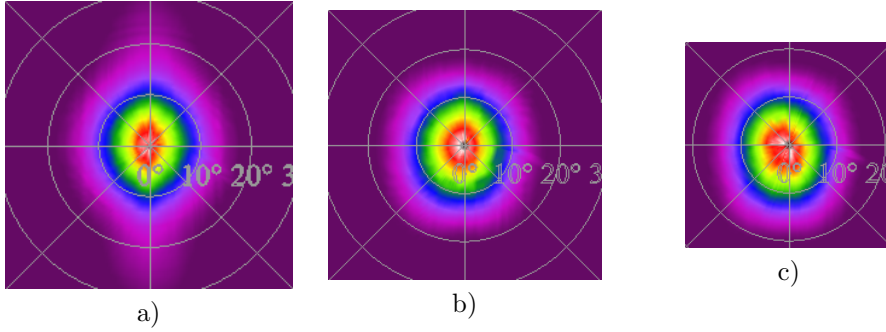


Figure 4.1 – Optical mode farfield measurement for a waveguide width of a) $4 \mu\text{m}$ b) $4.5 \mu\text{m}$ c) $5 \mu\text{m}$.

Waveguide width	Simulated divergence		Measured divergence		Simulated Γ_{QW}	Simulated Γ_p
	h	v	h	v		
$4 \mu\text{m}$	17.7°	19.1°	16.6°	18.6°	4.6%	8.4%
$4.5 \mu\text{m}$	16.9°	19.5°	16.2°	18.5°	4.7%	8.7%
$5 \mu\text{m}$	16.1°	19.8°	15.1°	18.4°	4.8%	8.8%

Table 4.1 – Comparison of simulated and measured divergence angles for three waveguide widths. h stands for horizontal divergence and v for vertical divergence.

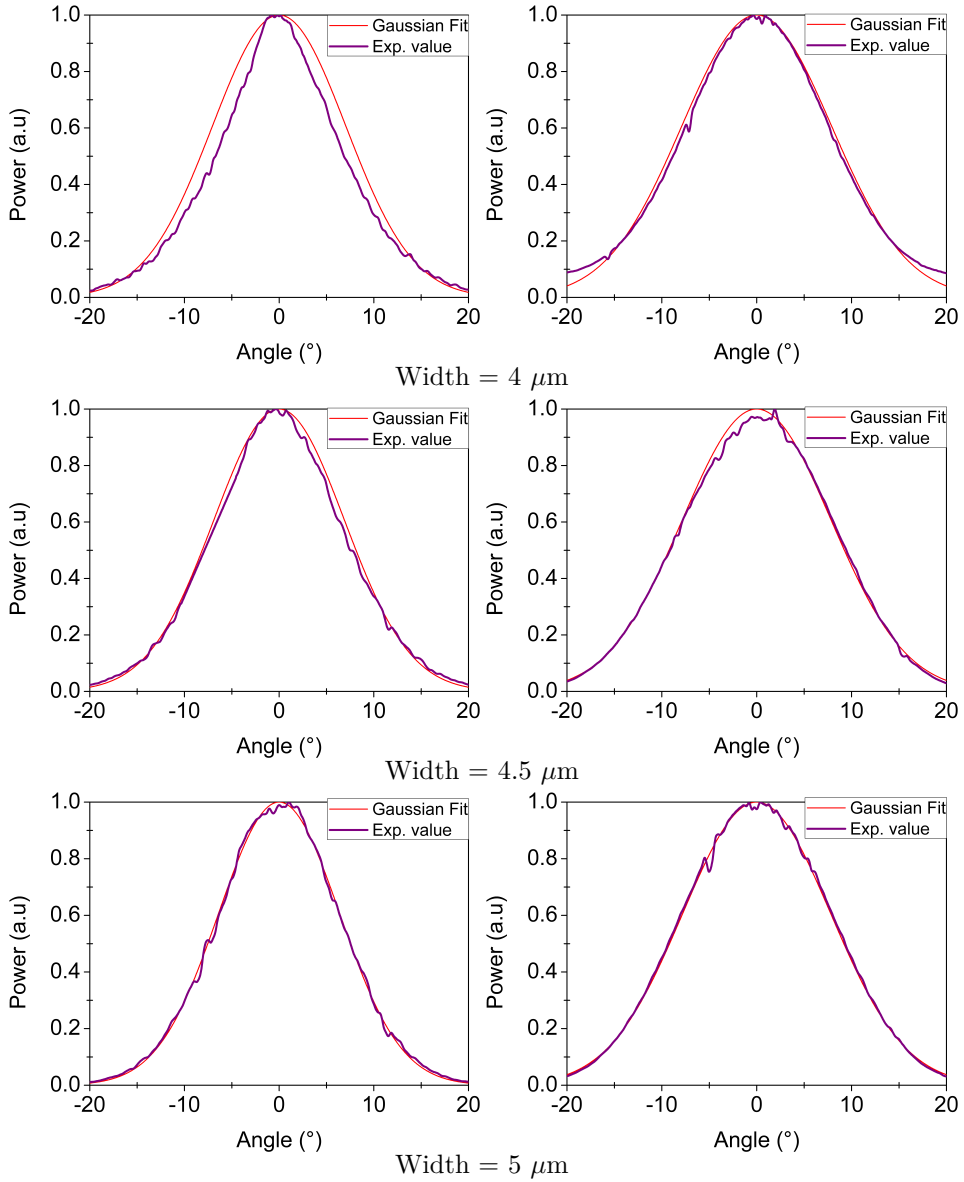


Figure 4.2 – Horizontal (left column) and vertical (right column) farfield profiles fitted with Gaussian profile.

Equivalent injection currents		
4 μm	4.5 μm	5 μm
320 mA	360 mA	400 mA
400 mA	450 mA	500 mA

Table 4.2 – Table of correspondence between injection currents of different widths SOAs for identical current density.

behaviors. The second energy transition is clearly visible on the orange curve, indicating that we are beyond flat spectrum current, while the blue curve is at its flattest. Flat spectrum current is therefore lower in the 4.5 μm wide SOA than in the 5 μm one. This difference arises from the SOA surface reduction when the width is decreased. Indeed flat spectrum current value is related to carrier density in the SOA which determines filling of the energy levels. Carrier density is itself directly linked to current density in the component j , defined as follows:

$$j = \frac{I}{S} \quad (4.1)$$

with I electrical current and S injected surface. In a 4.5 μm wide SOA, S is reduced compared to a 5 μm wide SOA. For the same current we have therefore $j_{4.5\mu\text{m}} > j_{5\mu\text{m}}$ meaning that flat spectrum current is reached at a smaller current. We added ASE spectra of 4 μm and 4.5 μm wide SOAs at their respective flat spectrum currents to the plot. All curves are normalized except for the 4.5 μm wide SOA at 500 mA to illustrate further increase of ASE power at higher current density. Other three ASE spectra are very similar.

A measurement problem with the 4 μm -wide SOA made gain and NF measurements difficult and we only present experimental result of both other widths. Figure 4.3 b) shows gain spectra of the 4.5 μm and 5 μm -wide SOAs at their respective flat gain currents with addition of the 4.5 μm wide SOA gain spectrum at 500 mA to illustrate flat gain current discrepancy between both SOA widths. Table 4.2 presents current equivalences for the three waveguide widths. When taken at their respective flat gain currents both SOAs show the same gain spectrum shape although at different values. Gain is higher for the broader SOA. This variation of gain mainly originates from variation of optical confinement shown in Table 4.1. We have then in Equation 1.1,

$$G_{chip} = \exp[(\Gamma g_m - \alpha)L]$$

Thus increasing gain in larger SOAs. However change in the waveguide width also slightly modifies optical confinement in the lossy p-doped layers, thus further impacting G_{chip} through α .

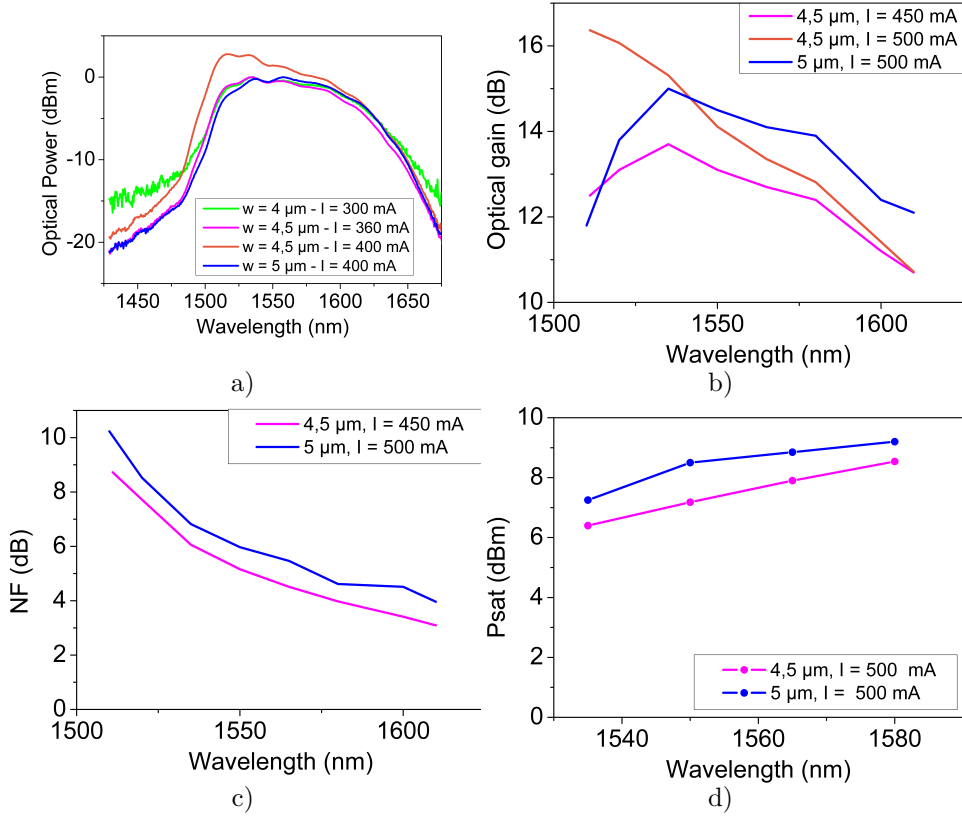


Figure 4.3 – Measurements of 4 μm , 4.5 μm and 5 μm wide SOAs. a) ASE spectra b) Gain spectra c) NF and d) P_{sat} .

Finally Figure 4.3 c) and d) present NF and P_{sat} measurements. NF seems to be better in the narrower 4.5 μm SOA which might be due to lower confinement in the p-layer. As expected we observe better P_{sat} in the wider SOA. We have seen in Chapter 3 that P_{sat} increases with current. Our measurements were all done at 500 mA meaning that current density is higher in the narrower waveguide. Despite having a lower current density in this measurement, P_{sat} is still better in the wider SOA as expected. Wider 5 μm waveguide SOA therefore proves to have higher gain and P_{sat} . We propose to push further in this direction by designing very wide SOA waveguides for higher P_{sat} , presented in the following subsection.

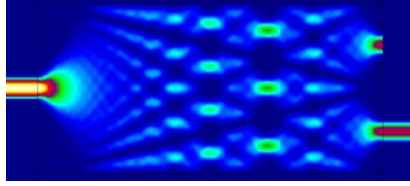


Figure 4.4 – Interference pattern along a 1:2 MMI with one input and two output waveguides.

4.1.2 Multimode interferometers

A multimode interferometer (MMI) is a broad waveguide whose large width allows guiding of many optical modes. Usually coming from a single-mode waveguide, a light signal entering the MMI waveguide will be distributed on the different MMI eigen modes. These modes propagate independently at different speeds due to their distinct propagation constants. Coexistence of these optical modes creates a periodic interference pattern along the waveguide and depending on position, the signal power distribution changes, as illustrated in Figure 4.4. Depending on position in the waveguide, propagating signal power can be distributed on one, two or more precise spots. This property can be used to split signal into multiple waveguides by designing the waveguide length to place output on one of these positions. MMIs therefore find multiple applications in photonic integrated circuits (PICs) where they are usually used as passive components.

We propose to develop an active MMI SOA for high power applications. We want to design a very wide SOA to enhance its P_{sat} and make use of MMI interferometric properties to remain single mode at the SOA output. In a MMI despite operating multimode we are able to recover all signal in a single-mode waveguide by adjusting the MMI length due to periodicity of the interferometric pattern. Starting from our fixed material structures I performed propagation simulations to determine waveguide thickness and length giving expected behavior. Simulations were done using Fimmprop software, an extension of Fimmwave previously used to design our material structure. It allows to simulate propagation of a light beam injected in a waveguide through a defined input port and extracts fraction of signal power transmitted at chosen output port.

We choose to limit total surface of the MMI to about $20000 \mu m^2$ which is the surface of a $5 \mu m \times 4 mm$ waveguide. Bigger surfaces indeed necessitate higher currents to obtain a sufficient carrier density for SOA operation. Knowing that a larger waveguide has a longer periodicity this restriction limits the number of acceptable width \times length couples ($W \times L$). We start with $W = 20 \mu m$ to obtain a really multimode waveguide and simulate propagation in such waveguide to determine

periodicity of the reunion of all modes in one spot. By placing an output port at this particular point we are able to simulate transmission of the waveguide. Transmission T can vary between 0 when no light is transmitted to the output port and 1 when when all light is transmitted. In our case we want T as close to 1 as possible to recover all signal. We then varied W and L to find best design. We finally obtained the following MMI: $W = 20.65 \mu\text{m}$ and $L = 1010 \mu\text{m}$ giving $T = 0.93$ for a total surface of $20.856.5 \mu\text{m}^2$. This design has been fabricated but had not been characterized when these lines were written.

4.2 Multi-electrode semiconductor optical amplifier

We have already noted in previous sections the improvement of P_{sat} at higher currents. It is due to decrease of differential gain a_1 which links material gain to carrier density variations. dg_{mat}/dn decreases as carrier density increases. Current increase also improves NF and gain but also elevates the SOA temperature which can be detrimental to its performances. Furthermore for some applications main parameter to control is the optical gain. In this case, injection current is fixed to obtain desirable gain value and might not be high enough for optimized P_{sat} and NF.

A solution can be found by considering optimization of each parameter separately. Indeed saturation output power only matters at the SOA output as optical power increases gradually along the component and reaches high values toward its end. On the other hand NF is critical at the input of the SOA [100], as it will then be amplified along the waveguide, whereas noise at the output does not change much. It is even different for gain which is built throughout the SOA length. Thus each parameter optimization depends on a different section of the SOA. Input section needs high injection current to lower NF, output section also needs high current operation to increase P_{sat} and middle section might need a lower injection current depending on desirable gain value. If we split the SOA into three independent sections we can inject each of them separately to optimize all parameters.

4.2.1 Three-electrode amplifier

SOA waveguide is uninterrupted and division in three electrodes is done at the metallization and implantation levels as illustrated in Figure 4.5. Insulation between the electrodes allows independent electrical injection.

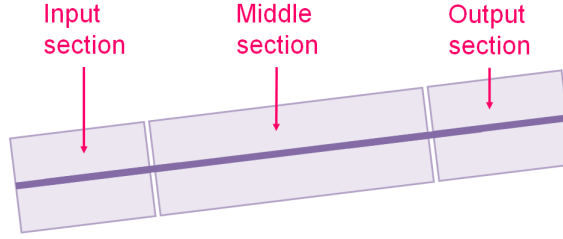


Figure 4.5 – Picture of a three-electrode SOA.

Middle section is the longest electrode: as gain directly depends on the SOA length, keeping input and output sections smaller helps us keeping good control of gain through middle section injection current. However we do not know in advance what length of input and output sections will have the greater effect. For the same component total length of 4 mm we therefore designed two different electrode lengths: 240 μm and 990 μm . In these first designs we use the same length for both input and output electrodes. By comparing the effect of current increase on the input and output sections we wanted to determine which length was more adapted. However preliminary measurements have not allowed us to select one length in particular and we only present results of the SOA with 990 μm -long electrodes.

4.2.2 Experimental results

The purpose of our measurement campaign is to show improvement of NF and P_{sat} when increasing injection current on the input and output electrodes. We start with measurement of the SOA gain, NF and P_{sat} at identical current density on all three section. Given the size difference between electrodes, injection current must be adapted to maintain the same current density on all electrodes. Table 4.3 shows correspondence of injection current for the three electrodes depending on their sizes. In the following measurements we will be referring to input electrode as E_1 and corresponding injection current as I_1 . Similarly we will use E_2 and I_2 for the middle electrode and E_3 and I_3 for the output electrode.

We first present ASE plots at different currents and for an identical current density on all three SOA electrodes in Figure 4.6. We choose for our measurement three wavelengths around the center peak: 1510 nm, 1530 nm and 1550 nm. We study the impact of I_1 and I_3 on NF and P_{sat} . Figure 4.7 presents gain, NF and P_{sat} measurements at 1510 nm, 1530 nm and 1550 nm as a function of injection current I_2 . At the same time, I_1 and I_3 are tuned to keep condition $I_1 = I_2/2 = I_3$ for a uniform current distribution. Measured values are compliant with expected behavior: gain increases with current and is higher at longer wavelength for low current

Equivalent injection currents	
$L = 990 \mu m$ ($E_1 \& E_3$)	$L = 2000 \mu m$ (E_2)
25 mA	50 mA
50 mA	100 mA
75 mA	150 mA
100 mA	200 mA
125 mA	250 mA
150 mA	300 mA
175 mA	350 mA
200 mA	400 mA
225 mA	450 mA

Table 4.3 – Table of correspondence between injection currents for both SOA sections depending on their length.

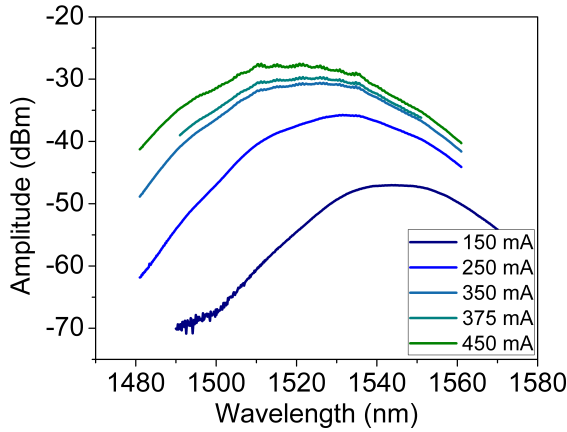


Figure 4.6 – Variation of ASE power as a function of injection current with identical current density on all sections. Current applied on the middle section is indicated in the legend.

values. Then as current increases, gain starts increasing at shorter wavelengths and even becomes higher at 1510 nm than 1550 nm.

On the other hand NF decreases at higher current due to reduction of population inversion factor n_{sp} . Population inversion factor tends towards unity for a complete population inversion. n_{sp} is also higher at shorter wavelengths which explains NF difference between wavelengths. We obtained P_{sat} of 8 dBm at 1510 nm, 9.4 dBm

at 1530 nm and 10.8 dBm at 1550 nm. P_{sat} is higher at longer wavelengths but also increases at higher injection currents.

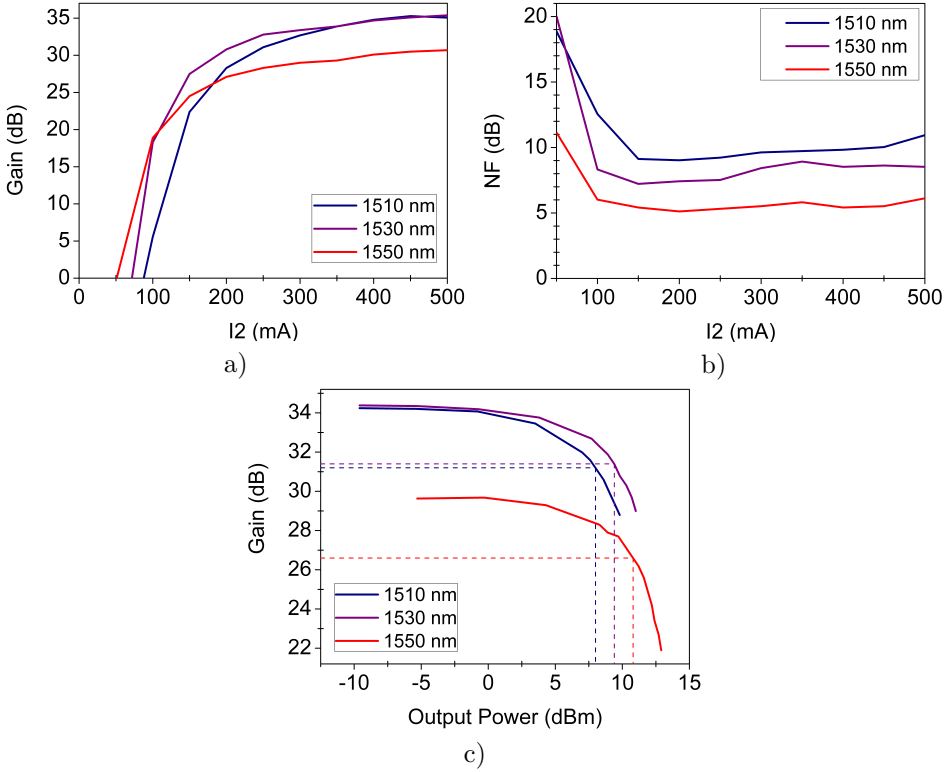


Figure 4.7 – Variation of gain (a), NF (b) and P_{sat} (c) of SOA_{990} with current for an identical current density on the three electrodes. P_{sat} is measured at $I_1 = I_2/2 = I_3 = 125$ mA.

To observe the effect of E_1 injection current we fix I_2 and I_3 , with $I_3 = I_2/2$. We then measure gain and NF as a function of I_1 . Figure 4.8 a) shows gain measurements at 1510 nm, 1530 nm and 1550 nm. Dash lines represent gain value at $I_1 = I_2/2 = I_3$, uniform current density. We can observe that gain curves cross the dash lines at the point where uniform current density is reached, around $I_1 = 125$ mA. Gain does not really increase for higher values of I_1 . From these observations we deduce that the impact of I_1 on optical gain is limited at high currents. Figure 4.8 b) shows an equivalent NF measurement. We observe that NF value decreases below uniform current density value by 1.5 dB at 1510 nm when I_1 increases. However the impact of I_1 increase on this improvement is questionable as at $I_1 = 125$ mA we already have $NF = 8.2$ dB, almost 1 dB less

than on our previous measurement, despite identical current density on the three SOA electrodes. No improvement is visible at longer wavelengths. Nevertheless a more visible effect is expected at 1510 nm due to wavelength dependence of population inversion factor n_{sp} . At considered current densities n_{sp} already seems to reach its minimum at 1530 nm and 1550 nm but can be brought to its optimal value at lower wavelengths by increasing carrier population through I_1 .

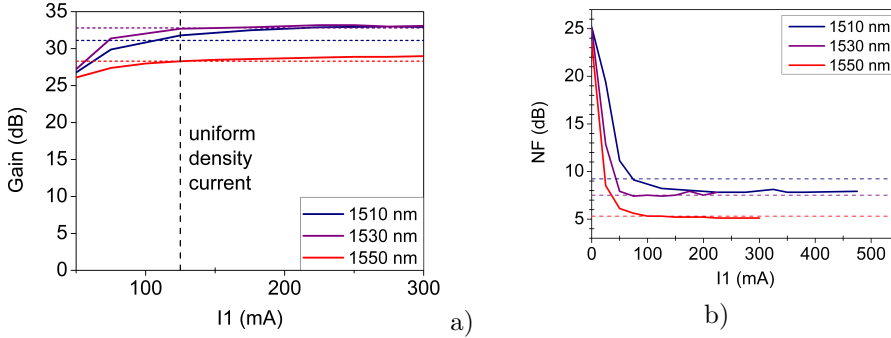


Figure 4.8 – Effect of I_1 variation on gain (a) and NF (b) for a given current density on E_2 and E_3 : $I_2/2 = I_3 = 125 \text{ mA}$.

We then tune I_3 to see the effect on P_{sat} . Figure 4.9 first shows gain and NF variations with I_3 . We observe an increase of gain of 3.4 dB at 1510 nm and 1.2 dB at 1550 nm. Greater effect observed compared to I_1 variations may be related to the expected increase of P_{sat} . Indeed when increasing I_1 , gain also increases but with a P_{sat} of 8 dBm at 1510 nm and 9.4 dBm at 1530 nm and a P_{in} of -25 dBm we are limited to a gain of 33 dB at 1510 nm and 34.4 dB at 1530 nm which is about what we obtain when varying I_1 . However when increasing I_3 , we also increase P_{sat} and are able to reach higher gains. As for NF there is a noticeable difference from I_1 variations. NF value remains the same at 1550 nm, close to uniform current density value. But at 1510 nm, NF is surprisingly low at low currents and slowly tends towards its uniform current density value. Further measurements must be done to understand this behavior.

We measured P_{sat} at 1510 nm, 1530 nm and 1550 nm while increasing I_3 . Plots of optical gain as a function of output power are presented in Figure 4.10 and P_{sat} extracted values are given in Table 4.4. Optimal current value for all wavelengths seems to be 375 mA with more than 2 dB increase compared to uniform current density values. At higher current, P_{sat} either remains the same or decreases, possibly due to thermal effects. Figure 4.11 summarizes changes in gain, NF and P_{sat} for $I_3 = 375 \text{ mA}$. We can see limited effect on NF while gain is slightly increased and P_{sat} even more.

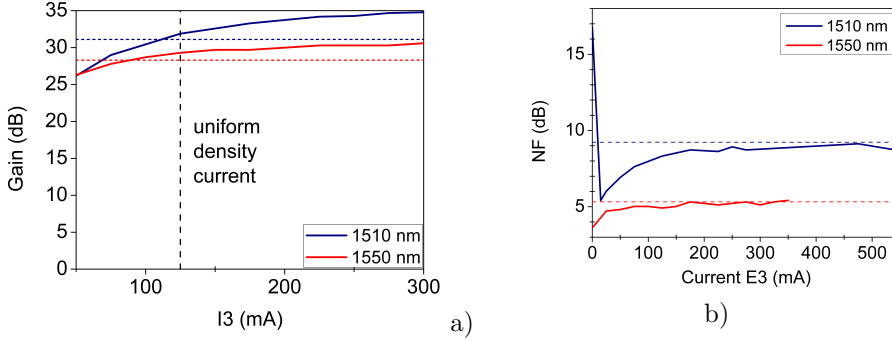


Figure 4.9 – Effect of I_3 variation on gain (a) and NF (b) for a given current density on E_2 and E_3 : $I_2/2 = I_3 = 125$ mA.

I_3	P_{sat}		
	at 1510 nm	at 1530 nm	at 1550 nm
175 mA	10.2 dBm	9.6 dBm	11.4 dBm
275 mA	12.2 dBm	12.2 dBm	12.7 dBm
375 mA	12.2 dBm	13.5 dBm	14 dBm
475 mA	11.1 dBm	12.8 dBm	13.8 dBm

Table 4.4 – Extracted values of P_{sat} at 1510 nm, 1530 nm and 1550 nm for different high values of I_3 , at $I_1 = 125$ mA and $I_2 = 250$ mA.

We see a strongly wavelength dependent effect of I_1 and I_3 on NF and P_{sat} . Shorter wavelengths which normally show worst performances in terms of NF and P_{sat} are very sensitive to current increase on E_1 and E_3 . This slightly compensates wavelength dependence of NF and P_{sat} . The tri-electrode configuration clearly improves performances of the amplifier as summarized in Figure 4.11. Further measurements will be necessary to better understand the different effects but given the relatively easy implementation of the three-electrode solution and its encouraging results it already seems like a good approach to push an amplifier performances.

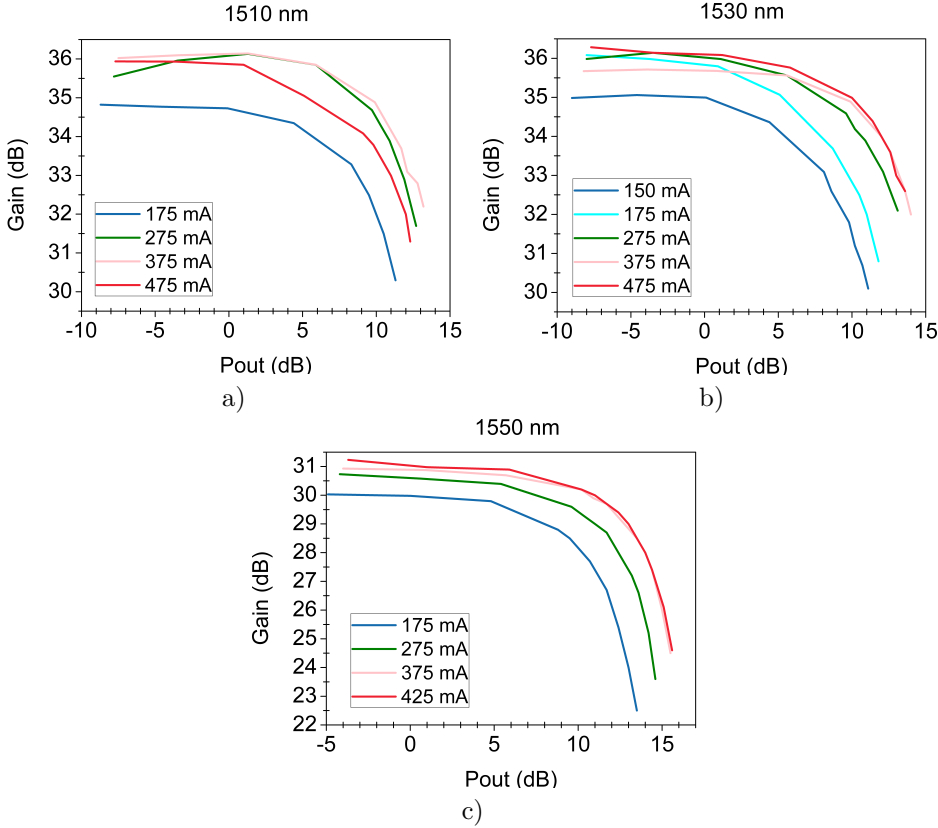


Figure 4.10 – Optical gain as a function of output power at $I_1 = I_2/2 = 125 \text{ mA}$ at different values of I_3 for a) 1510 nm, b) 1530 nm and c) 1550 nm. Effect of I_3 variations on P_{sat} .

4.3 Integrated gain measurement

4.3.1 Applications

Gain measurement method presented in Chapter 3 is mainly addressed to preliminary characterization on non-packaged chips. Indeed in their final applications, SOAs are often integrated in a module or a more complex circuit. In these situations it becomes complicated to access the chip parameters like gain and NF without contribution of surrounding optics or components. Although it is not always critical, keeping a direct access to the SOA parameters can be useful to monitor

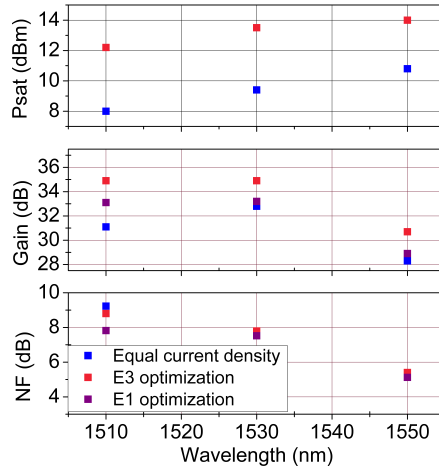


Figure 4.11 – Comparison of gain, NF and P_{sat} at uniform current density and for $I_3 = 375 \text{ mA}$ and $I_1 = 300 \text{ mA}$.

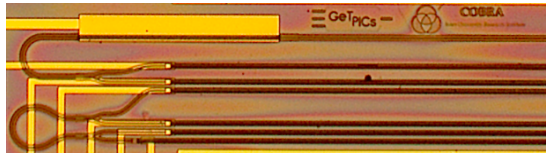


Figure 4.12 – Picture of a PIC including a SOA.

its performances during use for dynamic gain control with injected current, and analyze failures without having to disassemble the whole device.

Integration of SOAs in PICs is a good example of this scenario. SOAs are one of the base blocks for PICs due to their small size and easy integration with other photonic components. Figure 4.12 shows an SOA integrated in a PIC. SOAs can be used along with lasers and modulators on the emitter side, or in receptors before a photodiode. Integrating several components together presents the advantage of compactness and can lower the cost of the assembled circuit compared to individual components brought together later.

However in these configurations, access to optical input and output power is often impossible as the component facets are not accessible. This configuration therefore prevents any gain measurement. Monitoring power gain of PIC SOA gives nevertheless better control of performances and provides understanding of environmental effects on the device. There is therefore a real interest in finding an adapted gain measurement method.

4.3.2 Proposed method

Different methods have been proposed for direct in-use measurement of gain. A thermal characterization for instance which links temperature difference between SOA surface and a reference temperature to optical input power in order to evaluate gain [10, 11]. Despite good results the technique may not be incorporated in a measurement routine as it requires a specific set-up for an accurate temperature characterization. Other groups have linked optical gain with spontaneous emission (SE) of the SOA, either by a relation between SE intensity and gain [12] or by correlating the amplified spontaneous emission (ASE) peak wavelength to optical gain [13]. Newkirk et al. also proposed to divide the SOA in three sections and derived a relation between gain and ratio of input and output sections voltages [14]. These methods require calibration, often by a traditional gain measurement and remain indirect evaluations of the SOA gain.

We recall that direct characterization of the gain is given by the ratio between output and input signal without ASE contribution. These parameters can be measured by collecting fraction of the light with photodiodes as presented in [15]. With this method, two photodiodes collect part of the light reflected on coupling lenses at the input and output of a SOA. To adapt this method to PIC SOAs a solution must be found to integrate photodiodes on-chip. In the past a partial solution consisting of using an integrated photodiode to collect fraction of the output signal has been used in SOA for gain monitoring. However with this method the SOA input power must still be known to derive optical gain [16].

We propose a more complete method which makes use of two integrated photodiodes for on-chip optical gain characterization of SOA with possible use in PIC. A pair of identical coupled waveguides placed at input and output facets collect the same small fraction of signal for each photodiode.

4.3.3 Design and simulations

At first, implementation is done on a single SOA for easy comparison with classic method of gain measurement. Propagation simulations were done to design the coupling section. Coupling occurs between two nearby waveguides when they are close enough. For two waveguides with the same composition, coupling mainly depends on their width, spacing and length. These two parameters change what fraction of the signal is transmitted from one guide to the other and with which periodicity. Optical propagation simulations were done to design our coupled waveguides. Coupled waveguide width was fixed at $4 \mu\text{m}$ while in the coupling region the main waveguide width was reduced to $2.5 \mu\text{m}$. Spacing between waveguides is set at 1.8

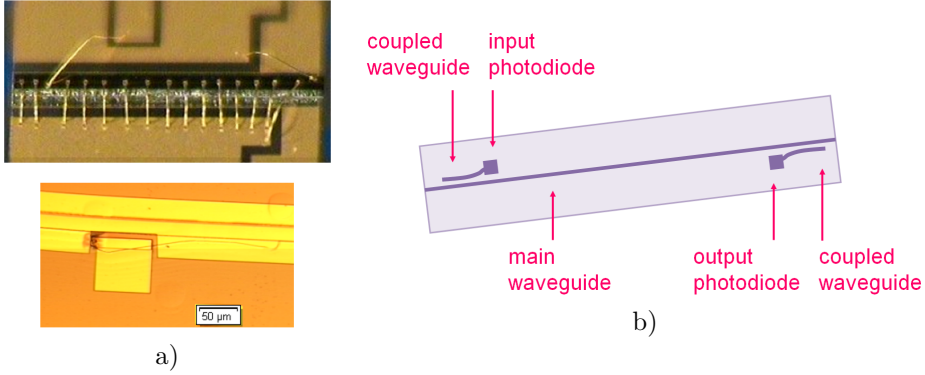


Figure 4.13 – a) Above, picture of SOA and integrated photodiodes. E_{phd} indicates the photodiodes electrodes. Photodiodes are located at the waveguide input and output. Below, detail of the photodiode. b) Schematic representation of SOA with integrated photodiodes.

μm for a $70 \mu\text{m}$ length. This length allows transfer of a small fraction of light of about 3% from the main guide to the secondary guides leading to the photodiodes. As collected light is lost for amplification we need to keep the amount of collected light as low as possible while detectable. Coupling length might be made shorter by putting the waveguides closer but spacing is limited by technological process. If spacing is too small we are not able to etch between the waveguides.

Figure 4.13 a) shows the entire chip with bonding separating electrodes for both photodiodes. A close view of a photodiode is also presented. Figure 4.13 b) presents a schematic representation of the device for clarity. Both photodiodes and coupled waveguides are identical to ensure the same responsivity.

4.3.4 Experimental set-up and results

To measure optical gain of the amplifier, the SOA is polarized at different currents while photodiodes are polarized at a fixed voltage of -1V to ensure total absorption of optical signal. A C-band Tunicas tunable laser provides optical input signal at -23 dBm and temperature of the SOA is regulated at 25°C .

Photocurrent from a photodiode is linked to optical power by the following relation :

$$I_{ph} = B \times P \quad (4.2)$$

With B the photodiode responsivity in A/W . Here responsivity is the same for

both photodiodes and we have therefore:

$$\begin{aligned}
 G_{chip} &= \frac{P_{out}}{P_{in}} \\
 &= \frac{(P_{out \text{ measured}} - P_{outASE})}{(P_{in \text{ measured}} - P_{inASE})} \\
 &= \frac{(BP_{out \text{ measured}} - BP_{outASE})}{(BP_{in \text{ measured}} - BP_{inASE})} \\
 &= \frac{(I_{out} - I_{outASE})}{(I_{in} - I_{inASE})} \tag{4.3}
 \end{aligned}$$

with I_{out} output photocurrent with signal, I_{outASE} output photocurrent when $P_{in} = 0$, I_{in} input photocurrent with signal and I_{inASE} input photocurrent when $P_{in} = 0$. For gain characterization we measured at each current of interest both input and output photocurrents, first without input signal ($P_{in} = 0$) to identify ASE contribution, then with signal. Following Equation 4.3 we can calculate gain from photocurrent measurement. This measurement method does not take into account coupling losses, as optical power is measured inside the SOA chip. It represents therefore intrinsic chip gain G_{chip} .

Figure 4.14 a) shows measured gain at six different currents. We observe the expected increase of gain with injection current but gain curve is a bit noisy especially at higher currents. We plot in Figure 4.15 $I_{in} - I_{inASE}$ and $I_{out} - I_{outASE}$, used in gain calculation. Experimental curves become noisier at higher currents. An explanation might be that an insufficient fraction of light is coupled into the photodiode resulting in higher sensitivity to noise. We are also investigating the possibility that spontaneous emission might diffuse into the photodiode. To solve this problem we propose for next designs to increase the fraction of light collected in the photodiode and move the photodiodes away from the main waveguide.

To compare photocurrent method with classic gain characterization, the later is performed on the SOA in the same conditions, with no polarization on the photodiodes. An optical fiber is coupled at the SOA output and optical spectrum is read on an Anritsu MS9710B OSA. Amplified signal and ASE levels are extracted from the spectrum, and knowing input power, gain can be calculated [53]. This method is sensitive to coupling losses, and gives more usable fiber-to-fiber gain. Measured gain is shown in Figure 4.14 b). SOA gain bandwidth is centered in 1550 nm and is slightly smaller than 30 nm.

Correction with coupling losses is done for comparison with previously obtained intrinsic values. Coupling losses are measured at 2.5 dB for each facet. Figure 4.16 shows gain characterization with both methods at different currents for wavelengths between 1525 nm and 1560 nm. Good consistency is found between both approaches despite photocurrent gain measurement getting noisy at higher currents.

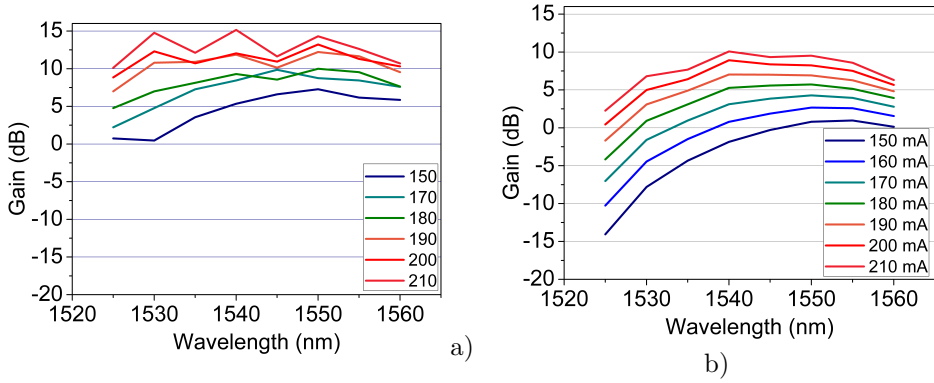


Figure 4.14 – Gain spectra at different currents a) measured with integrated photodiodes. b) measured with classic method.

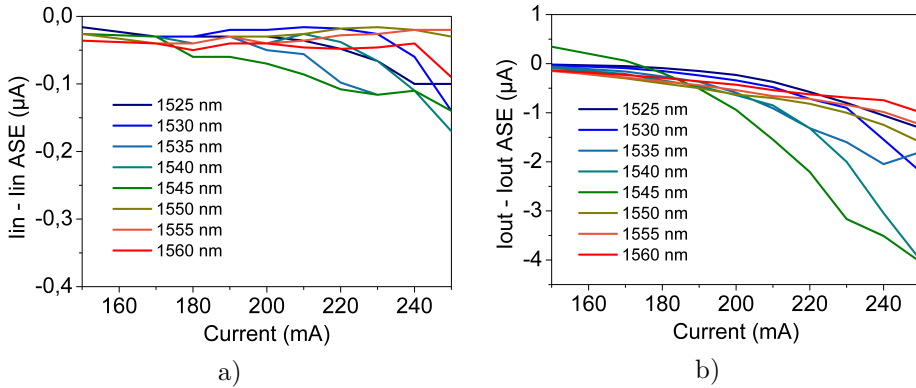


Figure 4.15 – Variation of $I_{in} - I_{inASE}$ (a) and $I_{out} - I_{outASE}$ (b) as a function of current at different injected signal optical wavelengths.

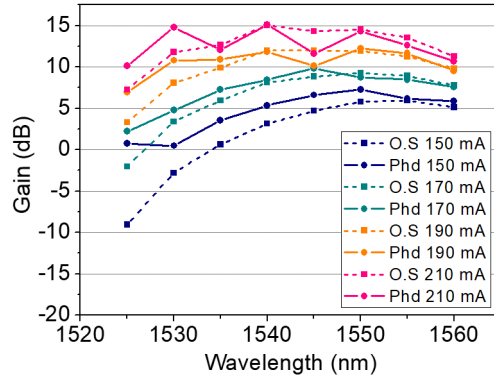


Figure 4.16 – Simultaneous plot of gain spectra measured without coupling losses. Dashed lines correspond to optical spectrum and with conventional method while straight lines correspond to photocurrent method.

4.4 Conclusion

In this chapter we have presented two studies on the optimization of a SOA performances. We have first studied the impact of SOA width on its performances and showed how a larger waveguide leads to better gain and saturation output power, as long as the waveguide remains single-mode. We have then demonstrated an improvement of noise figure and saturation output power dividing the SOA into three sections and injected higher current in the input and output sections. Finally we proposed an integrated gain measurement method with several potential applications.

When previous chapters focused on the SOA material composition, work presented in this chapter shows the importance of the SOA geometry. It is all the more interesting as geometry of a component can easily be varied, even on the same wafer whereas material composition is fixed for all components. Solutions like the ones presented in this chapter can therefore be more easily implemented.

Applications

We finally present in this chapter two applications based on our wideband SOAs. First application integrates two SOAs in a polarization independent module for wideband amplification in access or data center interconnect transmissions. Second application integrates a reflective SOA (RSOA) into a tunable hybrid external-cavity laser where the SOA large bandwidth allows very wide tuning range. Both applications show very promising performances and resulted in publications.

5.1 Reach Extender for Optical Access Networks

We present the performances of an in-line S+C+L band amplifier for access and datacenter-interconnects. It is composed of a polarization insensitive module featuring two SOAs incorporating the same broadband material from design B. As presented in the introduction chapter, in access networks a SOA is needed at the optical line terminal in the central office as downstream booster and upstream pre-amplifier [21]. For NG-PON2 standard, the optical bandwidth starts at 1524 nm for the upstream and expands till 1603 nm for the downstream [68] therefore requiring a wide gain component. Datacenter interconnects on the other hand, could make use of the additional channels an extended bandwidth can offer. State-of-the-art MQW SOA [101] exhibits a saturation output power (P_{sat}) of 20 dBm and noise figure

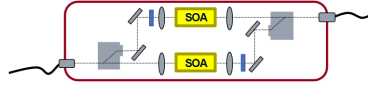


Figure 5.1 – Schematic representation of the polarization diversity module.

(NF) of 6 dB. Comparable results were obtained with a packaged low-confinement SOA reaching the minimum NF value of 4.5 dB at very large current [102]. By integrating our wideband SOAs in a dedicated module we want to propose such performances on a gain bandwidth superior to 100 nm.

5.1.1 Project presentation

Frame to develop such module was French FUI project Calipso, introduced at the beginning of chapter 2. Main purpose of the project was to make a polarization independent SOA module with gain bandwidth over 100 nm, gain superior to 15 dB, noise figure inferior to 7 dB and saturation output power superior to 20 dBm. To do so the project was divided into sub-projects involving different partners. Among them, III-V Lab was sole responsible of SOAs design and fabrication but was also involved in packaging through partnership with Egide, a packaging specialist and Kyliya, an optical assembler. Development of our wideband SOAs was a key point of the project and good results presented in Chapter 3 were an important milestone. Nevertheless, by developing a dedicated module we hope to push the SOAs performances, thanks to better heat regulation and optical coupling.

A dedicated chip carrier was first developed, featuring two parallel SOAs. Including two chips on the same carrier is rather unusual at III-V Lab and brazing equipment had to be adapted to ensure identical process on both chips. Brazing process itself was changed to improve heat dissipation of the chips. It was indeed discovered that in the first times of the project, air bubbles contaminated brazing metals during the process. After adapting the process a clear improvement of the chips power and NF was noted.

Second part of packaging consisted in including the chips on carrier (CoC) in a module comprising a polarization diversity scheme showed in Figure 5.1. This assembly was realized by Kyliya while the module body was fabricated by Egide. Life of a module therefore starts in the south of France at Egide. It is then sent to III-V Lab where the SOA CoC is fixed in the module and electrical bondings are realized. It can then be transferred to Kyliya in Paris where free-space optics elements are assembled. It is finally sent to Nokia Bell Labs in Villarceaux for measurements and transmission experiments. Measurements presented in this section were done at Villarceaux with Alexis Carbo-Meseguer and Jérémie Renaudier.

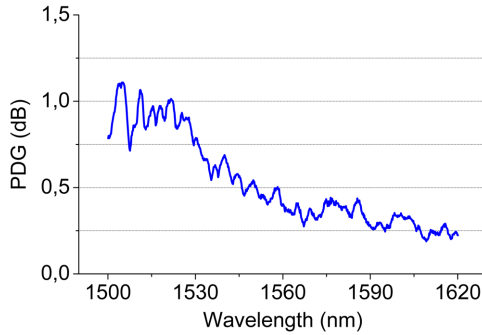


Figure 5.2 – PDG is the gain difference between TE and TM polarizations in the module.

5.1.2 Module description

To achieve polarization insensitivity of the module, two SOA were used in a polarization diversity scheme using free-space optics. It is composed of a polarization splitter followed by two SOAs. TE polarized light goes directly into the first SOA but TM polarized light is rotated to TE polarization before entering the second SOA in order to be correctly amplified. After amplification, the unchanged TE polarized light is rotated to TM polarization to ensure identical optical path. Low coupling losses of about 1 dB are achieved with the set-up. The pair of SOAs is brazed with InSn on a dedicated carrier for good thermal conductivity and minimized electrical resistance. Temperature monitoring is operated with a thermal resistance placed midway between both SOAs and controlled by a Peltier module.

Figure 5.2 presents the polarization dependent gain (PDG) in the module for wavelengths between 1500 and 1620 nm. It characterizes the difference of amplification between TE and TM modes and therefore quantifies the quality of the polarization diversity scheme. The PDG mostly stays below 1 dB showing a good correction of the SOA polarization dependence. This is obtained by slightly adjusting the currents of both SOA one to another. The operating point used in the following section is found at $I_1 = 1$ A, $I_2 = 1.05$ A.

5.1.3 Performances of the module

Figure 5.3 a) shows the measured optical gain dependence to the wavelength for the module at an optical power $P_{in} = 3.5$ dBm injected in one of the SOAs. We obtain a flat gain of 18.5 dB with less than -3 dB variation over 120 nm. The

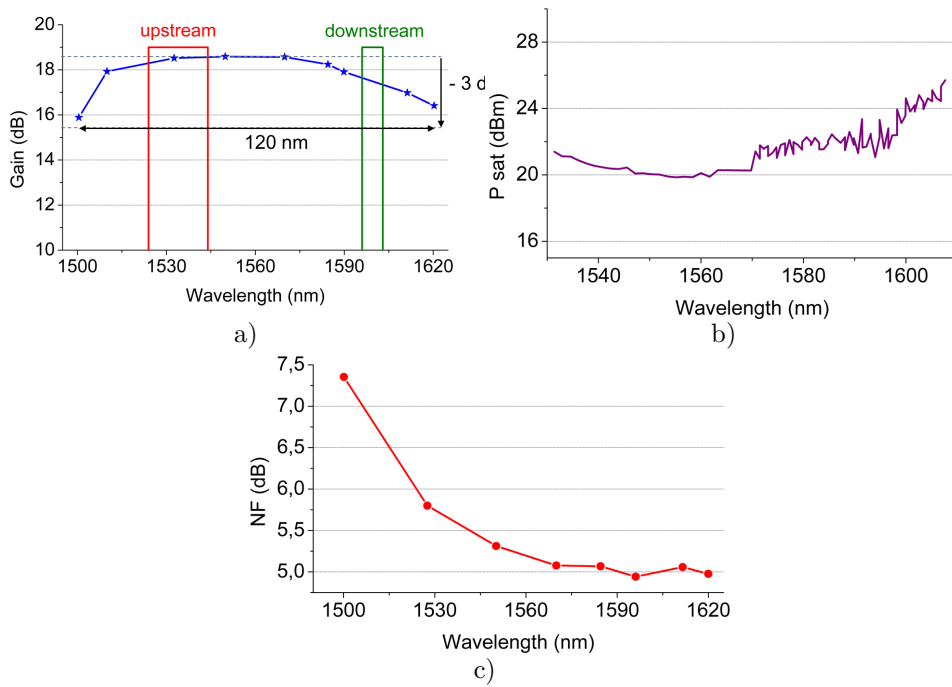


Figure 5.3 – a) Module flat gain over 120 nm. b) Saturation output power of the module. c) Noise Figure of the module.

gain bandwidth extends from 1500 nm to 1620 nm. In order to determine the saturation output power we measure the gain for different optical input powers. The saturation output power was examined for C and L-band wavelengths in Figure 5.3 b). Minimum value for P_{sat} is 20 dBm and goes up to 25 dBm at 1620 nm. P_{sat} decreases at smaller wavelengths due to higher differential gain. NF is also plotted as a function of the wavelength in Figure 5.3 c) from gain and amplified spontaneous emission (ASE) measurements. We reach the low value of 5 dB above 1570 nm. This is to our knowledge the lowest value obtained for a packaged SOA. The NF increases TO 7.3 dB at the shortest wavelengths due to a smaller inversion factor n_{sp} as explained in Section 1.1.

These excellent results can be compared with previous results obtained on SOA B on submount in Chapter 3. We observe a net improvement of all SOA performances. This is due to better heat dissipation in the module and very low coupling losses obtained with the free-space optics. Indeed coupling losses directly intervene in measured NF and gain, which also impacts P_{sat} . Temperature also appears in NF formula through population inversion factor n_{sp} . These measurements demonstrate great impact of these factors. Improvement of P_{sat} might also be due to distribution of power over several channels, although this aspect is not well understood yet. Measuring the module at Nokia Bell Labs laboratory in Villarceaux has also given us the possibility to extend measured bandwidth as their laser sources can reach wavelengths from 1500 nm to 1620 nm. Gain bandwidth limits are however not reached on at these wavelengths, finally proving the ultra-wideband character of our SOA design. Several modules were manufactured and delivered to Nokia Bell Labs. They were used for transmission experiments with excellent results [23].

5.2 Tunable hybrid external cavity lasers

5.2.1 Tunable lasers

Wavelength division multiplexing (WDM) has been key in core and metropolitan optical networks in order to increase the total aggregated data bit rate, and it is now spreading into passive optical networks (PON), mobile backhaul and data centers. However, these segments are particularly sensitive to cost, size footprint and power consumption. Therefore low-cost compact wavelength-tunable lasers are needed for next generation optical transceivers in small factor modules such as CFP/CFP2/CFP4 and QSFP+/QSFP28 both standards used for 100 Gbit/s transmissions [103,104]. Meanwhile, long-distance DWDM systems are running out of channels in the C-band and L-band, and can expand using Raman amplification technology [105]. Coarse-WDM (CWDM) systems will also require upgrading in

order to meet the rise in bandwidth demand by exploring other spectral regions. Consequently, they will have to use C and L band as proposed for PON systems far away from the bands reserved for already existing GPON [106] or for datacenter interconnects [107]. New demand for wideband tunable lasers also arises for other applications like optical coherent tomography (OCT) or light detection and ranging (LIDAR), where a wavelength tunable laser with a short response time and high spectral purity is required.

Many approaches for ultra-wide tuning are based on an external cavity using a gain section, and passive tunable filter with typically Fabry-Perot etalons or ring resonators. These filters can be combined with a Vernier effect, and can be compatible with ultra-wide tuning thanks to the flat envelope of their multiple reflectivity peaks compared to sampled-grating based filters for example. Monolithic solutions have been proposed, such as the monolithic integration on InP. This requires advanced fabrication process to combine different functionalities and waveguide technologies but promising results have been demonstrated [108–110].

Another promising platform for the next generation of photonic integrated circuits is silicon photonics, as it is now available in multiple commercial foundries with high volumes and low manufacturing cost. However, light emission and/or amplification is still not straightforward. Solutions combining III-V and silicon materials are being investigated either through monolithic integration of III-V material directly on top of Silicon on Isolator (SOI) waveguides [111] or hybrid integration with a RSOA edge-coupled in front of the passive SOI waveguides. High performances have been demonstrated in the past decade [112] including high output power of 42 mW [113, 114], low RIN < -135 dB/Hz [115], and low linewidth of 100 kHz [114, 116]. Tunable lasers have been proposed for the C-band with booster semiconductor optical amplifier (SOA) [117] or the L-band [118] but only covering one spectral region at the time. The first C and L bands wavelength tunable laser module was demonstrated with silicon photonic external cavity where several chips were co-packaged with one gain chip for the C band and one gain chip for the L-band [119]. However, reducing the number of chips is expected to provide greater cost savings as less alignments are required.

Hybrid tunable lasers using silica-based (SiO_2) passive lightwave circuits (PLCs) for filtering have also been studied. PLCs are totally passive elements with very low losses, but due to the much smaller index contrast, rings diameters are larger (mm range). These approaches require for example three rings with a double Vernier effect to ensure single-mode operation over a wide wavelength range. This technology has demonstrated more than 90 nm tuning range with output power > 13 dBm [120, 121]. In addition, thanks to their very long cavity, these lasers demonstrated down to 2 kHz linewidth over the C-band [18]. A hybrid laser using Silicon nitride (Si_3N_4) with slightly higher index contrast also recently demonstrated 40 nm tuning range (TR) over the C-band [122]. The passive sections of these lasers

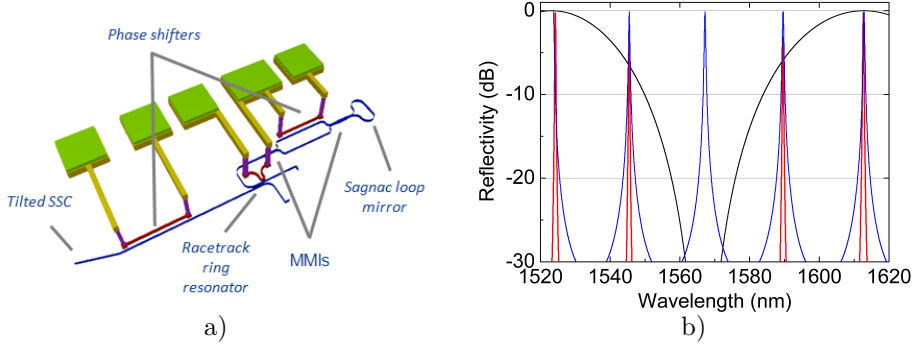


Figure 5.4 – a) Schematic of Hybrid III-V/Si laser via edge coupling including RSOA, spot size converter (SSC), phase shifter, one single racetrack ring resonator filter and asymmetric MachZehnder based mirror. b) Transmission spectra of the RR (blue), the AMZIM (black) and the resulting spectrum (red).

can potentially tune over a very wide range using Vernier effect. But the tuning range of hybrid lasers is mainly limited by III-V material optical gain bandwidth of the RSOA, typically 30-40 nm. In order to tune over C and L bands with one single tunable laser, we propose to use our wideband SOA design with gain bandwidth over 100 nm. We hybridized a RSOA from design A_{bis} with both SOI and silica-based external cavities designed for broad tuning.

5.2.2 External cavity design

5.2.2.1 Silicon-based cavity

Schematic of our silicon-based cavity structure is presented in Figure 5.4 a). The external cavity is composed of one tilted inverted taper, one thermo-optic phase shifter, one racetrack ring resonator (RR) and a variable wavelength tunable mirror including an asymmetric Mach-Zehnder interferometer (AMZI) and one Sagnac loop mirror (SLM). The devices are fabricated on a 220 nm silicon-on-insulator (SOI) platform (8" SOI wafer) with a 3 μm -thick buried oxide (BOX) layer. The propagation losses are measured to be around 2.5 dB/cm. The tilted inverted taper is designed with a length of 150 μm and width of 0.18 μm in order to realize an efficient mode conversion to match the mode of the butt-coupled RSOA with the smaller SOI waveguide mode. When electric current is injected in the micro-heaters their temperature increases due to Joule effect, heating the surrounding waveguide. Temperature dependency of refractive index then allows the peak wavelength of

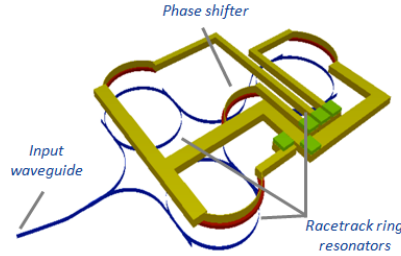


Figure 5.5 – Schematic of silica-based external cavity including three ring resonators, one phase shifter section, corresponding heaters placed on top of each section and tilted in/out waveguide.

the ring resonator filter to be controlled with a micro-heater as well as the filtering function of the mirror. The proposed integrated mirror provides access to a large range of reflectivity over a large optical bandwidth. The principle of the variable reflectivity mirror is based on a reflective asymmetric Mach-Zehnder interferometer (RAMZI) configuration as detailed in [123]. The optical signal propagates through a 1x2 coupler and is split into two optical paths. The length difference between both arms allows a wavelength dependent reflectivity. Figure 5.4 b) shows the principle of lasing mode selection using a ring resonator and such mirror. Addition of the RR peaks spectrum and the AMZIM bandpass spectrum gives transmission spectrum of the cavity. The resulting spectrum has a 90 nm spacing between adjacent maxima and its adjacent peaks have a difference in reflectivity of at least 3 dB. A phase shifter is inserted into one of the branches of this reflective AMZIM. Using such asymmetric reflectivity tunable mirror, we adjust the reflectivity in order to force the lasing wavelength in a different sub-band. We use RR with large free spectral range (FSR) of more than 22 nm. The single-ring laser allows single mode operation as only one Fabry-Perot mode is expected to lase due to the superposition of the material gain, the ring resonator and the AMZI mirror transfer functions.

5.2.2.2 Silica-based cavity

The silica-based cavity is composed of three serial ring resonators, a 1:2 MMI and a phase section represented in Figure 5.5. These elements represent a round-trip cavity length of 24.4 cm corresponding to Fabry-Perot modes with 10 pm free spectral range. Thanks to very low losses in the SiO₂ waveguides, the length of the cavity is not an obstacle to high output power. Output facet is 7°-tilted to minimize reflections at the interface with the RSOA. Cavity tuning range is defined by Vernier effect between the three RRs. The resulting FSR of 62 nm is shown in

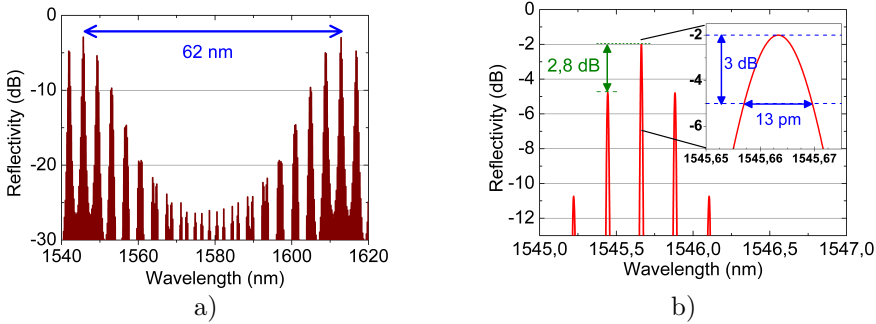


Figure 5.6 – a) Reflectivity spectra of SiO₂ PLC. b) Reflectivity of SiO₂ PLC at the lasing wavelength.

Figure 5.6 a). This design thus limits tuning range of the laser to 62 nm but new designs with 100 nm FSR has been made and will be tested in the future.

Lasing frequency corresponds to the Fabry-Perot mode at the coincidence of rings' transfer functions. To ensure single mode operation there must be a sufficient filtering of the adjacent modes. Good finesse of the filter is obtained for a small coupling factor κ of the rings. However a compromise has to be made as the output power increases with κ . The same κ value is implemented on all rings and fixed at 0.4. Figure 5.6 b) displays close view of the PLC resulting reflectivity. Resulting difference with adjacent coincidence is 2.8 dB, and the 13 pm full width at half maximum of the main peak ensures high rejection between the 10 pm-spaced Fabry-Perot modes inside the same coincidence. Heaters placed on the rings control the position of wavelength Fabry-Perot mode at the center of the main peak. Temperature dependency of refractive index is lower in SiO₂ than in Si leading to great stability, but poor thermal tuning efficiency. Therefore, grooves have been etched along and underneath SiO₂ waveguides to focus heat generation on waveguides, leading to 10 times larger thermal tuning efficiency [124].

5.2.3 Hybrid laser

5.2.3.1 RSOA design

We use a reflective SOA (RSOA) with one 7°-tilted non-reflective facet and a straight 30%-reflective facet. RSOA used in this experiment is taken from Wafer *A_{bis}*. This design was chosen because of its higher gain, in order to compensate for propagation losses in the silicon cavity. Identical RSOAs are used in the silicon

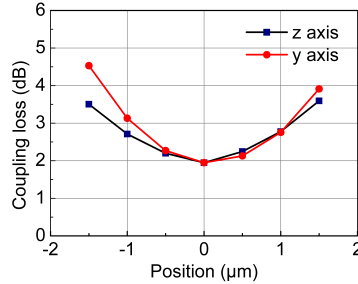


Figure 5.7 – Coupling sensitivity to misalignment.

and silica-based cavities. RSOA length is 3 mm and has a 5 μm -wide waveguide. We presented in Chapter 3 low value of divergence and quasi circularity of optical mode in Wafer A_{bis} waveguide. These characteristics facilitate the coupling of the hybrid laser.

5.2.3.2 Integration and coupling

The RSOA is butt-coupled to the external cavity both for the III-V/Si and III-V/SiO₂ chips. A spot size converter on the silicon PIC allows mode matching between the silicon and RSOA, therefore improving the coupling efficiency. Simulations of coupling losses displayed in Figure 5.7 show coupling tolerance to misalignment between the RSOA and an inverted silicon-based taper. Fiber coupling losses for the RSOA are estimated to be around 3 dB. As for PLC approach, the SiO₂ waveguide is 4.5 μm wide, large enough for good coupling with the RSOA waveguide. Coupling losses were measured to be around 2 dB. During the experiment the RSOA is held in a fixed position. First an optical fiber is coupled to the straight output facet of the RSOA by maximising the collected output power from ASE emission. Then the external cavity is coupled to the tilted facet of the RSOA by observing the appearing of a single-mode spectrum on an OSA. Once both couplings are optimum, the different heaters are controlled to maximize side-mode suppression ratio (SMSR) and output power.

5.2.4 Hybrid laser characterization

Both silicon and silica based cavities presented in this subsection have been developed by two Nokia Bell Labs teams in New Jersey (Murray Hill and Holmdel) while

the RSOA has been designed and fabricated at III-V Lab. As part of our collaboration, lasers characterizations have been partly done in the USA and in France: III-V/Si laser was characterized by an American team, except for the linewidth measurements done at III-V Lab. All the III-V/SiO₂ laser characterizations were done in France.

5.2.4.1 III-V/Si laser

Temperature of the device was stabilized at 20 °C. First, we measured the fiber-to-fiber optical gain of the RSOA device at different wavelengths as shown in Figure 5.8 a). The gain needs to overcome the cavity losses, which are estimated to be around 9 dB round trip. For low injected current, the optical gain reached values higher than the cavity loss for 1.55 and 1.6 μm however higher current is needed to reach such value at 1.5 μm . The fiber-coupled output power is measured depending on the injected current into the RSOA as shown in Figure 5.8 c). Results are reported in Figure 5.8 b). Optical power up to 20 mW (13 dBm) was obtained, which is among the highest fiber-coupled power reported for hybrid laser without booster SOA. The threshold current is 95 mA and the slope efficiency of the fiber-coupled output power is 5% (W/A).

The silicon PIC has been designed for a large wavelength tuning range of 90 nm. We obtained a tuning range from 1540 to 1635 nm making the total tuning range of 95 nm. It is the largest tuning range of hybrid silicon-based tunable lasers ever reported, to the best of our knowledge. The superimposed spectra are shown in Figure 5.9 a). For 95 nm tuning range the heater applied electrical power is around 50 mW. High SMSR above 35 dB is obtained over the full tuning range. Figure 5.9 b) shows the SMSR depending on the wavelength. Then the output power is measured for each wavelength. The facet output power ranges from + 5 dBm up to + 15 dBm, as displayed in Figure 5.9 c). Lower power is obtained in the C-band due to lower RSOA gain in this region at the carrier density corresponding to the laser threshold current. To obtain constant output power at all wavelengths, the RSOA must be optimized so that the laser threshold current corresponds to the flat gain current of the RSOA. Here the RSOA should be made shorter to obtain less gain and delay laser threshold current so that shorter wavelengths also exhibit gain at threshold.

Phase noise measurement were performed using a self-heterodyne set-up as presented in [125] with a 10 km fiber delay line (corresponding to a 47.45 μs delay) and an acousto-optic modulator performing a 80 MHz frequency shift. The temporal signal was acquired with an oscilloscope at 500 MS/s with a total size of 128 mega-sample (MS) (corresponding to 256 ms acquisition time) and a 12 bit resolution. It was processed to extract the power spectral density (PSD) of the beating

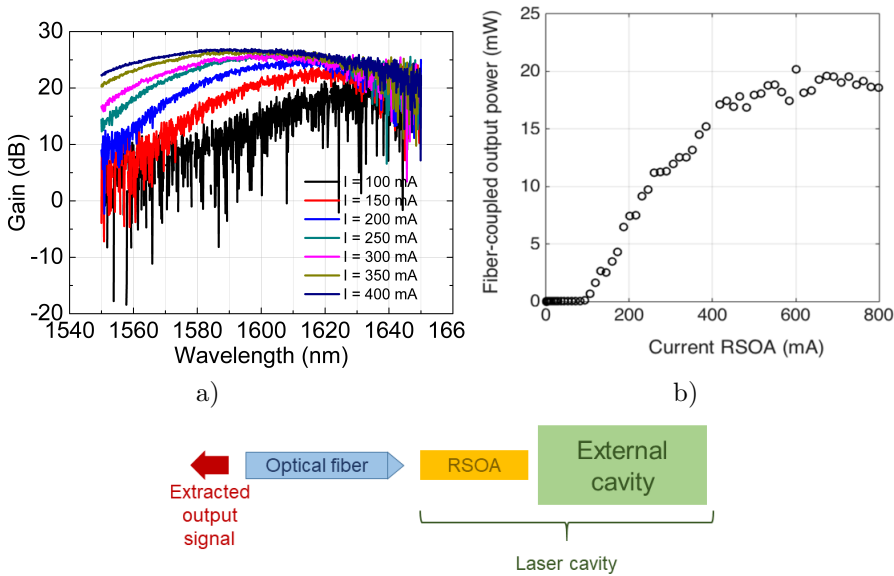


Figure 5.8 – a) Optical gain spectra for several injection currents and b) L-I curve as a function of injected current into the RSOA. c) Scheme of the hybrid external cavity laser.

signal, shown in Figure 5.9 d). A Lorentzian fit gives a linewidth of 550 kHz for the laser, in the same range as previous results [123]. Linewidth measurements were performed at different wavelengths with equivalent results.

5.2.4.2 III-V/SiO₂ laser

Using an identical RSOA, the III-V/SiO₂ hybrid laser was characterized at 20 °C. Maximum fiber-coupled stable output power of 10 dBm is obtained at 250 mA as presented in Figure 5.10 c). Figure 5.10 a) shows a 66 nm tuning range obtained by heating two of the three rings. This result is in good agreement with the simulated FSR of the filter. In this case the third ring is not used and imposes the wavelengths of the triple ring coincidence, generating a discrete spectrum. A continuous spectrum is obtained by simultaneously tuning all three rings. As one heater needs 60 mW to go across the whole tuning range, 180 mW are necessary for continuous tunability of the laser over 62 nm with all three rings. The output power shows less than 5 dB variation along the tuning range which is less than the III-V/Si laser, but on a reduced spectrum. Due to high finesse of the filter high SMSR of 50 dB is reached for all peak wavelengths as presented in Figure 5.10 b). High purity of

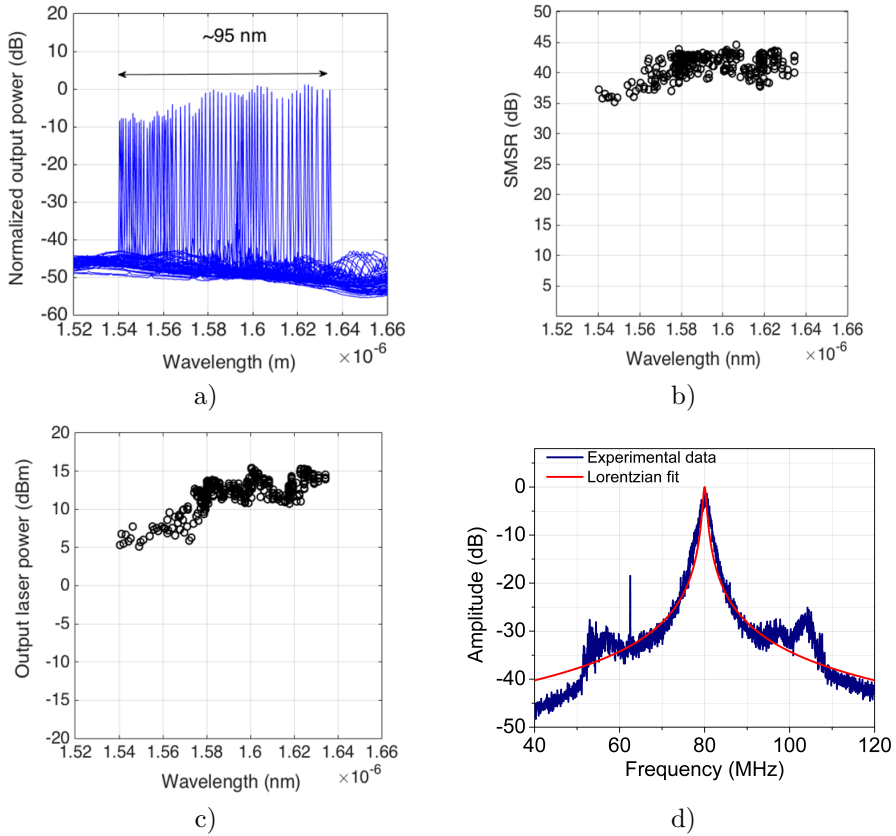


Figure 5.9 – a) Superimposed spectra, b) SMSR and c) laser facet output power as a function of the wavelength, d) linewidth measurement at 1605 nm.

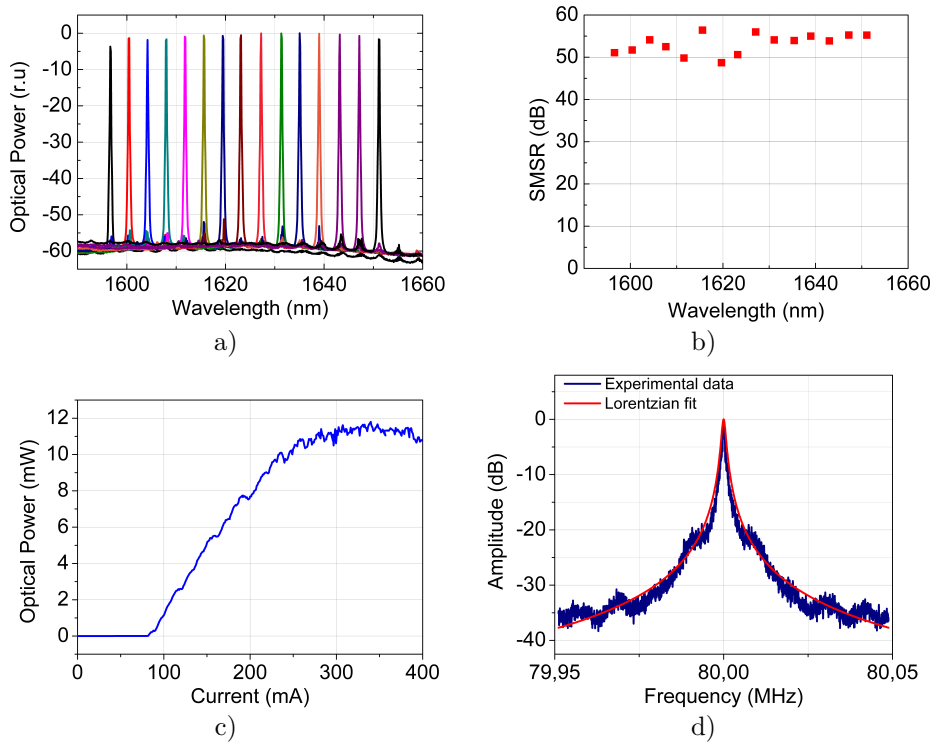


Figure 5.10 – a) Normalized superimposed spectra, b) SMSR, c) L-I curve as a function of injected current into the RSOA and d) linewidth measurement at 1611 nm.

the laser is also expected due to ultra-long cavity. In order to quantify it, linewidth measurements were realized using the self-heterodyne set-up presented before, at 250 MS/s for a total size of 128 MS (512 ms acquisition time). Measurements presented in Figure 5.10 c) correspond to a Lorentzian fit with low linewidth of 1 kHz. These measurements were repeated at different wavelength with comparable results.

5.2.5 Analysis

The set-up used for the experiment is not optimized in terms of thermal management, which degrades the lasers performances. Thus laser power efficiency culminates at 3% at 300 mA for both structures. However lasers linewidths measurements were realized at different wavelengths for both Si and SiO₂ approaches with good reproducibility. High output power is also achieved with both structures without a fixed coupling which is expected to reduce coupling losses and stabilize the structure. Packaged lasers will probably lead to greater values of output power and linewidth.

Intrinsic differences between the structures appear in the results. Silicon has a higher refractive index dependence on temperature than silica. Tuning efficiency is therefore better in silicon. On the other hand thermal stability of silica makes possible the use of one ring as a stable wavelength reference for the optical filter and the use of silica trenched structures makes the tuning power efficiency of one ring comparable in both structures. It is however counterbalanced by the number of rings on the silica chip. Having three rings is indeed mandatory for good mode selectivity as the silica ring resonators have small FSR coming from their size. It is a consequence of the smaller index contrast of silica compared to silicon which allows compactness of silicon chips. Nevertheless silicon compact rings have a larger FSR meaning a lesser quality factor than the larger SiO₂ rings. This results in a better SMSR of the III-V/SiO₂ hybrid laser and participates in reaching an extremely narrow linewidth.

The hybrid lasers present large similarities. Tuning ranges of both lasers are in very good agreement with simulations and fully use the bandwidth allowed by the filters. This proved predictability of behavior is an advantage for the design of future structures. The tuning range is not limited by the RSOA gain bandwidth and could be further extended with appropriate filter design. Although large tuning ranges were already reached with III-V/SiO₂ lasers [120, 121] and could probably be replicated with silicon, the wideband RSOA gives a stable gain condition at all wavelengths resulting in little variation of the lasers characteristics over the C and L bands. However the RSOA gain spectrum has a strong dependence on injection current. In order to achieve the largest tuning range the gain spectrum must be as

flat as possible at the laser threshold. Flat gain is obtained at a particular value of the product $L \times N$ with L the RSOA length and N the electrical carriers density. Optimization of this product will be subject of future studies. Another perspective is the optimization of the RSOA reflective facet. Indeed a low reflectivity means higher collection of the laser output power, but as reflectivity also intervenes in the lasing process it must be varied with caution. Finding the best compromise will further improve the lasers performances.

5.3 Conclusion

We have presented in this chapter two different applications for our wideband SOAs with excellent results both times. These applications show great perspectives for future optical telecommunications in very different areas. After publishing excellent transmission results with our module [19, 23], a field trial with Facebook was organized and gave great results, soon to be published. We can therefore imagine use of our module from access networks to data center interconnects and maybe long-haul transmissions. Given the differences between these networks, specifications in terms of gain, saturation output power, noise figure, power consumption or even cost vary a lot. Specific development would of course be needed to adapt for each application but the potential of our solution has been proved. NF at shorter wavelength is still a challenge which might be addressed through the use of multi-electrode amplifiers.

On the other hand, developing tunable lasers with a very wide tuning range [17, 20] could for instance be used in access networks or to increase bandwidth of DWDM systems for datacenter interconnect, metropolitan or long-haul transmissions. But it could also find applications for imaging or detection. III-V Lab recently started a project on this topic with LPCNO and Apex, a French company manufacturing OSAs. To cover a large bandwidth the OSA indeed needs tunable lasers with a wide tuning range. The project therefore aims at integrating III-V Lab RSOAs into external cavity lasers and also finds interest in developing an equivalent design in the O-band.

Finally as limits of extended bandwidths around the S+C+L-band are being reached, new perspectives appear in the use of O-band. This band might not be suited for long-haul transmissions but could be interesting for access applications as EDFAs can not be used in that band. Excellent NF and P_{sat} performances of our amplifier module would then prove useful and adapting our wideband design to the O-band could be a good solution. Given the perspectives one of future studies challenges will be to adapt our design to the O-band.

Conclusion

Evermore increasing amount of transmitted data forces optical networks to constantly evolve and increase their transmission rates. Several solutions are nowadays combined, however limitations appear on certain development axis. Spectral efficiency of optical fibers notably reaches a maximum seemingly impossible to overcome. Solutions must therefore be found in other directions. In this thesis a new approach was proposed consisting of developing new wideband and high power semiconductor optical amplifiers for wavelength division multiplexing applications. This solution would permit to increase amplification optical bandwidth thus allowing to add more transmission channels. In the past, semiconductor optical amplifiers presented limitations in terms of noise and linearity which prevented their use in optical networks. Nowadays new designs overcome these limitations and semiconductor optical amplifiers are valid candidates for future optical transmissions. We have presented in this thesis the development of such devices from design to practical application.

It was important in the introduction chapter to present the stakes of amplification in optical networks and current solution with erbium doped fiber amplifiers. We also presented the physics of semiconductor optical amplifier and derived most important parameters that are gain, noise figure and saturation output power. After introducing semiconductor optical amplifiers we could compare them to current solution and justify their potential for future networks.

Design of wideband and high power semiconductor optical amplifiers was developed in the second chapter. We designed five different material structures using the same physical principle: using two electronic transitions to extend the amplifier bandwidth. Structures were designed to place optical gain bandwidth between S, C and L bands. An asymmetric cladding consisting of a thick slab placed beneath

the active layers was used on all structures to increase their saturation output power. Optical simulations were done to optimize the design. Resulting structures were 4 mm long, 5 μm wide waveguides manufactured at III-V Lab through an optimized fabrication process.

Characterization of all five structures was done at III-V Lab. We present them in chapter 3. Amplifiers from all designs showed very wide gain bandwidth at the expected wavelengths with good gain value. Great noise figure values below 7 dB in the C+L band were also obtained along with maximum saturation output power of 10 dBm at 500 mA. These performances increase at higher current. Differences between the amplifiers could be explained by design, validating calculations and simulations of the previous chapter. These excellent results also demonstrate tolerance and stability of the design.

Fourth chapter moved away from our specific designs to study waveguide geometry in order to optimize performances of a given material structure. We thus showed better performances of larger waveguides for a structure comprising an asymmetric cladding. We also studied tri-electrode amplifiers which show potential to improve noise figure and saturation output power with an optimized current distribution in the component. Finally we propose a novel integrated gain measurement which could be of great interest in packaged or circuit integrated amplifiers.

Last chapter is dedicated to two applications of the developed amplifiers. Using wideband properties of the SOAs we presented a dedicated polarization independent module. We showed for the system a flat gain of 18.5 dB between 1500 and 1620 nm and a saturation output power above 20 dBm in the same 120 nm bandwidth. Record noise figure value of 5 dB was reached with less than 1 dB variation over the same wavelength range. These performances match the access networks specifications; for instance, the whole expanded spectrum of the PtP links in NG-PON2 will be amplified with a sufficiently large gain and output power, together with a low NF. Same module was successfully used to demonstrate 100 nm continuous-band wavelength division multiplexing transmission system with 115 Tb/s transport over 100 km for datacenter interconnects [23].

We also demonstrate novel hybrid ultra-wide wavelength tunable lasers using silicon or silica-based cavities. The hybrid devices integrate an ultra-wide gain RSOA device and external photonic integrated circuit. The small factor hybrid silicon device is used to successfully demonstrate up to 20 mW fiber-coupled power, ultra-wide tuning range over 95 nm covering the C and L bands and high SMSR above 35 dB over the full tuning range. The hybrid silica device presents 10 mW fiber-coupled output power, 66 nm tuning range with about 50 dB SMSR and 1 kHz spectral linewidth. Both Si and SiO₂ approaches have advantages and downsides but the same RSOA structure was used for both lasers, proving to be extremely promising for wideband wavelength-tunable hybrid external-cavity lasers of diverse

technologies. More adapted filter designs could reach 100 nm tuning range. These results pave the way to low-cost silicon-based integrated lasers for next-generation of C and L band optical transceivers.

Work presented in this thesis is the result of a long-going effort to develop semiconductor optical amplifiers suitable to future optical networks. III-V Lab organization allows control of all steps of a component development, from design and simulations to fabrication, characterization and packaging. This permits a better understanding of the components and their complete optimization. Thanks to this aspect and strong collaborations with partners like LPCNO and Nokia Bell Labs, developed amplifiers show excellent results on all studied aspects and performances above the state-of-the-art. Further perfecting of the devices is still in process but system applications are already considered.

Perspectives for future development include improvement of noise figure and saturation output power of the semiconductor optical amplifier through multi-electrode waveguide. Further test with our module amplifiers for dense wavelength division multiplexing applications are also planned and could prove useful in the next generation of optical networks. Transfer of the wideband semiconductor optical amplifier structure in the O-band is currently studied for the same purpose. Finally design of wideband external cavity filters will allow us to obtain hybrid tunable lasers with more than 100 nm tuning range.

APPENDIX A

List of abbreviations

AMZIM - asymmetric Mach-Zehnder interferometer mirror

ASE - amplified spontaneous emission

CB - conduction band

CoC - chip on carrier

CWDM - coarse wavelength division multiplexing

DBR - distributed Bragg reflector

DML - directly modulated laser

DWDM - dense wavelength-division multiplexing

E - energy of a photon

EDFA - erbium-doped fiber amplifier

FEC - forward error-correcting code

FSR - free spectral range

FUI - fond unique interministériel

FWHM - full width at half maximum

G - fiber-to-fiber gain (dB)

Γ - optical confinement (%)

GaAs - gallium arsenide

InGaAsP - indium gallium arsenide phosphide

InP - indium phosphide

ITU - International Telecommunication Union

IVBA - intervalence band absorption

LSHB - longitudinal spacial hole burning

MBE - molecular beam epitaxy

MMI - multimode interferometer

MOVPE - metalorganic vapor phase epitaxy

MQW - multiple quantum wells

nf or NF - noise figure (linear or dB)

NG-PON2 - next generation passive optical network 2

NRZ - non-return-to-zero

PDG - polarization dependent gain

PIC - photonic integrated circuit

P_{in} - signal input power

PL - photoluminescence

P_{out} - signal output power

P_{sat} - saturation output power

QD - quantum dot

QW - quantum well

RR - ring resonator

RSOA - reflective semiconductor optical amplifier

SAG - selective-area-growth

SCOW - slab-coupled optical waveguide

SLED - superluminescent light-emitting diode

SMSR - side-mode suppression ratio

SNR - signal-to-noise ratio

SOA - semiconductor optical amplifier

SSC - spot size converter

TE - transverse electric

TM - transverse magnetic

TW - travelling wave

VB - valence band

WDM - wavelength-division multiplexing

APPENDIX B

Derivation of saturation output power

We propose in this appendix a derivation of Equation 1.9 given in Section 1.1 and also used in Section 2.2. We follow rate equation model given by Connelly in [126]. We consider a SOA with zero facet reflectivity and we first define material gain as follows:

$$g_m = a_1(n - n_0) \quad (\text{B.1})$$

with n carrier density, n_0 carrier density at transparency and a_1 differential gain assumed to be a constant.

Carrier density n obeys the rate equation with:

$$\frac{dn}{dt} = \frac{J}{ed} - \frac{n}{\tau} - a_1(n - n_0) \frac{I_s}{h\nu} \quad (\text{B.2})$$

First term refers to current injection with J current density in the active region, e charge of an electron and d thickness of the active region. Second term counts for spontaneous emission and also includes Auger effect with τ carrier lifetime and third term for stimulated emission with $h\nu$ energy of a photon and I_s optical signal intensity. Propagation of I_s in the SOA is described by:

$$\frac{dI_s}{dz} = [\Gamma a_1(n - n_0) - \alpha] I_s \quad (\text{B.3})$$

with Γ the optical confinement in the active region and α loss coefficient in the waveguide.

In steady state conditions carrier density is constant and equation B.2 becomes:

$$\frac{J}{ed} + a_1 n_0 \frac{I_s}{h\nu} - \left(\frac{1}{\tau} + \frac{a_1 I_s}{h\nu} \right) n = 0$$

leading to,

$$\begin{aligned} n &= \frac{\left(\frac{J}{ed} + a_1 n_0 \frac{I_s}{h\nu} \right)}{\left(\frac{1}{\tau} + \frac{a_1 I_s}{h\nu} \right)} \\ &= \frac{\tau}{\left(1 + \frac{a_1 I_s \tau}{h\nu} \right)} \times \frac{\left(J + \frac{a_1 n_0 ed I_s}{h\nu} \right)}{ed} \\ &= \frac{\tau}{(h\nu + a_1 I_s \tau)} \times \frac{(Jh\nu + a_1 n_0 ed I_s)}{ed} \\ &= \frac{1}{\left(\frac{h\nu}{a_1 \tau} + I_s \right)} \times \left(\frac{Jh\nu}{a_1 ed} + n_0 I_s \right) \end{aligned}$$

We define the optical intensity $I_1 = \frac{h\nu}{a_1 \tau}$ equivalent to $[W/m^2]$. We have thus:

$$\begin{aligned} n &= \frac{1}{(I_1 + I_s)} \times \left(\frac{J\tau I_1}{ed} + n_0 I_s \right) \\ &= \frac{J\tau}{ed} \times \frac{I_1}{(I_1 + I_s)} + \frac{n_0 I_s}{(I_1 + I_s)} \\ &= \left(\frac{J\tau}{ed} \right) \left(1 + \frac{I_s}{I_1} \right)^{-1} + \frac{n_0 I_s}{(I_1 + I_s)} \end{aligned} \quad (\text{B.4})$$

We define $P_1 = \frac{AI_1}{\Gamma}$ with $A = \text{thickness} \times \text{width}$, section of the active region. P_1 is the optical power in $[W]$ and corresponds to the intensity integrated in the active region section.

By inserting Equation B.4 in Equation B.3 we obtain:

$$\begin{aligned} \frac{dI_s}{dz} &= \left[\Gamma a_1 \left(\left(\frac{J\tau}{ed} \right) \left(1 + \frac{I_s}{I_1} \right)^{-1} + n_0 \frac{I_s}{(I_1 + I_s)} - n_0 \right) - \alpha \right] I_s \\ &= \left[\frac{\Gamma a_1}{\left(1 + \frac{I_s}{I_1} \right)} \left(\left(\frac{J\tau}{ed} \right) + n_0 \frac{I_s}{I_1} - n_0 \left(1 + \frac{I_s}{I_1} \right) \right) - \alpha \right] I_s \\ &= \left[\frac{\Gamma a_1 \left(\frac{J\tau}{ed} - n_0 \right)}{\left(1 + \frac{I_s}{I_1} \right)} - \alpha \right] I_s \end{aligned}$$

and finally,

$$\frac{dI_s}{dz} = \left[\frac{\Gamma g_0}{(1 + \frac{I_s}{I_1})} - \alpha \right] I_s \quad (\text{B.5})$$

with $g_0 = a_1(\frac{J\tau}{ed} - n_0)$ material gain in unsaturated regime.

For simplification of calculation we make the hypothesis that losses are negligible so that $\alpha = 0$. We obtain then,

$$\frac{dI_s}{dz} = \left[\frac{\Gamma g_0}{(1 + \frac{I_s}{I_1})} \right] I_s \quad (\text{B.6})$$

We verify that the function $I_s(z)$ defined as,

$$I_s(z) = I_s(0) \exp\left(\frac{I_s(0)}{I_1}\right) \exp\left(\Gamma g_0 z - \frac{I_s(z)}{I_1}\right)$$

is solution of equation B.6:

$$\begin{aligned} \frac{dI_s}{dz} &= I_s(0) \exp\left(\frac{I_s(0)}{I_1}\right) \left[\Gamma g_0 - \frac{1}{I_1} \frac{dI_s(z)}{dz} \right] \exp\left(\Gamma g_0 z - \frac{I_s(z)}{I_1}\right) \\ \Rightarrow \frac{dI_s}{dz} \left[1 + I_s(0) \exp\left(\frac{I_s(0)}{I_1}\right) \frac{1}{I_1} \exp\left(\Gamma g_0 z - \frac{I_s(z)}{I_1}\right) \right] &= \Gamma g_0 I_s(z) \\ &\Rightarrow \frac{dI_s}{dz} \left(1 + \frac{I_s(z)}{I_1} \right) = \Gamma g_0 I_s(z) \\ &\Rightarrow \frac{dI_s}{dz} = \frac{\Gamma g_0}{\left(1 + \frac{I_s(z)}{I_1} \right)} I_s(z) \end{aligned}$$

Quod erat demonstrandum, equation B.6 is verified.

At the SOA output $z = L$. We name $I_s(L) = I_{sOUT}$ and $I_s(0) = I_{sIN}$. We obtain:

$$\begin{aligned} I_{sOUT} &= I_{sIN} \exp\left(\frac{I_{sIN}}{I_1}\right) \exp\left(\Gamma g_0 L - \frac{I_{sOUT}}{I_1}\right) \\ \Rightarrow I_{sOUT} &= I_{sIN} \exp(\Gamma g_0 L) \exp\left(\frac{I_{sIN} - I_{sOUT}}{I_1}\right) \end{aligned} \quad (\text{B.7})$$

We define SOA gain $G = \frac{I_{sOUT}}{I_{sIN}}$ and $G_0 = \exp(\Gamma g_0 L)$ unsaturated gain. Following

Equation B.7 we have:

$$\begin{aligned}
 G &= G_0 \exp\left(\frac{I_{sIN} - I_{sOUT}}{I_1}\right) \\
 &= G_0 \exp\left(\frac{I_{sIN}(1 - G)}{I_1}\right) \\
 &= G_0 \exp\left(\frac{(1 - G)I_{sOUT}}{GI_1}\right)
 \end{aligned} \tag{B.8}$$

Finally we define $I_{sOUT|3dB}$ saturation intensity for which $G = G_0/2$. At $I_{sOUT|3dB}$ we have:

$$\begin{aligned}
 \frac{G_0}{2} &= G_0 \exp\left(\frac{(1 - \frac{G_0}{2})I_{sOUT|3dB}}{\frac{G_0}{2}I_1}\right) \\
 \Rightarrow \ln(2) &= \frac{(\frac{G_0}{2} - 1)I_{sOUT|3dB}}{\frac{G_0}{2}I_1} \\
 \Rightarrow I_{sOUT|3dB} &= \frac{\ln(2)G_0I_1}{G_0 - 2}
 \end{aligned} \tag{B.9}$$

We can thus deduce saturation output power P_{sat} :

$$\begin{aligned}
 P_{sat} &= \frac{AI_{sOUT|3dB}}{\Gamma} \\
 &= \ln(2) \frac{A}{\Gamma} \frac{h\nu}{a_1\tau} \frac{G_0}{G_0 - 2}
 \end{aligned}$$

What lies behind P_{sat} expression is the idea that a high saturation output power is obtained when carriers out-number photons. It allows all photons to participate in stimulated absorption and maintain nominal gain value.

Bibliography

- [1] L. A. Coldren, S. W. Corzine, and M. L. Mashanovitch, *Diode lasers and photonic integrated circuits*, vol. 218. John Wiley & Sons, 2012.
- [2] Thorlabs, “C-Band Optical Amplifiers (BOAs and SOAs), 1550 nm.” https://www.thorlabs.com/newgrouppage9.cfm?objectgroup_id=3901.
- [3] “Aeon C-band SOAs.” http://03799fb.netsolhost.com/img/pdf/C-Amp_8.5x11_p.pdf.
- [4] K. Morito *et al.*, “A broad-band MQW semiconductor optical amplifier with high saturation output power and low noise figure,” *IEEE photonics technology letters*, vol. 17, no. 5, pp. 974–976, 2005.
- [5] K. Morito and S. Tanaka, “Record high saturation power (+ 22 dBm) and low noise figure (5.7 dB) polarization-insensitive SOA module,” in *Optical Amplifiers and Their Applications*, p. TuC2, Optical Society of America, 2005.
- [6] P. Thiis *et al.*, “Progress in long-wavelength strained-layer InGaAs(P) quantum-well semiconductor lasers and amplifiers,” *IEEE journal of quantum electronics*, vol. 30, no. 2, pp. 477–499, 1994.
- [7] P. Juodawlkis *et al.*, “High-power 1.5 μm InGaAsP slab-coupled optical waveguide amplifiers and lasers,” in *Lasers and Electro-Optics Society (LEOS)*, vol. 1, pp. 425–426, IEEE, 2003.
- [8] P. W. Juodawlkis *et al.*, “Packaged 1.5- μm Quantum-Well SOA With 0.8-W Output Power and 5.5-dB Noise Figure,” *IEEE Photonics Technology Letters*, vol. 21, no. 17, pp. 1208–1210, 2009.

- [9] P. W. Juodawlkis *et al.*, “High-power, low-noise 1.5- μm slab-coupled optical waveguide (SCOW) emitters: physics, devices, and applications,” *IEEE Journal of Selected Topics in Quantum Electronics*, vol. 17, no. 6, pp. 1698–1714, 2011.
- [10] D. Luerssen *et al.*, “Thermal profiling of gain saturation in semiconductor optical amplifiers,” in *Conference on Lasers and Electro-Optics (CLEO)*, vol. 1, pp. 2–pp, IEEE, 2004.
- [11] J. A. Summers *et al.*, “Thermal and optical characterization of photonic integrated circuits by thermoreflectance microscopy,” *IEEE Journal of Quantum Electronics*, vol. 46, no. 1, pp. 3–10, 2010.
- [12] N. Dutta *et al.*, “Monitoring the performance of a semiconductor optical amplifier,” *Applied Physics Letters*, vol. 57, no. 7, pp. 659–660, 1990.
- [13] B. A. Small, B. G. Lee, and K. Bergman, “Empirical method for determining SOA gain based on ASE characterization,” *IEEE photonics technology letters*, vol. 18, no. 21, pp. 2224–2226, 2006.
- [14] M. Newkirk *et al.*, “Three-section semiconductor optical amplifier for monitoring of optical gain,” *IEEE photonics technology letters*, vol. 4, no. 11, pp. 1258–1260, 1992.
- [15] L. Tiemeijer *et al.*, “High-gain 1310 nm semiconductor optical amplifier modules with a built-in amplified signal monitor for optical gain control,” *IEEE Photonics Technology Letters*, vol. 9, no. 3, pp. 309–311, 1997.
- [16] K.-Y. Liou *et al.*, “Operation of integrated InGaAsP-InP optical amplifier-monitoring detector with feedback control circuit,” *IEEE Photonics technology letters*, vol. 2, no. 12, pp. 878–880, 1990.
- [17] G. de Valicourt *et al.*, “Integrated ultra-wide band wavelength-tunable hybrid external cavity silicon-based laser,” in *Optical Fiber Communication Conference*, pp. Th5C–6, Optical Society of America, 2017.
- [18] H. Debregeas *et al.*, “2 kHz linewidth C-band tunable laser by hybrid integration of reflective SOA and SiO₂ PLC external cavity,” *IEEE International Semiconductor Laser Conference*, pp. 50–51, 2014.
- [19] A. Verdier *et al.*, “Wideband material for low linewidth widely tunable laser and reach extender for optical access networks,” in *European Conference on Optical Communication (ECOC)*, IEEE, 2017.
- [20] A. Verdier *et al.*, “Ultrawideband wavelength-tunable hybrid external-cavity lasers,” *Journal of Lightwave Technology*, vol. 36, no. 1, pp. 37–43, 2018.

- [21] R. Bonk *et al.*, “A bi-directional semiconductor optical amplifier acting simultaneously as upstream pre-amplifier and downstream booster in low cost NG-PON2 optical line terminations,” in *Optical Fiber Communications Conference (OFC)*, pp. 1–3, IEEE, 2014.
- [22] “TU-T G989.2: 40-Gigabit-capable passive optical networks 2 (NG-PON2): Physical media dependent (PMD) layer specification,” tech. rep.
- [23] J. Renaudier *et al.*, “First 100-nm Continuous-Band WDM Transmission System with 115Tb/s Transport over 100km Using Novel Ultra-Wideband Semiconductor Optical Amplifiers,” in *European Conference on Optical Communication (ECOC)*, IEEE, 2017.
- [24] T. S. Moss and E. H. P. Gorlicii, “Relations between the Refractive Index and Energy Gap of Semiconductors,” *Review Article phys. stat. sol. (b)*, vol. 131, no. 415, 1985.
- [25] J. W. Crowe and R. M. Craig, “Small-Signal Amplification in GaAs Lasers,” *Appl. Phys. Lett.*, vol. 4, no. 57, 1964.
- [26] J. Crowe and W. Ahearn, “9B8 - Semiconductor laser amplifier,” *IEEE Journal of Quantum Electronics*, vol. 2, no. 8, pp. 283–289, 1966.
- [27] M. J. Adams and M. Cross, “Electromagnetic theory of heterostructure injection lasers,” *Solid-State Electronics*, vol. 14, pp. 865–883, 1971.
- [28] H. Kressel, “Gallium Arsenide and (AlGa)As Devices Prepared by Liquid-Phase Epitaxy (Review Article),” *Journal of Electronic Materials*, vol. 3, no. 4, 1974.
- [29] D. Schicketanz and G. Zeidler, “GaAs-double-heterostructure lasers as optical amplifiers,” *IEEE Journal of Quantum Electronics*, vol. 11, pp. 65–69, feb 1975.
- [30] E. O. Goebel, G. Luz, and E. Schlosser, “Optical gain spectra of In-GaAsP/InP double heterostructures,” *IEEE Journal of Quantum Electronics*, vol. 15, no. 8, pp. 697–700, 1979.
- [31] J. C. Simon, “GaInAsP Semiconductor Laser Amplifiers for Single- Mode Fiber Communications,” *Journal of Lightwave Technology*, no. 9, 1987.
- [32] G. Eisenstein and L. W. Stulz, “High quality antireflection coatings on laser facets by sputtered silicon nitride,” *Applied Optics*, vol. 23, no. 1, p. 161, 1984.
- [33] “Theoretical analysis and fabrication of antireflection coatings on laser-diode facets,” *Journal of Lightwave Technology*, vol. 3, no. 2, pp. 288–293, 1985.

- [34] G. Eisenstein, L. Stulz, and L. Van Uitert, "Antireflection coatings on semiconductor laser facets using sputtered lead silicate glass," *Journal of Lightwave Technology*, vol. 4, no. 9, pp. 1373–1375, 1986.
- [35] M. Sugawara *et al.*, "Theory of optical signal amplification and processing by quantum-dot semiconductor optical amplifiers," *Physical Review B*, vol. 69, no. 23, pp. 235–332, 2004.
- [36] X. Marie and N. Balkan, *Semiconductor modeling techniques*, vol. 159. Springer Science & Business Media, 2012.
- [37] G. P. Agrawal and N. K. Dutta, *Semiconductor Lasers*. Springer, 1993.
- [38] T. Briant *et al.*, "Accurate determination of the noise figure of polarization-dependent optical amplifiers: theory and experiment," *Journal of lightwave technology*, vol. 24, no. 3, p. 1499, 2006.
- [39] D. M. Baney, P. Gallion, and R. S. Tucker, "Theory and measurement techniques for the noise figure of optical amplifiers," *Optical fiber technology*, vol. 6, no. 2, pp. 122–154, 2000.
- [40] T. Mukai, Y. Yamamoto, and T. Kmura, "S/N and Error Rate Performance in AlGaAs Semiconductor Laser Preamplifier and Linear Repeater Systems," *IEEE Journal of Quantum Electronics*, 1982.
- [41] Y. Yamamoto and K. Inoue, "Noise in amplifiers," *Journal of Lightwave Technology*, vol. 21, no. 11, pp. 2895–2915, 2003.
- [42] T. Saitoh and T. Mukai, "1.5 μm GaInAsP traveling-wave semiconductor laser amplifier," *IEEE Journal of Quantum Electronics*, vol. 23, no. 6, pp. 1010–1020, 1987.
- [43] D. D'alessandro, G. Giuliani, and S. Donati, "Spectral gain and noise evaluation of SOA and SOA-based switch matrix," *IEE Proceedings-Optoelectronics*, vol. 148, no. 3, pp. 125–130, 2001.
- [44] A. Crottini *et al.*, "Noise figure improvement in semiconductor optical amplifiers by holding beam at transparency scheme," *IEEE Photonics Technology Letters*, vol. 17, no. 5, pp. 977–979, 2005.
- [45] Cisco, "The History and Future of Internet Traffic." <https://blogs.cisco.com/sp/the-history-and-future-of-internet-traffic>.
- [46] M. Anagnosti *et al.*, "High performance monolithically integrated SOA-UTC photoreceiver for 100Gbit/s applications," in *International Conference on Indium Phosphide and Related Materials (IPRM)*, pp. 1–2, IEEE, 2014.

- [47] S. Bottacchi *et al.*, “Advanced photoreceivers for high-speed optical fiber transmission systems,” *IEEE Journal of Selected Topics in Quantum Electronics*, vol. 16, no. 5, pp. 1099–1112, 2010.
- [48] C. Caillaud *et al.*, “Low cost 112 Gb/s InP DFB-EAM for PAM-4 2 km transmission,” in *European Conference on Optical Communication (ECOC)*, pp. 1–3, IEEE, 2015.
- [49] S. Kanazawa *et al.*, “56-Gbaud 4-PAM (112-Gbit/s) operation of flip-chip interconnection lumped-electrode EADFB laser module for equalizer-free transmission,” in *Optical Fiber Communications Conference (OFC), 2016*, pp. 1–3, IEEE, 2016.
- [50] K. Kazi, *Optical networking standards: a comprehensive guide for professionals*. Springer Science & Business Media, 2007.
- [51] E. Desurvire and J. Simpson, “Amplification of spontaneous emission in erbium-doped single-mode fibers,” *Journal of Lightwave Technology*, vol. 7, pp. 835–845, may 1989.
- [52] R. Mears *et al.*, “Low-noise erbium-doped fibre amplifier operating at 1.54 μm ,” *Electronics Letters*, vol. 23, no. 19, p. 1026, 1987.
- [53] H. Venghaus and N. Grote, eds., *Fibre Optic Communication Key Devices*. Springer, 2012.
- [54] D. Fishman *et al.*, “A high capacity noncoherent FSK lightwave field experiment using Er^{3+} -doped fiber optical amplifiers,” *IEEE Photonics Technology Letters*, vol. 2, no. 9, pp. 662–664, 1990.
- [55] Y. Sun *et al.*, “Transmission of 32-WDM 10-Gb/s channels over 640 km using broad-band, gain-flattened erbium-doped silica fiber amplifiers,” *IEEE Photonics Technology Letters*, vol. 9, no. 12, pp. 1652–1654, 1997.
- [56] Y. Sun *et al.*, “Optical fiber amplifiers for WDM optical networks,” *Bell Labs Technical Journal*, 1999.
- [57] G. Wellbrock and T. J. Xia, “How will optical transport deal with future network traffic growth?,” in *European Conference on Optical Communication (ECOC)*, 2014.
- [58] Yan Sun *et al.*, “An 80 nm ultra wide band EDFA with low noise figure and high output power,” in *Integrated Optics and Optical Fibre Communication - European Conference on Optical Communication (IOOC-ECOC)*, IEEE, 1997.
- [59] Y. Sun *et al.*, “A Gain-Flattened Ultra Wideband EDFA for High Capacity WDM Optical Communications Systems,” in *European Conference on Optical Communications (ECOC)*, (Madrid), 1998.

- [60] B. E. Saleh, M. C. Teich, and B. E. Saleh, *Fundamentals of photonics*, vol. 22. Wiley New York, 1991.
- [61] R. Laming, M. Zervas, and D. Payne, "Erbium-doped fiber amplifier with 54 dB gain and 3.1 dB noise figures," *IEEE Photonics Technology Letters*, vol. 4, pp. 1345–1347, dec 1992.
- [62] O. Lumholt *et al.*, "Quantum limited noise figure operation of high gain erbium doped fiber amplifiers," *Journal of Lightwave Technology*, vol. 11, no. 8, pp. 1344–1352, 1993.
- [63] J. Zhang *et al.*, "Laser integrated modulator module for uncooled, 10 Gbit/s 1550 nm long-reach data transmission," *Electronics Letters*, vol. 39, no. 25, p. 1, 2003.
- [64] S. Tanaka *et al.*, "Compact, very-low-electric-power-consumption (0.84 W) 1.3- μm optical amplifier module using AlGaInAs MQW-SOA," in *European Conference on Optical Communication (ECOC)*, pp. 1–3, IEEE, 2010.
- [65] Z. Li and G. Li, "Ultrahigh-speed reconfigurable logic gates based on four-wave mixing in a semiconductor optical amplifier," *IEEE Photonics Technology Letters*, vol. 18, no. 12, pp. 1341–1343, 2006.
- [66] T. Durhuus *et al.*, "All-optical wavelength conversion by semiconductor optical amplifiers," *Journal of Lightwave Technology*, vol. 14, no. 6, pp. 942–954, 1996.
- [67] D. R. Zimmerman and L. H. Spiekman, "Amplifiers for the masses: EDFA, EDWA, and SOA amplifiers for metro and access applications," *Journal of Lightwave Technology*, vol. 22, no. 1, p. 63, 2004.
- [68] "G.989.2 - 40-Gigabit-capable passive optical networks 2 (NG-PON2): Physical media dependent (PMD) layer specification," tech. rep., International Telecommunication Union (ITU-T), 2014.
- [69] R. Bonk *et al.*, "1.3/1.5 μm QD-SOAs for WDM/TDM GPON with extended reach and large upstream/downstream dynamic range," in *Optical Fiber Communication-includes post deadline papers, 2009. OFC 2009. Conference on*, pp. 1–3, IEEE, 2009.
- [70] C.-F. Lin *et al.*, "Sequence influence of nonidentical InGaAsP quantum wells on broadband characteristics of semiconductor optical amplifiers-superluminescent diodes," *Optics letters*, vol. 26, no. 14, pp. 1099–1101, 2001.
- [71] C.-F. Lin, Y.-S. Su, and B.-R. Wu, "External-cavity semiconductor laser tunable from 1.3 to 1.54 μm for optical communication," *IEEE Photonics Technology Letters*, vol. 14, no. 1, pp. 3–5, 2002.

- [72] M. Gibbon *et al.*, "Selective-area low-pressure MOCVD of GaInAsP and related materials on planar InP substrates," *Semiconductor science and technology*, vol. 8, no. 6, p. 998, 1993.
- [73] J. Zhang, X. Wang, and F. Choa, "A broadband gain material for widely tunable lasers," in *Conference on Lasers and Electro-Optics, (CLEO)*, pp. 208–209, IEEE, 2001.
- [74] T. Akiyama *et al.*, "An ultrawide-band semiconductor optical amplifier having an extremely high penalty-free output power of 23 dBm achieved with quantum dots," *IEEE Photonics Technology Letters*, vol. 17, no. 8, pp. 1614–1616, 2005.
- [75] N. Yasuoka *et al.*, "Quantum-Dot Semiconductor Optical Amplifiers With Polarization-Independent Gains in 1.5 μm Wavelength Bands," *IEEE Photonics Technology Letters*, vol. 20, no. 23, pp. 1908–1910, 2008.
- [76] F. Koyama *et al.*, "Multiple-quantum-well GaInAs/GaInAsP tapered broad-area amplifiers with monolithically integrated waveguide lens for high-power applications," *IEEE photonics technology letters*, vol. 5, no. 8, pp. 916–919, 1993.
- [77] L. Tiemeijer *et al.*, "High-gain, high-power 1550-nm polarization independent MQW optical amplifier," *IEEE Photonics Technology Letters*, vol. 8, no. 9, pp. 1142–1144, 1996.
- [78] K. Morito *et al.*, "High-output-power polarization-insensitive semiconductor optical amplifier," *Journal of lightwave technology*, vol. 21, no. 1, pp. 176–181, 2003.
- [79] A. Borghesani *et al.*, "High saturation power (> 16.5 dBm) and low noise figure (< 6 dB) semiconductor optical amplifier for C-band operation," in *Optical Fiber Communication Conference*, p. ThO1, Optical Society of America, 2003.
- [80] P. W. Juodawlkis *et al.*, "High-power 1.5- μm InGaAsP-InP slab-coupled optical waveguide amplifier," *IEEE photonics technology letters*, vol. 17, no. 2, pp. 279–281, 2005.
- [81] S. Tanaka *et al.*, "Polarization-insensitive GaInNAs-GaInAs MQW-SOA with low noise figure and small gain tilt over 90-nm bandwidth (1510–1600 nm)," *IEEE Photonics Technology Letters*, vol. 20, no. 15, pp. 1311–1313, 2008.
- [82] W. Loh *et al.*, "Noise figure of a packaged, high-power slab-coupled optical waveguide amplifier (SCOWA)," in *Annual Meeting of the IEEE Lasers and Electro-Optics Society (LEOS)*, pp. 852–853, IEEE, 2008.

- [83] H. Carrère *et al.*, “Large optical bandwidth and polarization insensitive semiconductor optical amplifiers using strained InGaAsP quantum wells,” *Applied Physics Letters*, vol. 97, no. 12, 2010.
- [84] L. Schares *et al.*, “Etched-facet semiconductor optical amplifiers for gain-integrated photonic switch fabrics,” in *European Conference on Optical Communication (ECOC)*, pp. 1–3, IEEE, 2015.
- [85] E. Yablonovitch and E. Kane, “Band structure engineering of semiconductor lasers for optical communications,” *Journal of lightwave technology*, vol. 6, no. 8, pp. 1292–1299, 1988.
- [86] A. Adams, “Band-structure engineering for low-threshold high-efficiency semiconductor lasers,” *Electronics Letters*, vol. 22, no. 5, pp. 249–250, 1986.
- [87] E. Yablonovitch and E. Kane, “Reduction of lasing threshold current density by the lowering of valence band effective mass,” *Journal of Lightwave Technology*, vol. 4, no. 5, pp. 504–506, 1986.
- [88] G. Fuchs *et al.*, “Intervalence band absorption in strained and unstrained InGaAs multiple quantum well structures,” *Applied physics letters*, vol. 60, no. 2, pp. 231–233, 1992.
- [89] P. Thijs and T. Van Dongen, “High quantum efficiency, high power, modulation doped GaInAs strained-layer quantum well laser diodes emitting at 1.5 μm ,” *Electronics Letters*, vol. 25, no. 25, pp. 1735–1737, 1989.
- [90] H. Haug and S. W. Koch, *Quantum Theory of the Optical and Electronic Properties of Semiconductors: Fifth Edition*. World Scientific Publishing Company, 2009.
- [91] O. Gilard, *Contribution à la modélisation de diodes laser à puits quantiques contraints pour télécommunications optiques*. PhD thesis, Toulouse 3, 1999.
- [92] G. Bastard, “Wave mechanics applied to semiconductor heterostructures,” 1990.
- [93] B. Miller *et al.*, “Tensile-strained InGaAs/InGaAsP quantum-well optical amplifiers with a wide spectral gain region at 1.55 μm ,” *IEEE photonics technology letters*, vol. 5, no. 5, pp. 520–522, 1993.
- [94] P. Koonath *et al.*, “Polarization-insensitive quantum-well semiconductor optical amplifiers,” *IEEE journal of quantum electronics*, vol. 38, no. 9, pp. 1282–1290, 2002.
- [95] G. Bendelli *et al.*, “A new structure for high-power TW-SLA (Travelling wave semiconductor laser amplifier),” *IEEE Photonics technology letters*, vol. 3, no. 1, pp. 42–44, 1991.

- [96] I. Henning, M. Adams, and J. Collins, "Performance predictions from a new optical amplifier model," *IEEE journal of quantum electronics*, vol. 21, no. 6, pp. 609–613, 1985.
- [97] Y. Nagashima *et al.*, "Asymmetric-cladding 1480-nm pump laser with CW fiber output power of 1 W," in *Optical Amplifiers and Their Applications*, p. MD10, Optical Society of America, 2003.
- [98] E. Marcatili, "Slab-coupled waveguides," *Bell Labs Technical Journal*, vol. 53, no. 4, pp. 645–674, 1974.
- [99] B. Broberg and S. Lindgren, "Refractive index of $\text{In}_{1-x}\text{Ga}_x\text{As}_y\text{P}_{1-y}$ layers and InP in the transparent wavelength region," *Journal of Applied Physics*, vol. 55, no. 9, pp. 3376–3381, 1984.
- [100] T. Motaweh *et al.*, "Wideband gain MQW-SOA modeling and saturation power improvement in a tri-electrode configuration," *Journal of Lightwave Technology*, vol. 35, no. 10, pp. 2003–2009, 2017.
- [101] S. Tanaka *et al.*, "Record high saturation output power (+ 20 dBm) and low NF (6.0 dB) polarisation-insensitive MQW-SOA module," *Electronics Letters*, vol. 42, no. 18, p. 1, 2006.
- [102] W. Loh *et al.*, "Noise figure of watt-class ultralow-confinement semiconductor optical amplifiers," *IEEE Journal of Quantum Electronics*, vol. 47, no. 1, pp. 66–75, 2011.
- [103] Cisco, "Pluggable optical modules: Transceivers for the cisco ons family," tech. rep. Available at <https://www.cisco.com/c/en/us/products/collateral/optical-networking/network-convergence-system-2000-series/datasheet-c78-736938.pdf>.
- [104] Finisar, "Product guide: Transceivers, transponders and active optical cables," tech. rep.
- [105] S. Namiki and Y. Emori, "Ultrabroad-band raman amplifiers pumped and gain-equalized by wavelength-division-multiplexed high-power laser diodes," *IEEE Journal of Selected Topics in Quantum Electronics*, vol. 7, no. 1, pp. 3–16, 2001.
- [106] "From O to L: The Future of optical wavelength-band, author=Gasca, Laurent," 2008.
- [107] C. Lam, "Optical network technologies for datacenter networks," in *Optical Fiber Communication (OFC)*, pp. 1–3, IEEE, 2010.

- [108] T. Segawa *et al.*, “Semiconductor double-ring-resonator-coupled tunable laser for wavelength routing,” vol. 45, no. 7, pp. 892–899, 2009.
- [109] T. Segawa *et al.*, “A Novel Tunable Laser with Flat-Output Wideband Tuning Based on Parallel Ring Resonators,” no. 2, pp. 3–5, 2009.
- [110] S. Matsuo and T. Segawa, “Microring-Resonator-Based Widely Tunable Lasers,” *IEEE Journal of Selected Topics in Quantum Electronics*, vol. 15, no. 3, pp. 545–554, 2009.
- [111] G.-H. Duan *et al.*, “Hybrid III-V on Silicon Lasers for Photonic Integrated Circuits on Silicon,” *IEEE Journal of selected topics in quantum electronics*, vol. 20, no. 4, pp. 158–170, 2014.
- [112] T. Chu, N. Fujioka, and M. Ishizaka, “Compact, lower-power-consumption wavelength tunable laser fabricated with silicon photonic-wire waveguide micro-ring resonators,” *Optics Express*, vol. 17, no. 16, p. 14063, 2009.
- [113] L. Wang *et al.*, “Tunable silicon micro-ring laser for coherent optical communication,” in *Optical Fiber Communication Conference (OFC)*, pp. W2A–26, Optical Society of America, 2016.
- [114] T. Kita, K. Nemoto, and H. Yamada, “Silicon Photonic Wavelength-Tunable Laser Diode With Asymmetric Mach-Zehnder Interferometer,” *IEEE Journal of Selected Topics in Quantum Electronics*, vol. 20, no. 4, pp. 344–349, 2014.
- [115] S. Tanaka *et al.*, “Highly-efficient, low-noise Si hybrid laser using flip-chip bonded SOA,” *Optical Interconnects Conference (OIC)*, vol. 2, pp. 12–13, 2012.
- [116] K. Nemoto, T. Kita, and H. Yamada, “Narrow spectral linewidth wavelength tunable laser with Si photonic-wire waveguide ring resonators,” *IEEE International Conference on Group IV Photonics (GFP)*, vol. 4, pp. 216–218, 2012.
- [117] K. Sato *et al.*, “High output power and narrow linewidth silicon photonic hybrid ring-filter external cavity wavelength tunable lasers,” in *European Conference on Optical Communication (ECOC)*, pp. 1–3, IEEE, 2014.
- [118] J. Hulme, J. Doylend, and J. Bowers, “Widely tunable vernier ring laser on hybrid silicon,” *Optics express*, vol. 21, no. 17, pp. 19718–19722, 2013.
- [119] T. Chu *et al.*, “Full C and L bands wavelength tunable laser module with silicon micro-ring resonators,” in *OptoElectronics and Communications Conference (OECC)*, pp. 866–867, IEEE, 2010.
- [120] Y. Deki *et al.*, “Wide-wavelength tunable lasers with 100 GHz FSR ring resonators,” *Electronics Letters*, vol. 43, no. 4, pp. 225–226, 2007.

- [121] R. Todt *et al.*, “Widely tunable resonated-ring-reflector lasers covering C- and L-bands,” in *European Conference on Optical Communication (ECOC)*, pp. 1–2, IEEE, 2007.
- [122] Y. Fan *et al.*, “Optically Integrated InP- Si_3N_4 Hybrid Laser,” *IEEE photonics journal*, vol. 8, no. 6, pp. 1–11, 2016.
- [123] G. de Valicourt *et al.*, “Hybrid-Integrated Wavelength and Reflectivity Tunable III-V/Silicon Transmitter,” *Journal of Lightwave Technology*, vol. 35, no. 8, pp. 1376–1382, 2017.
- [124] M. Earnshaw *et al.*, “Ultra-low power thermo-optic silica-on-silicon waveguide membrane switch,” *Electronics Letters*, vol. 43, no. 7, pp. 393–394, 2007.
- [125] D. Dennis, “Fiber optic test and measurement,” *Print Hall, New Jersey*, 1998.
- [126] M. J. Connelly, *Semiconductor Optical Amplifiers*. kluwer aca ed., 2002.